CHARACTERIZATION OF SAE 52100 BEARING STEEL FOR FINITE ELEMENT SIMULATION OF THROUGH-HARDENING PROCESS

A THESIS SUBMITTED TO
THE GRADUATE SCHOOL OF NATURAL AND APPLIED SCIENCES
OF
MIDDLE EAST TECHNICAL UNIVERSITY

BY

OZAN MÜŞTAK

IN PARTIAL FULFILLMENT OF THE REQUIREMENTS
FOR
THE DEGREE OF MASTER OF SCIENCE
IN
METALLURGICAL AND MATERIALS ENGINEERING

SEPTEMBER 2014

Approval of the thesis:

CHARACTERIZATION OF SAE 52100 BEARING STEEL FOR THROUGH HARDENING FINITE ELEMENT SIMULATION

submitted by **OZAN MÜŞTAK** in partial fulfillment of the requirements for the degree of **Master of Science in Metallurgical and Materials Engineering Department, Middle East Technical University** by,

Prof. Dr. Canan ÖZGEN _____
Dean, Graduate School of **Natural and Applied Sciences**

Prof. Dr. C. Hakan GÜR _____
Head of Department, **Metallurgical and Materials Engineering**

Prof. Dr. C. Hakan GÜR _____
Supervisor, **Metallurgical and Materials Engineering Dept., METU**

Asst. Prof. Dr. Caner ŞİMŞİR _____
Co-Supervisor, **Manufacturing Engineering Dept., Atılım University**

Examining Committee Members:

Prof. Dr. Rıza GÜRBÜZ _____
Metallurgical and Materials Eng. Dept., METU

Prof. Dr. C. Hakan GÜR _____
Metallurgical and Materials Eng. Dept., METU

Prof. Dr. Bilgehan ÖGEL _____
Metallurgical and Materials Eng. Dept., METU

Asst. Prof. Dr. Eren KALAY _____
Metallurgical and Materials Eng. Dept., METU

Dr.-Ing Feridun ÖZHAN _____
Technical General Manager, ORS BEARINGS INC.

Date: 09.09.2014

I hereby declare that all information in this document has been obtained and presented in accordance with academic rules and ethical conduct. I also declare that, as required by these rules and conduct, I have fully cited and referenced all material and results that are not original to this work.

Name, Last name : Ozan MÜŞTAK

Signature :

ABSTRACT

CHARACTERIZATION OF SAE 52100 BEARING STEEL FOR FINITE ELEMENT SIMULATION OF THROUGH-HARDENING PROCESS

Müştak, Ozan

M.S., Department of Metallurgical and Materials Engineering

Supervisor : Prof. Dr. C. Hakan Gür

Co-Supervisor : Asst. Prof. Dr. Caner Şimşir

September 2014, 116 pages

Through hardening is probably the most important heat treatment process for bearings as final geometrical and material characteristics of the final component are mainly determined in this step. Finite element simulation of heat treatment processes is stand out as a qualified solution for prediction of final properties of component due to advantages e.g. cost and time savings, over real-time furnace experiments. Heat treatment simulation needs accurately extracted material property database including thermo-physical and thermo-mechanical properties of the all phases as a function of temperature. However, only a fraction of these data are available for 100Cr6 (SAE 52100). The present study aimed to the determination of thermo-mechanical and thermo-metallurgical properties of 100Cr6 bearing steel, which are necessary for through hardening simulation, by using a combination of experimental and computational methods. Briefly, the study includes experimental determination of temperature dependent physical properties (e.g. thermal expansion coefficient), temperature dependent mechanical properties (e.g. flow curves, yield strengths, transformation strains, thermal strains), phase transformation kinetics, (e.g. TTT/CCT diagrams), critical temperatures (Ms, Mf, Bs, Ac1 and Ac3) and

investigating the effect of stress on phase transformation. Thermal conductivity, heat capacity, elastic modulus, Poisson’s ratio, enthalpy and density values were calculated using physically based computational methods.

Keywords: Material Characterization, Dilatometry, Finite Element Simulation, Through Hardening.

ÖZ

SERTLEŞTİRME ISIL İŞLEMİNİN SONLU ELEMANLAR YÖNTEMİ İLE BENZETİMİ İÇİN SAE 52100 RULMAN ÇELİĞİNİN KARAKTERİZASYONU

Müştak, Ozan

Yüksek Lisans, Metalurji ve Malzeme Mühendisliği Bölümü

Tez Yöneticisi : Prof. Dr. C. Hakan Gür

Ortak Tez Yöneticisi : Yrd. Doç. Dr. Caner Şimşir

Eylül 2014, 116 sayfa

Sertleştirme, rulman bileziklerinin nihai geometrilerinin ve malzeme karakteristiklerinin belirlendiği başlıca üretim basamaklardan biri olması açısından belki de en önemli ısıl işlem prosesidir. Isıl işlem için sonlu elemanlar benzetimi, bileşenin ısıl işlem sonrası özelliklerinin tahmin edilmesi istendiğinde fırınlarda yapılacak gerçek zamanlı deneylere göre maliyet ve zaman tasarrufu sağlaması açısından ön plana çıkmaktadır. Isıl işlem benzetimi, tüm fazların sıcaklığa bağlı olarak termo-fiziksel ve termo-mekanik özelliklerini içeren hassas bir şekilde oluşturulmuş malzeme veri setine ihtiyaç duymaktadır. Bununla birlikte, bu verilerin sadece bir kısmı 100Cr6 (SAE 52100) için kullanılabilir durumdadır. Bu çalışmada, sertleştirme ısıl işlemi benzetimi için gerekli olan, 100Cr6 rulman çeliğinin termo-mekanik ve termo-metalurjik özelliklerinin, deneysel ve hesaplamalı yöntemler kullanılarak oluşturulması amaçlanmıştır. Deneysel yöntemler kullanılarak; sıcaklığa bağlı olarak fiziksel özellikler; termal genleşme katsayısı belirlenmiş, sıcaklığa bağlı olarak mekanik özellikler; kuvvet-akma eğrileri, dönüşüm gerinmesi, termal gerinmeler, faz dönüşüm kinetiği; TTT/CCT diyagramları, kritik sıcaklıklar (Ms,

Mf, Bs, Ac1, Ac3) hesaplanmış ve gerilimin faz dönüşümüne etkisi incelenmiştir. Termal iletkenlik, ısı sığası, elastik modülü, Poisson katsayısı, entalpi ve yoğunluk gibi değerler fiziksel tabanlı hesaplamalı yöntemler kullanılarak hesaplanmıştır.

Anahtar Kelimeler: Malzeme Karakterizasyonu, Dilatometri, Sonlu Elemanlar Simülasyonu, Sertleştirme Isıl İşlemi.

To My Family…

ACKNOWLEDGEMENTS

The author would like to express sincere gratitude to his supervisor, Prof. Dr. C. Hakan GÜR for giving opportunity to work with him on this research, and also thank for his encouragement, guidance, and support during the research.

The author would like to express his deepest and special appreciation to his co-supervisor Asst. Prof. Dr. Caner ŞİMŞİR. This work would not be possible without his encouragement, knowledge, guidance, patience, help, and support throughout the research.

The author would like to express gratitude to his managers, Dr.-Ing Feridun ÖZHAN, Turhan SAVAŞ and Dr.-Ing Hamdullah MERDANE at ORS Bearings Inc. for their encouragement, guidance and support. The author also would like to express his gratitude to his colleagues, Halil Onat TUĞRUL, Nazmi SAYDEMİR, Mustafa HORTAÇ, Nedim Özgür ENGİN and Zeren TAŞKAYA on behalf of all ORS Bearings Inc. members, for their encourage, interest, help, support and technical assistance.

The author would like to express his thank to Dr. Kemal DAVUT, Tuba DEMİRTAŞ, Deniz DURAN, Nezih MUMCU, Elif EVCİL and all other members of Metal Forming Center of Excellence for their valuable technical assistance, help and support during this research.

The author owes his deepest gratitude to his parents, Nazmiye MÜŞTAK, Mehmet MÜŞTAK and his brother Hamit Kaan MÜŞTAK for their gentle love, inspiration, support and guidance throughout his life.

The author would like to thank heartily to Gül YÜCEL for her love, friendship and support since they met in 2008.

Special thanks go to Ümit AKÇAOĞLU, Murat KAMBEROĞLU, Onur DEMİREL, Erdem MERMER, Sadık YETKİN, Emre AKBAŞ and Murat ÇETİNKIRAN for their friendship, help and support.

This research was financially supported by a SANTEZ project. The author would like to acknowledge Ministry of Science, Industry and Technology of Republic of Turkey and ORS Bearings Inc. for their financial support.

The author would like to acknowledge ONATUS Company for their permission to use of SYSWELD® software in this thesis.

Finally, the author would like to offer his regards and blessings to all of those who supported him in any respect during this research.

TABLE OF CONTENTS

LIST OF TABLES

TABLES

LIST OF FIGURES

FIGURES

LIST OF SYMBOLS AND ABBREVIATIONS

Abbreviations

FEM	Finite Element Method
FDM	Finite Difference Method
BEM	Boundary Element Method
FEA	Finite Element Analysis
EDM	Electrical Discharge Machining
SEM	Scanning Electron Microscopy
TRIP	Transformation Induced Plasticity
FCC	Face Centered Cubic
BCC	Body Centered Cubic
CCT	Continuous Cooling Transformation
TTT	Time-Temperature-Transformation
DCCT	Continuous Cooling Transformation after Deformation
DTTT	Time-Temperature-Transformation after Deformation
CTE	Coefficient of Thermal Expansion
JMA	Johnson-Mehl-Avrami
XRD	X-Ray Diffractometer
PSD	Position Sensitive Detector
GCL	Guarded-Comparative-Longitudinal
DSC	Differential Scanning Calorimetry
DTA	Differential Thermal Analysis
LVDT	Linear Variable Differential Transformer
RMS	Root Mean Square
CALPHAD	Computer Coupling of Phase Diagrams and Thermochemistry
HTC	Heat Transfer Coefficient

Roman Symbols

P	Volume fraction
P_i	Volume fraction of phase *i*
P_i	Property of phase *i*
P^0	Property of phase in pure element
P_{mix}	Property of the mixture
$P(T)$	Material property at a given temperature
X_i	Mole fraction for phase *i*
$P(t)$	Amount of new phase transformed in time *t* Johnson-Mehl-Avrami equation
$n(T)$	Temperature dependent time exponent for Johnson-Mehl-Avrami equation
$k(T)$	Temperature dependent isothermal rate constant for JMA equation
H	Enthalpy
H^0	Standard enthalpy
G^0	Gibbs Free Energy of pure components
q	Heat flux
q	Exponent dependent on the effective diffusion mechanism
K_{RO}	Material parameter for Ramberg-Osgood equation
K^{tp}	Transformation plasticity parameter
K	Hardening constant
N	ASTM grain size
D	Effective diffusion coefficient
E	Elastic modulus
n_{RO}	Strain hardening exponent for Ramberg-Osgood equation
n	Hardening exponent
n	Exponent for modified Koistinen Marburger equation
$f(z)$	Progress of transformation plasticity function
c_k	Multiplier for equation used for calculation of TRIP strain
M_s	Martensite start temperature

M_f	Martensite finish temperature
B_s	Bainite start temperature
Ac1	Ac1 temperature
Ac3	Ac3 temperature
Cp	Specific heat
T	Temperature
T_i	Initial temperature
T_f	Final temperature
T_{ref}	Reference temperature
V	*V*olume
V_i	Initial volume
V_f	Final volume
l	Length
l_0	Initial length
l_f	Final length
t	Time
$t_{8/5}$	Characteristic time

Greek Symbols

α	Thermal expansion coefficient
$\bar{\alpha}$	True coefficient of thermal expansion
α_v	Volumetric thermal expansion coefficient
α_l	Linear thermal expansion coefficient
Ω	Transformation rate constant in the Koistinen-Marburger equation
ε	Strain
ε^{tot}	Total strain
ε^{tp}	Transformation plasticity strain
ε^{el}	Elastic strain

ε^{pl}	Plastic strain
ε^{th}	Thermal strain
ε^{tr}	Transformation strain
$\varepsilon_{i\to j}^{tr}$	Transformation strain of phase *i* to phase *j* transformation
ρ	Density
ρ_{tot}	Total density
ρ_i	Density of phase *i*
κ	Thermal conductivity
φ_v	Interaction parameter
ω_{ij}^{v}	Binary interaction parameter between phase *i* and phase *j*
β	Empirical coefficient for modified Kirkaldy model
τ	Shear stress
τ_{max}	Maximum shear stress
σ_{true}	True stress
σ_y	Yield strength
σ_y^i	Yield strength of phase *i*

Operators

Δx	Change in x
∇x	Gradient of x
•	Scalar product

CHAPTER 1

INTRODUCTION

Ball bearings are widely used in critical structural components utilized in assemblies of industrial sectors such as automotive and transportation, machine tools, food, chemical, energy, aircraft and aerospace. Main duty of ball bearings is to deliver the motion with high speeds and carry remarkable loads with ease and high efficiency. Generally, a ball bearing consists of four main parts which are inner and outer rings, balls and a cage.

The material used for most of the bearing applications is SAE 52100 (DIN-EN 100Cr6, Material No: 1.3505) alloy steel, which has the basic alloying content such as Cr (1.35–1.60 wt. %), Mn (0.25–0.45 wt. %) and Si (0.15–0.35 wt. %) [1] (Table 1). 100Cr6 is also known as the bearing steel, because it has good dimensional stability, high machinability and high hardenability, which are the required properties for most of the bearing applications [2].

Table 1: Standard chemical composition of SAE 52100.

Wt%	**C**	**Si**	**Mn**	**P**	**S**	**Cr**	**Mo**	**Al**	**Cu**	**O**
Min.	0.93	0.15	0.25	-	-	1.35	-	-	-	-
Max.	1.05	0.35	0.45	0.025	0.015	1.60	0.10	0.050	0.30	0.0015

In general, there are three methods used for manufacturing of bearing rings in the industry. In the first method, steel rods are used as a raw material and the rods are drilled and turned for giving the bearing ring shape. In the second method, as-spheroidized seamless steel tubes are used as a raw material instead of rods, the bearing ring form is given to the tubes by turning operations. In the third method, steel rods are used as a raw material and in order to give a bearing ring shape, hot

forging operation is used as a first operation. After the production of inner and outer rings with hot forging, final shape is given with spheroidization heat treatment, cold-ring rolling, turning, through-hardening heat treatment and grinding processes respectively.

The essential properties of bearing applications such as fatigue strength, wear resistance, hardenability and dimensional stability, directly dependent on phases involved and their distribution in the microstructure of the component. Final microstructure and mechanical properties, except final residual stresses, are given by through-hardening heat treatment to the bearing rings. Through residual stresses and surface residual stresses are determined by tempering and grinding processes respectively for the bearing rings. That is why, through-hardening is probably the one of the most important process, among other manufacturing steps, for improving mechanical properties of the bearing rings.

Final microstructure and the resultant physical properties can vary for through-hardening process with changing parameters of heating rate, austenitization temperature, isothermal dwell time, quenching rate and quench temperature [3]. In a metallurgical point of view, final microstructure that is desired for bearing rings consist of both martensite and some amount of retained austenite phases [4].

Determination of the optimum through-hardening process parameters is the key in order to eliminate or minimize production losses and to get desired final geometrical shape, mechanical properties and microstructure. This determination can be done via experimental trials or numerical simulation methods. There are several software codes and tools available, which are based on FEM, FDM and BEM, for simulation of heat treatment process. Each experimental setup generally takes enormous amount of time and can be very costly because trial & error approach with physical experiments must be used in order to determine the optimum process parameters. Due to high cost of experimental heat treatment trials upon prior forming operations of bearing ring, heat treatment simulation stands out as a fast and feasible solution for prediction of final properties of heat treated products.

Heat treatment simulation can be used for optimization of product performance, understanding of heat treatment process and design of innovative heat treatment processes. One can predict internal stresses, distortion, final properties of component both during and at the end of heat treatment process. With the aid of heat treatment simulations, it becomes easier and possible to understand nature of the heat treatment process and changes in material properties during quenching. Without heat treatment simulation, experimental trials must be done in order to investigate the behavior of component during quenching/heat treatment which needs advanced technology instruments and apparatus. It helps to improve residual stress distribution and microstructure of the final component. Simulations can also be used for designing innovative heat treatment processes such as, gas/fluid-jet quenching, intensive quenching or interrupted quenching.

Finite element simulations gained importance due to further development in hardware and associated simulation software. Simulations were become easier to compute, less time consuming and so, feasible for prediction of final properties of heat treated product with the aid of developments in computer hardware and software packages. Despite all the improvements in computer hardware and software packages at last decades, one of the main difficulties is the availability of reliable material input data for heat treatment simulations. The significance of these input data is increasing greatly with increasing demands for predicting quantitative final properties of components at a higher accuracy.

Accurate determination of material properties is important for success in the heat treatment simulation. Forecasting almost-real microstructure, mechanical properties, final geometrical shape and distortion in microns using heat treatment simulations is not possible without appropriate material data set [5-9].

Input data for heat treatment simulation can be determined experimentally, calculated with thermodynamics based computational methods or can be found in the literature. In the literature, there are several works that can be used as an input data for simulation purposes but data available in the literature either insufficient or unreliable [10]. Finding this rare data for similar material or simulation scenario is

almost impossible from the literature. Experimental methods are obviously another solution, however it is a time consuming and costly option, especially when all the material properties are demanded. It needs advanced technology instruments and adequate knowledge in order to conduct experiments and analyze results of the experiments. As a third option, computational methods need reliable software that is based on thermodynamic laws and models for calculation of material properties more accurately as in addition of expertise in computation and analyzing of the results. Consequently, a combination of experimental and computational methods can be the best choice when time, cost and reliability issues are taken into account.

Experimental material characterization needs advanced equipments such as thermo-mechanical simulation systems (Deformation Dilatometer), X-Ray diffractometer (XRD), differential scanning calorimeter (DSC), optical microscopy, electron microscopy techniques, laser flash analyzer and technical experience about these methods [11]. A study about experimentally determined material data set for heat treatment simulations has been conducted by Acht et al. [12, 13]. Furthermore, Ahrens and friends investigated problems about the theoretical, technical and application of material data extraction for heat treatment simulation at their works [14].

Besides the experimental methods used for acquisition of material properties, there have been recent developments that might be used for calculation of material properties by multi-scale computational material property determination methods which are based on thermodynamic kinetics laws and physical behavior models. Sente®'s commercial software package JMatPro® was released less than a decade ago and the code is able to calculate and construct a data set for typical heat treatment simulations [15]. There are several works which can be found in the literature about calculation of material properties by JMatPro® and verification of the produced data set with corresponding experiments [15-21].

In this work, both experimental and computational methods were used in order to compile an accurate material data set for through-hardening simulation. Experimental and computational data were compared with each other and also

compared with the literature. In the second chapter, theory about heat treatment simulation, physics underlying and models available for the quenching, results that had been expected to outcome and literature works in same field were discussed. In the third chapter, experimental results were given with their experimental setup including temperature programs and analysis procedures of experiments. In the fourth chapter, computational results can be found with the theory that was used by JMatPro® for calculation of material properties. Fifth chapter is related with evaluation and justification of experimentally and computationally determined material data set, which was first converted into an input data for SYSWELD® commercial heat treatment simulation software. Verification of material data set, finite element problem setup and detailed comparison of simulation results with the literature were also given in the fifth chapter. In the last chapter, conclusion about the work and outlook were presented.

CHAPTER 2

THEORY AND LITERATURE SURVEY

2.1. Quenching

Quenching might be defined as rapid cooling of material from elevated temperature to the lower temperatures for getting the desired microstructure and phase distribution in order to improve mechanical properties of the material. Cooling rate is so high that thermodynamically least favorable displacive phase transformation can take place, instead of diffusional phase transformation.

Quenching is mostly applied for the metallic alloys and components such as steel, aluminum, titanium and superalloys. In the industry, quenching is widely used for hardening of steel components in order to obtain high hardness in addition to uniform hardness distribution throughout material with minimum size change and deformation with introducing martensite phase into final microstructure.

In through-hardening process, steel component heated above the austenitization temperature (Ac3) at first for complete (except carbides) phase transformation of austenite takes place, then rapidly cooled to desired temperature by the help of quenching media which might be water, oils, polymer solutions or gases.

During quenching, heat transfer, phase transformations and mechanical interactions take place simultaneously. Thus, quenching is a physically very complex process that is taking into account a large number of phenomena resulting from the coupling of thermal, mechanical and metallurgical effects [21]. This phenomena was basically summarized in Figure 1. The main driving force for quenching is the heat transfer and it depends on quenching technique and the interaction between quenching media and the component surface.

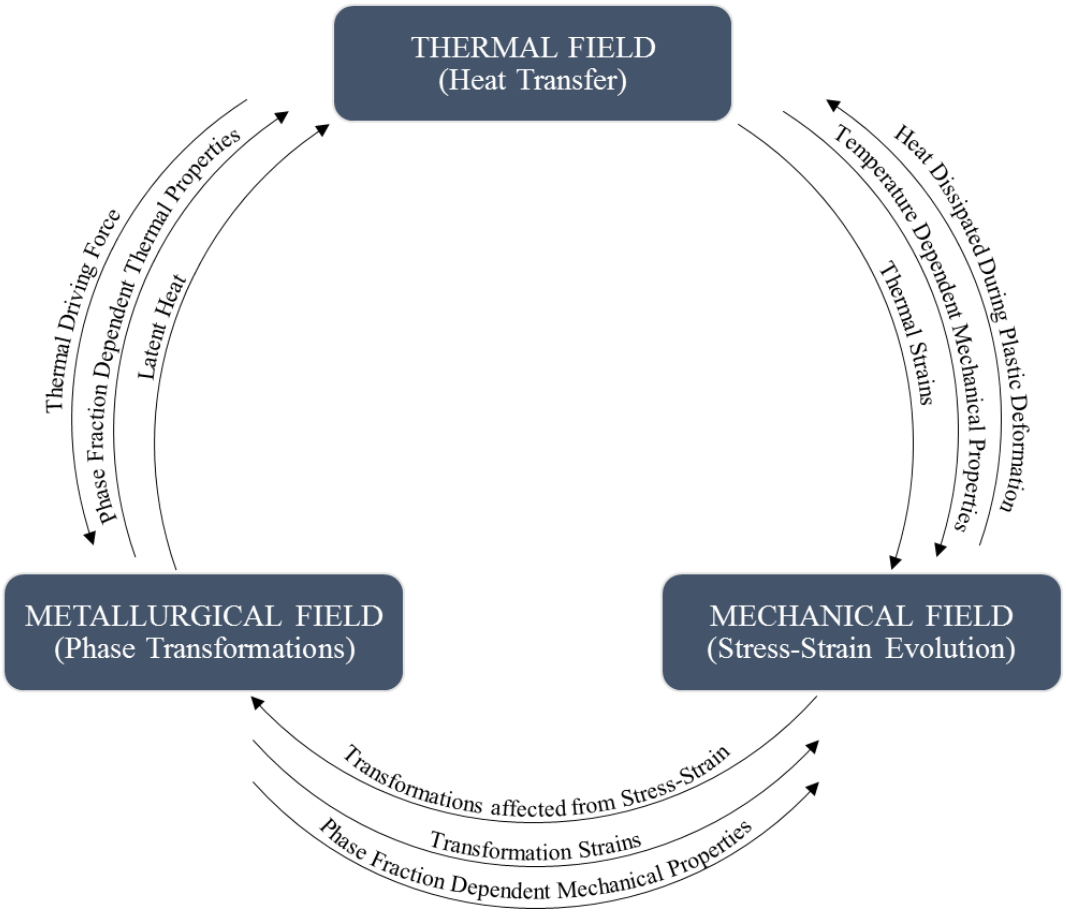

Figure 1: Physical fields and couplings during quenching.

During quenching, temperature gradient is generated due to temperature difference between surface and core of the component which depends on geometry and quenching conditions. Thermal and transformation stresses are generated during quenching process due to this temperature gradient. Volumetric decrease in terms of thermal contraction is observed while austenitized material cools down until phase transformation starts. Different contraction levels might be obtained throughout the component due to the temperature gradient and these contraction levels must be compensated internally with thermal stresses. On the other hand, volumetric increase in the transforming region might be investigated due to difference in crystal structure between the parent and product phases during complete phase transformation of

austenite into pearlite, bainite or martensite. Transformation strain due to phase transformation also must be compensated internally with transformation stresses.

2.2. Heat Treatment Simulation and Simulation of Quenching

The process of heat treatment involves controlled heating and cooling of the metal or alloy in the solid state in order to modify their physical and mechanical properties. Since heat treatment is an energy-consuming process and demanding usually long processing time, every effort made to optimize it and to reduce the costs is welcomed. In this sense, one can find the modern FEM-based analysis tools as great solution. One of the key problems in the numerical simulation of thermo-mechanical processes is material modeling [22]. Material characterization and introducing gathered material data on simulation model for specific application is important for heat treatment simulations.

Quenching simulation is needed in order to understand the nature of the quenching process and changes in material properties during quenching with ease. Furthermore, final mechanical properties and geometry of the component can be optimized using quenching simulations with changing process parameters. However, all the complex mechanisms of the process have to be known and appropriate models and methods have to be used in order to achieve success in quenching simulation. For instance, phase transformations and mechanisms of stress and strain generation due to both transformation and thermal strains during quenching are essential material characteristics for quenching simulation of steel component.

Briefly, history of heat treatment simulations and its applications in the field can be given as follows. At the beginning of 80's and late 70's, FEM-based simulation models for heat treatment and quenching process for steels had been started by Inoue and others in Japan [23-25]. Shortly after this work, Sjöström from Sweden has been contributed with his work on simulation model for quenching process of steel [26]. At the second half of 80's large-scale projects carried out by Mining Faculty of Nancy University at France and Paris Technical University about developing simulation and material models for quenching of steels and these models are still used widely [27-30]. In the 90's, simulation and modeling for thermal surface

hardening processes has started such as carburizing, induction-laser-flame hardening [31-33]. SYSWELD® software had been released in this time period while Gür and Tekkaya have developed a software code for heat treatment [34, 35]. First decade of 2000's is revolutionary in terms of widespread use of simulations of heat treatment. High-budget and large-scale projects carried out in industrialized countries such as Germany, USA, France, Sweden and Japan about the heat treatment simulations [5].

Experimental determination of material properties is one of the keys for achieving success in heat treatment simulations. For each time interval of the process, physical and mechanical properties of each microstructural constituents (martensite, bainite, pearlite, etc.) should be known as a function of temperature. From this point of view, detailed material characterization for extraction of thermo-physical and thermo-mechanical properties is essential [5-9].

2.3. Phase Transformations in Steels

All the material properties are mainly affected by phase transformations and depend on microstructure of the material so, phase transformations are important phenomena for thermal treatments of steels.

Phase transformations might be divided in two main subcategories in terms of their mechanisms which are diffusional phase transformations and diffusionless (displacive) phase transformations.

2.3.1. Diffusional Phase Transformations

Main mechanism used in the diffusional phase transformation is mass exchange between transforming phases where, one phase shrinks while the another one extends. Atomic re-arrangement occurs in crystal structure through lattice by the long-range diffusion mechanism for diffusional phase transformations. Austenite to pearlite transformation might be given as an example for diffusional phase transformations.

2.3.2. Displacive Phase Transformations

Displacive phase transformation refers to spontaneous and small change in position of atoms at a certain temperature instead of long-range diffusion mechanism.

Distance that co-operatively travelled by atoms less than an interatomic distance of crystal structure [4].

Most common phase generated with displacive phase transformation is martensite. Bainite is also given as an example for displacive phase transformation however only a part of change in crystal structure of FCC to BCC can be defined with same manner. Growing of bainite lamellas is driven by diffusion.

2.4. Kinetics of Phase Transformations

Solid-state phase transformations of steel at quenching process directly related with thermodynamic stability and solubility of carbon atoms inside the austenite phase. Solubility of carbon atom and due to alloying elements inside austenite phase decreases during quenching as temperature decreases. These rejected alloying elements and carbon atoms from mother phase of austenite aggregates and forms distinct phases or mixtures on microstructure. This transformation process can be explained with three mechanisms, which are nucleation, growth and impingement of small growing particles.

2.4.1. Kinetics of Diffusional Phase Transformations

There are several models and mathematical approaches available in the literature for diffusional phase transformations. Transformation models of Austin-Rickett, Johnson-Mehl-Avrami and Leblond for diffusional phase transformations can be given as examples. Modelling of nucleation and growth of particles that reach critical radius is the main concern for diffusional case. At nucleation stage, new phase formation begins with formation of nuclei during cooling. At the growth stage, transformation rate increases due to growth of nuclei which have reached the critical radius. Finally, transformation rate decreases due to increase in impingement of growing particles till the transformation stops. Volume needed for nucleation and probability of finding untransformed regions at parent phase decrease at which transformation rate starts to slow down. S-shape curve for an isothermal transformation, which were represented in Figure 2, shows the tendency of transformation rate with respect to time.

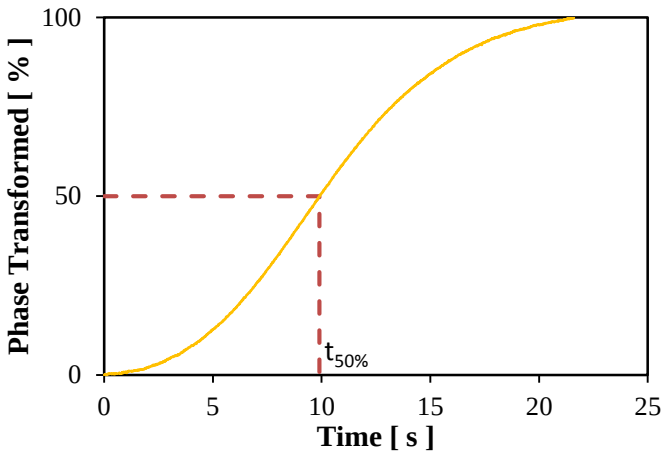

Figure 2: Representative S-shape curve for an isothermal transformation.

The most frequently used isothermal model for diffusional phase transformations was developed by Johnson, Mehl and Avrami [36, 37] and it is given in Equation (1):

$$P(t) = 1 - exp\left[-(k(T) \cdot t)^{n(T)}\right] \quad (1)$$

where, *P(t)* is amount of new phase transformed, *t* is time, *n(T)* is temperature dependent time exponent and *k(T)* represents temperature dependent isothermal rate constant. However, in case of quenching, temperature is not constant and hence anisothermal transformation models are needed. Luckily, isothermal transformation models can be extended to the anisothermal cases by some modification.

One of the most used method for extending isothermal transformation kinetics to anisothermal one consists of additivity hypothesis proposed by Scheil [38] combined with a fictitious time phenomena. This concept has been applied to solid state transformations by Cahn [39] and generalized by Christian [40].

Heating or cooling path can be divided into equal isothermal steps. For each isothermal step *(i+1)*, fraction of newly formed phase can be computed using isothermal kinetics (2):

$$P_{i+1} = P_{i+1}^{max} \cdot \left[1 - exp\left[-\left(k_{i+1} \cdot (t_{i+1} + dt)\right)^{n_{i+1}}\right]\right] \quad (2)$$

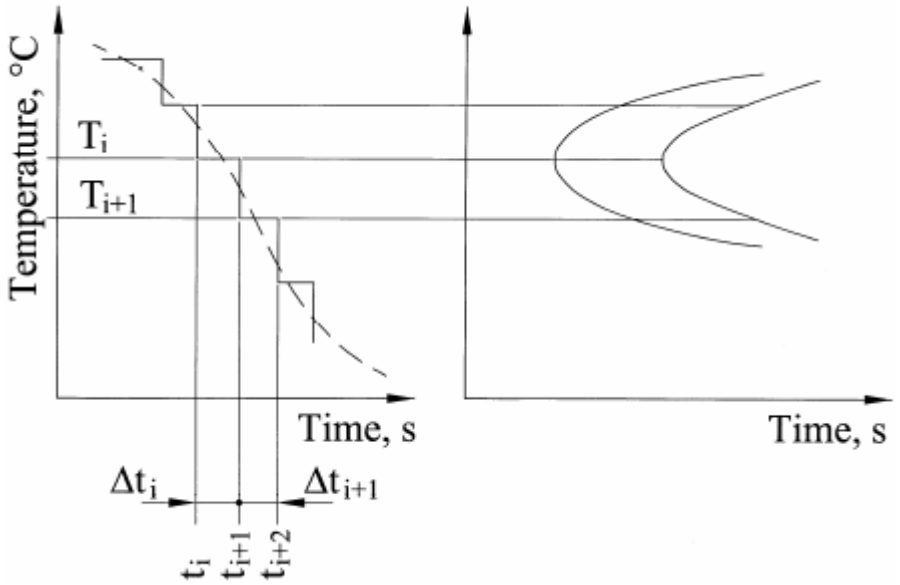

Figure 3: Schematic representation of Scheil's additivity principle.

Another way for extending isothermal transformation kinetics to anisothermal transformation kinetics is the integration of the isothermal kinetic law. This second type of prediction model requires an inherently "additive" kinetic equation which is also generated from JMA equation [41].

2.4.2. Kinetics of Displacive Phase Transformations

The displacive transformation that is extensively studied in metals is the martensitic transformation. Displacive transformation is usually so fast that time dependency can be simply neglected. Kinetics of displacive phase transformations cannot be described with Avrami type equations. Generally, Koistinen-Marburger Equation (3) is often used for calculation of the proportion of athermal martensite formed as a function of temperature [42]:

$$P(T) = 1 - exp\left[-\Omega \cdot \left(M_s - T_f\right)\right] \quad ; \mathrm{T} \leq \mathrm{M_s} \tag{3}$$

where, *P(T)* is proportion of martensite transformed at a given temperature, M_s is the martensite start temperature, Ω is transformation rate constant and often considered to be approximately *0.011* and T_f represents the temperature that is desired to

proportion of martensite calculated. Later Magee [43] and Lusk et al. [44] developed alternative approaches to the martensitic transformations.

M_s temperature can vary sharply with prior diffusional phase transformations because of the change in carbon concentration in austenite phase. Moreover it is also known that, stress and prior plastic deformations are also affect the M_s temperature significantly.

2.5. Effect of Stress on Phase Transformations and Transformation Plasticity

The effect of stresses on phase transformation can be summarized and divided into two major effects, firstly, it changes transformation kinetics and secondly it causes generation of irreversible permanent strain, namely, transformation plasticity even the material exposed to stresses which are smaller than the yield strength of soft phase at a given temperature [45-48].

During thermal treatments, material is subjected to fluctuating thermal and transformation stresses due to temperature gradient and phase transformations respectively. These fluctuating stresses may affect the phase transformation with changing critical transformation temperatures or phase transformation kinetics. They may accelerate or retard the transformation of austenite into the product phases.

The effect of stress on transformation kinetics of martensite has been investigated in many studies [4, 48-52]. Critical temperature for martensitic transformation, M_s, may vary with type of stress applied on the material. Stress state applied on material can be decomposed into two parts as deviatoric stress and hydrostatic pressure. It is known that positive hydrostatic pressure may alter M_s temperature to the lower temperatures while uniaxial stresses increase M_s temperature contrarily. Hydrostatic pressure confronts to the transformation dilation of martensite, so M_s might be expected to decrease to lower temperatures. However, increase in M_s by deviatoric stresses can be explained with interaction of shear components of global stress state with displacive transformation strains [21, 48, 49].

Hydrostatic pressure also retards diffusional transformation by confronting the volumetric expansion generated by phase transformation. On the contrary,

transformation rate accelerated by uniaxial stresses applied on material, which increases nucleation sites with increasing internal defects and increases free volume needed for diffusional transformations [48, 51, 53, 54].

Transformation plasticity is a deformation mechanism known that causes a permanent irreversible deformation during phase transformation. Greenwood and Johnson [55], Magee [43] and later Leblond [29] have developed models for transformation plasticity. In uniaxial loading, transformation plasticity (ε^{tp}) is often described by the Equation (4):

$$\varepsilon^{tp} = K^{tp} \cdot \sigma \cdot f(z) \tag{4}$$

where, K^{tp} is the transformation plasticity parameter, σ is the applied stress and *f(z)* is progress of transformation plasticity function expressing the dependency of transformation plasticity strain on the fraction transformed.

Progress of transformation plasticity function *f(z)* must satisfy *f(0) = 0* and *f(1) = 1*. The transformation plasticity strain is referred as the "*extent of transformation plasticity*", when *z=1*. Different expressions for *f(z)* can be found in the work of Fischer et al. [56].

There are several models published in the literature about calculation of transformation plasticity parameter, K^{tp}, which can be generalized in the form of Equation (5) [29, 55, 57, 58]:

$$K^{tp} = c_k \cdot \frac{\Delta V}{\sigma_y^a \cdot V} \tag{5}$$

where, c_k is the multiplier for equation, $\frac{\Delta V}{V}$ represents the volume change during transformation and σ_y^a is the yield strength of austenite at that specific temperature. Different models can be obtained by changing multiplier c_k between *0.66* and *0.83*, given in Equation (5).

2.6. Thermo-physical Properties

2.6.1. Coefficient of Thermal Expansion, Thermal and Transformation Strains

Thermal expansion coefficient, which is generally denoted as α or *CTE*, can be defined as a material property that is related with a change in volume with respect to change in temperature. There are two exact definition often mentioned which are true coefficient of thermal expansion, denoted by $\bar{\alpha}$, or mean coefficient of thermal expansion, denoted by α [59]. True coefficient of thermal expansion takes slope of line between two precise points on the length change versus temperature plot into account, while mean coefficient of thermal expansion related with the slope of the tangent of data series over a range between strain versus temperature plot. Thermal expansion coefficient can be calculated with the general form in Equation (6):

$$\alpha_{avg} = \frac{1}{(T_f - T_i)} \cdot \int_{T_i}^{T_f} \alpha(x)dx \tag{6}$$

It is also described with the following form for calculation of volumetric coefficient, α_v (7):

$$\alpha_v = \frac{\Delta V}{V_0} \cdot \frac{1}{\Delta T} \tag{7}$$

where, ΔV is volume change $(V_f - V_0)$, V_0 is initial volume and ΔT is the temperature change. Volume coefficient of thermal expansion, α_v might be assumed approximately equal to $3\alpha_l$, when thermal expansion of the material is isotropic. Linear coefficient of thermal expansion, α_l, can be calculated with following Equation (8):

$$\alpha_l = \frac{\Delta l}{l_0} \cdot \frac{1}{\Delta T} \tag{8}$$

where, Δl is length change $(l_f - l_0)$, l_0 is initial length and ΔT represents the temperature change.

Thermal strain generated by thermal expansion/contraction during heating/cooling for phase *i* can be defined by Equation (9),

$$\varepsilon_i^{th} = \varepsilon_i^{tr} + \int_{T_0}^{T} \alpha_i dT \tag{9}$$

taking the integral of Equation (9), thermal strain for phase *i* takes the following form (10):

$$\varepsilon_i^{th} = \varepsilon_i^{tr} + \alpha_i \cdot (T - T_0) \tag{10}$$

where, T_0 is initial temperature (20 °C), ε_i^{th} is thermal strain, ε_i^{tr} is transformation strain at temperature T_0, α_i is coefficient of thermal expansion and *T* is temperature.

Transformation strain, phase *i* to *j* due to phase transformation can be described as following form (11):

$$\varepsilon_{i\to j}^{tr}(T) = \varepsilon_j^{th}(T) - \varepsilon_i^{th}(T) \tag{11}$$

where, $\varepsilon_j^{th}(T)$ is thermal strain of phase *j* at temperature *T* and $\varepsilon_i^{th}(T)$ is thermal strain of phase *i* at temperature *T*.

Transformation strain can also be described as a form of densities of phases *i* and *j* with following Equation (12) [60]:

$$\varepsilon_{i\to j}^{tr}(T) = -1 + \sqrt[3]{\frac{\rho_i(T)}{\rho_j(T)}} \tag{12}$$

where, $\rho_i(T)$ is density of phase *i* at temperature *T* and $\rho_j(T)$ is density of phase *j* at temperature *T*.

2.6.2. Density

Density of a steel component is dependent on the phases included in its microstructure. Crystal structure of phase mainly determines the density of the phase. Density of the steel component can be calculated with the Equation (13) by

summing the densities of each phases included at a given temperature according to their proportions assuming linear mixing rule is applicable:

$$\rho_{tot} = \sum_{n} \rho_n \cdot P_n \tag{13}$$

where, ρ represents density, P is the volume fraction of phases and n is the number of phases included. Density of a steel component changes with changing temperature which can be explained by volumetric expansion/contraction of material and solubility of carbon atom in the microstructure. The temperature dependency of density is important for through-hardening case in which it must be given as a function of temperature.

There are several methods used in order to measure the density of a steel component. Buoyancy method, which uses Archimedean principle, can be used for density measurements at room temperature. However, Buoyancy method is useless at high temperatures. On the other hand, it might be supported with dilatometric experiments in order to calculate density of steel at high temperatures. A combination of room temperature measurement via Buoyancy method and high temperature measurements with a dilatometer might be the solution for determining densities of phases experimentally as a function of temperature. XRD might also be used for determination of densities of each distinct phases [60], however XRD is not feasible when compared with dilatometry for a density measurement [10].

Density of phase i can be calculated with following relation (14), if the values of density at reference temperature and the thermal expansion coefficient of phase i are known:

$$\rho_i(T) = \rho_i(T_{ref}) \cdot \frac{1}{\left[1 + \alpha_i \cdot (T - T_{ref})\right]^3} \tag{14}$$

where, $\rho_i(T_{ref})$ is density at reference temperature, α_i is coefficient of thermal expansion and T_{ref} is the reference temperature.

2.6.3. Thermal Conductivity, Specific Heat Capacity and Enthalpy

Thermal conductivity, κ, can be described as a property of material related with the ability to conduct heat. Heat flux, q, can be expressed with following Equation (15) by Fourier's law which includes thermal conductivity:

$$q = -\kappa \cdot \nabla T \tag{15}$$

where, ∇T is the temperature gradient. In order to determine thermal conductivity value, heat flow meter apparatus or GCL heat flow technique might be used and detailed information about these methods can be found in ASTM C518-10 [61] and E1225-13 [62] respectively.

Specific heat capacity or thermal capacity, often denoted by *Cp*, is a measurable quantity and can be defined as an energy or heat required for changing temperature of material for a given amount. Higher the specific heat capacity means less temperature change when compared with lower *Cp* in terms of same heat given or extracted from the material. Specific heat capacity is known as a temperature and phase dependent material property. From the heat capacity, enthalpy for phase *i* can be calculated as follows (16):

$$H_i(T) = \int_{T_0}^{T} Cp_i(T) \cdot dT + H_i^0 \tag{16}$$

where, *i* is element index and H_i^0 is the standard enthalpy for phase *i*.

Specific heat capacity is often determined with calorimetry techniques such as DSC and DTA. Moreover, the enthalpy might also be obtained with DSC by calculating area under the DSC curve.

2.7. Mechanical Properties

2.7.1. Material Models for Mechanical Interactions

There are several constitutive models that are available, such as elasto-plastic, elasto-visco-plastic, and visco-plastic models. Rate independent elasto-plastic models generally used for quenching purposes. Yield function, hardening rule and flow rule

components of elasto-plastic material models must be defined in order to predict the behavior of material.

Yield function determines the boundary between fully elastic and elasto-plastic behavior. The two relations, Tresca (17) and von Mises (18) criteria are generally used as yield functions which are given respectively as followings:

$$\tau_{max} \geq {}^{\sigma_y}/_{2} \tag{17}$$

$$\sigma_y = \frac{1}{2}[(\sigma_1 - \sigma_2)^2 + (\sigma_2 - \sigma_3)^2 + (\sigma_1 - \sigma_3)^2 + 6(\sigma_{12}^2 + \sigma_{23}^2 + \sigma_{13}^2)] \tag{18}$$

where, τ_{max} is maximum shear stress, σ_y is yield stress and σ_1, σ_2, σ_3 are principal stresses.

Hardening rule related with interaction between effective plastic strain and the yield strength. The power-law hardening Equation (19) [63] might be used in order to describe the strain hardening with plastic deformation:

$$\sigma = K \cdot (\varepsilon_T)^n \tag{19}$$

where, K is hardening constant, ε_T is total strain and n is the hardening exponent.

Isotropic hardening and kinematic hardening concepts are available and generally used for representation of hardening behavior of material. In isotropic hardening, yield surface expands while shape of yield surface remains same. In kinematic hardening, yield surface translates in stress space while preserving its shape.

2.7.2. Strain Constituents

Total strain generated during heat treatment might be given various individual strain constituents as following (20) [64];

$$\varepsilon^{tot} = \varepsilon^{el} + \varepsilon^{pl} + \varepsilon^{th} + \varepsilon^{tr} + \varepsilon^{tp} \tag{20}$$

where, ε^{el} is elastic strain, ε^{pl} is plastic strain, ε^{th} is thermal strain, ε^{tr} is transformation strain and ε^{tp} is the transformation plasticity strain.

2.8. Experimental Determination of Material Properties by Dilatometry

Dilatometry is a thermo-theoretical technique for the measurement of dimension change of a material as functions of both temperature and time when subjected to pre-defined temperature-time-deformation cycles. Obtained data can be converted into strain as functions of both time and temperature which can later be used for determination of material properties such as the beginning and completion of phase transformations during the thermal cycle.

Dilatometer is an instrument that above mentioned thermal simulations can be performed in order to record any dimension change on the sample during for pre-defined time-temperature program with the help of its high-sensitive displacement measuring system, heating and cooling systems. As an output of the dilatometer experiment, relative change in length-and/or-diameter versus temperature plot is known as dilatometric curve (Figure 4).

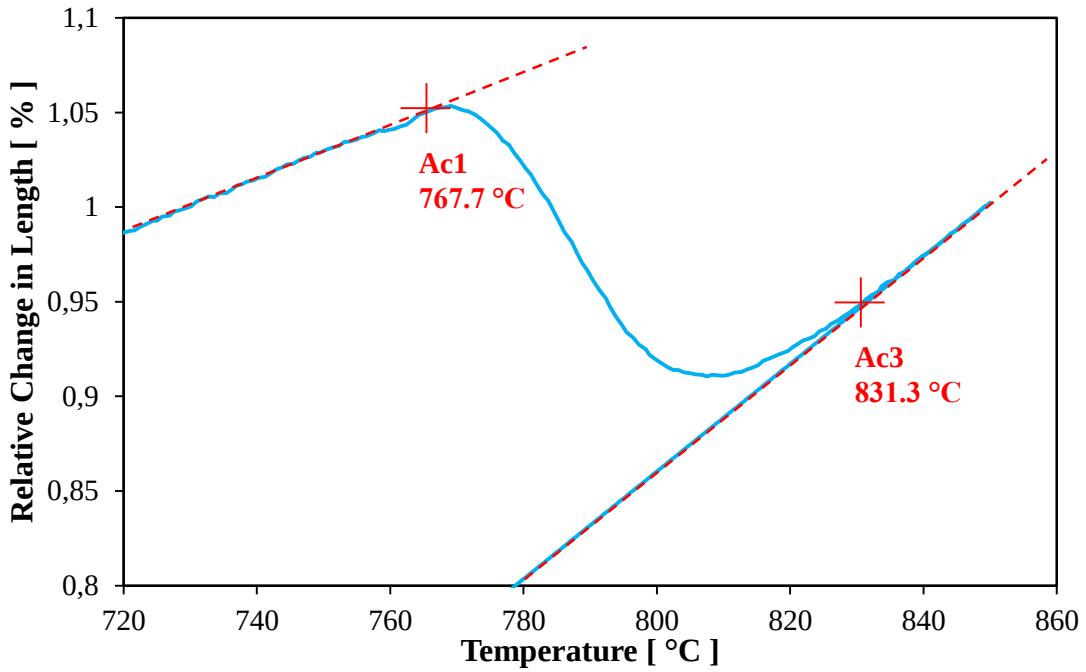

Figure 4: Relative change in length vs. temperature of 100Cr6 with an initial spheroidite microstructure showing complete transformation of initial phase to austenite. Temperature interval of 720-860 °C was plotted.

In this work, four different dilatometry techniques were used at the experimental side, which were alpha & sub-zero dilatometry, quenching dilatometry, deformation dilatometry and stressed dilatometry.

2.8.1. Alpha and Sub-Zero Dilatometry

Alpha dilatometry is often used in order to determine the thermal expansion coefficient of steels. Change in dimension with respect to temperature must be measured in order to determine thermal expansion coefficient at a given heating or cooling thermal path. Low-expansion fused silica measuring components are used in conjunction with a displacement measuring system for high-precision measurement of dimension change. ASTM publications are available about measuring coefficient of thermal expansion, namely, E228 and E831.

Sub-zero dilatometry is used for investigating the thermal expansion coefficient, thermal strain and transformation strains below room temperature. It is known that the martensite finish (M_f) temperature for 100Cr6 is less than -90 °C. Therefore, sample must be cooled down to approximately -130 °C in order to reach M_f temperature and investigate the behavior of martensitic phase during this cooling path.

In Sub-Zero dilatometry, cooling system includes liquid nitrogen with an exchanger that is used for cooling down of helium or nitrogen gases from room temperature (20 °C) to -130 °C. These gases used for gas-nozzle-quenching of specimen in order to reduce its temperature approximately -130 °C. High cooling rates like 2000 °C/s might be achieved via this mode, however thin walled hollow samples must be used in order to achieve these high cooling rates.

2.8.2. Quenching Dilatometry

Quenching dilatometry is used for determination of critical temperatures of phase transformation, construction of time-temperature-transformation (TTT) diagram and continuous-cooling-transformation (CCT) diagram. Hollow samples might be cooled via linear, exponential or $t_{8/5}$ cooling rates. Phase transformation occurring at this continuous heating and cooling paths or in the isothermal dwell stage can be

accurately observed via displacement measuring system as a relative length changes of the sample material. Critical points on dilatometric curve can be constructed one by one according to expected phase transformation behavior (expansion or contraction) for sample material. After conducting a series of experiments at different cooling rates or isothermal dwell times, determined critical points of phase transformations can be used for constructing a CCT or TTT diagrams.

There is an ASTM publication with a designation of "A1033-10" available for quantitative measurement of phase transformations. In this study, this ASTM procedure was partially compiled in order to determine critical temperatures (Ac1, Ac3) and construct CCT and TTT diagrams.

2.8.3. Deformation Dilatometry

Deformation dilatometry is generally used for deforming the sample during thermal cycle and investigate the effects of deformation on the material properties. It can also be used for construction of time-temperature-transformation diagram after deformation and continuous-cooling-transformation diagram. However, in this study, deformation dilatometry was used as a mechanical property characterization tool as a function of temperature. Traditional principle of measuring length change with respect to temperature extended to include controlled deformation process with the help of a hydraulic press, close-loop servo, load cell and sensitive displacement measuring system. Solid steel samples can be compressed using various deformation-time-temperature programs in order to obtain flow-curves of material.

2.8.4. Stressed Dilatometry

Stressed dilatometry is used in order to observe the relation between stress and phase transformations. Critical temperatures for phase transformations can be affected from applied stresses when the stress is applied before initialization of decomposition of austenite into product phases. The same sample and dilatometer set-up as in the deformation dilatometry is used, however, the stress applied on the sample must be in the elastic region of the austenite phase at that temperature. Effect of stress on phase transformation varies with the changing magnitude and direction of force applied on sample.

CHAPTER 3

EXPERIMENTAL DETERMINATION OF MATERIAL PROPERTIES

3.1. Experimental Setup and Procedure

Experimental part of this study consists of dilatometry techniques, microstructural analysis for investigating the distribution and relative amount of phases for samples in CCT/TTT tests and retained austenite measurements by XRD.

3.1.1. Dilatometer

In this study, a dilatometer, DIL-805 A/D Baehr-Thermoanalysis GmbH (Figure 5) was used. It employs inductive heating, He/N_2 gas nozzle quenching and it is also capable of applying a uniaxial force simultaneously up to 20 kN in order to measure the dilation of steels as a function of temperature during thermal cycles. Dilatometer is located in Metal Forming Center of Excellence at Atılım University.

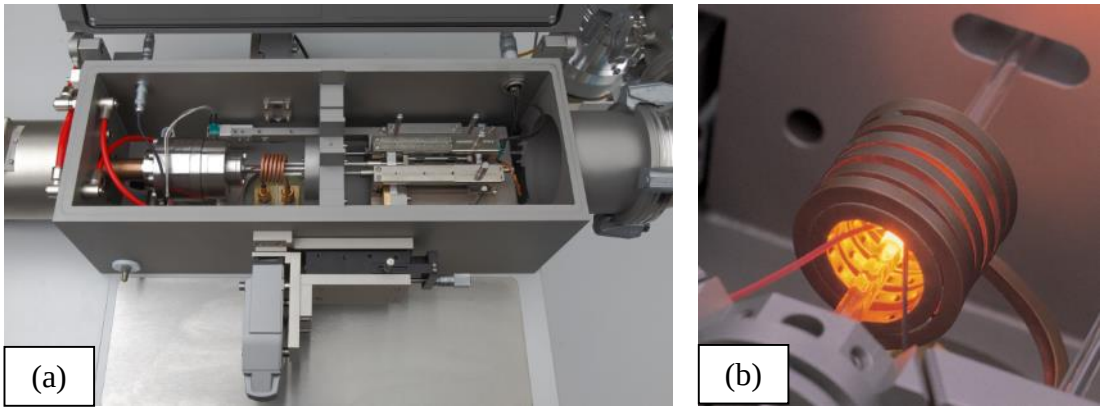

Figure 5: (a) Chamber of Baehr-Thermoanalysis GmbH, DIL 805 A/D dilatometer and (b) induction coil used in DIL 805 A/D.

The dilatometer uses water cooled copper coil (Figure 5 and Figure 6), which generates high frequency current in order to heat the specimens by induction. The coil consists of an additional perforated copper coil nested inside the induction coil as a part of cooling system for gas quenching. Cooling system uses Air, Ar, He or N_2 gases for gas nozzle quenching. Additionally, the cooling system might be supported with heat exchanger which is letting the inert gas passes through liquid N_2, and blown to the specimen in order to reach 2500 K/s cooling rate (only with thin-walled hollow sample).

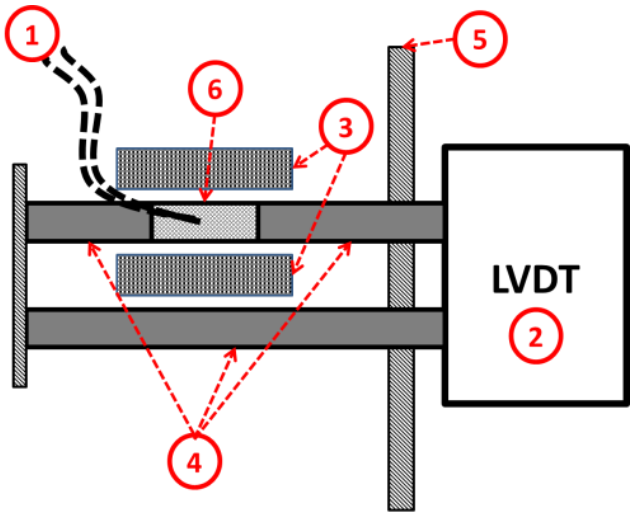

Figure 6: Schematic representation of DIL 805 A/D in quenching mode. ① $Pt_{90}Rh_{10}$–Pt (S-Type) thermocouple, ② LVDT, ③ Induction Coil, ④ Push rods, ⑤ Separation wall and ⑥ Specimen.

Length change is measured with linear variable differential transformer (LVDT) which is placed in the measuring head (Figure 6). The strain was measured longitudinally by LVDT. Push-rods, which might be made from fused silica SiO_2 or alumina Al_2O_3 (Figure 6), are used between specimen and LVDT in order to transmit dilation of specimen to the LVDT and hold the specimen inside the induction coil. Deformation punches, which might be made from fused silica SiO_2, alumina Al_2O_3 or silicon nitride Si_3N_4, are used together with push-rods in deformation dilatometry. LVDT and the specimen are separated and isolated from each other with a wall inside the chamber (Figure 6). Therefore, LVDT is not affected by heat radiation and

heat conduction generated from specimen (Figure 6). Resolution of the LVDT used in this dilatometer is 0.05 μm, which increases the sensitivity of the measurement.

$PtRh_{10}$-Pt (Type-S, 20 °C up to 1550 °C) or NiCr-Ni (Type-K, -200°C up to 1100°C) thermocouples can be used for temperature measurements. Thermocouples are spot welded on the specimen surface (Figure 6) before performing an experiment.

Large amount of heat loss might be expected during heating and also during isothermal dwell time by heat conduction and heat radiation over pushrods or deformation punches since they are in contact with the specimen. The heat loss is compensated with more heat input generated by induction coil in accordance with thermocouple readings.

Maximum allowed heating rate is 100 K/s and maximum cooling rate is 200 K/s for solid specimens. Both heating and cooling rates might be reach 4000 K/s and 2500 K/s respectively when thin-walled hollow specimen is used.

Specimen can be heated under the vacuum or inert gas atmosphere to prevent oxidation and decarburization of specimen. In this study, experiments performed under a vacuum of $5x10^{-5}$ mbar in order to avoid oxidation during thermal cycles.

3.1.1.1. Dilatometer Samples

Each dilatometry techniques uses their own specimen and they may vary in both length and diameter. In this study, there were four different types of dilatometry specimens used in the experiments:

1. Solid specimen with length of 10 mm and diameter of 5 mm (Figure 7.a) for deformation tests of austenitic and bainitic samples,
2. Solid specimen with length of 8 mm and diameter of 4 mm (Figure 7.b) for deformation tests of martensite,
3. Hollow specimen with length of 10 mm, diameter of 4 mm and bore diameter of 2 mm (Figure 7.c) for CCT/TTT tests,
4. Hollow specimen with length of 10 mm, diameter of 4 mm and bore diameter of 3.6 mm (Figure 7.d) for sub-zero tests,

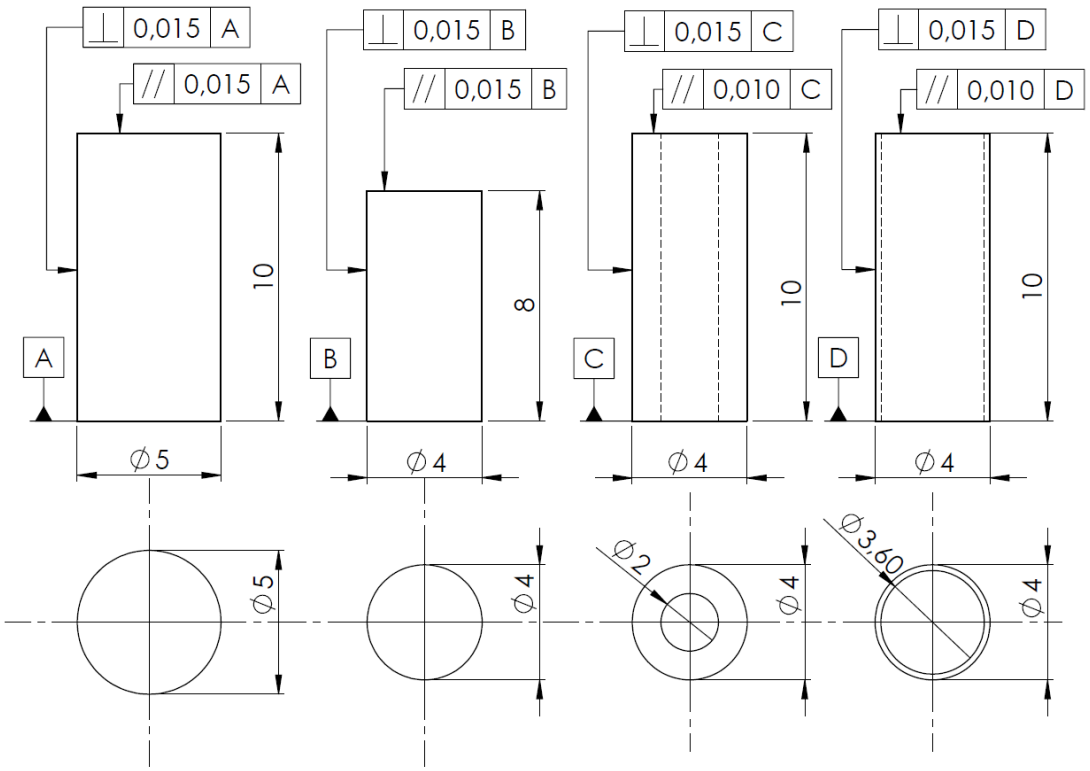

Figure 7: Dilatometer specimens; Ø5x10mm specimen for mechanical tests of bainite and austenite (a), Ø4x8mm specimen for mechanical tests of martensite (b), Ø4x10mm, bore diameter of Ø2mm specimen for CCT and TTT tests (c), Ø4x10mm, bore diameter of Ø3.96mm specimen for sub-zero tests (d).

3.1.1.2. Preparation of Dilatometer Samples

Specimens were extracted from length of 6000 mm and diameter of 37 mm as-cast and rolled 100Cr6 steel rods. Chemical composition of 100Cr6 bearing steel used in this study was given in Table 2. At first, 100Cr6 steel rod was sliced down to the length of 10 mm and then each slice was spheroidized in an atmosphere controlled spheroidization furnace at 790 °C for 14 hours in order to obtain same and homogenous microstructure in each specimen.

Table 2: Chemical Composition of 100Cr6 used in the study. Composition was given as Wt. (%).

	C	**Cr**	**Si**	**Mn**	**Al**	**Cu**	**Mo**	**Ni**	**O**	**P**
Wt. (%)	0.99	1.43	0.24	0.36	0.017	0.1	0.02	0.06	$5e^{-5}$	0.016

The specimens used for mechanical tests of bainitic and martensitic phases had been heat treated as in sliced form. Bainitic samples were obtained by austenitizing at 850°C for 30 minutes, then quenching to salt bath at 230°C and holding at that temperature for 4 hours. Same austenitization procedure applied for martensitic specimens, however specimens were oil quenched to 50 °C before liquid nitrogen treatment at -150 °C for 2 hours. After the heat treatment process of slices, dilatometer specimens were extracted from r/2 of sliced rods in order to eliminate the effect of core segregation Figure 8 by EDM.

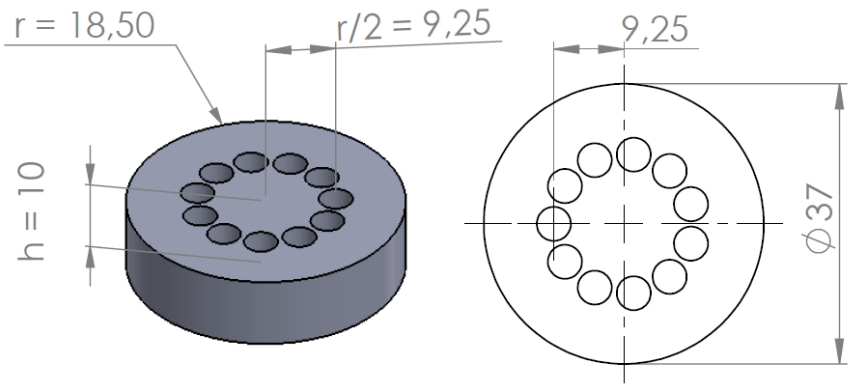

Figure 8: Position of the specimens extracted from sliced rod.

In this study, total 247 specimens were prepared for dilatometry experiments.

3.1.1.3. Temperature Programs used in Dilatometry Experiments

Dilatometry specimens are inductively heated and then cooled in accordance with the defined temperature programs. In this study, different temperature programs were used for each set of experiments. However, same austenitization procedure was used for entire set. Specimens used for mechanical tests of martensitic and bainitic phases had been prepared before performing the related tests as-martensitic and as-bainitic samples in order to reduce total duration of experiments by eliminating the standard austenitization segment in the temperature programs.

The standard austenitization segment used in each temperature program was determined according to bearing through-hardening process. Dilatometry samples were through-hardened in continuous heat treatment furnace and charged at different positions of conveyor belt of the continuous furnace.

Amount of retained austenite present in the microstructure of specimens after the through-hardening process were determined via XRD. The retained austenite amount of heat treated samples in furnace were approximately %13 ± 1.5 regardless to their position on conveyor belt. Verification tests were conducted in dilatometer with different heating rates and dwell times in order to reach the retained austenite value of heat treated samples at the continuous furnace.

After a series of verification tests, retained austenite value of the heat treated samples had been reached with an austenitization segment of heating rate with 4.7 °C/s, and a dwell time of 30 minutes at 850 °C for dilatometry samples. Temperature programs including austenitization segment at 850 °C briefly listed on Table 3.

Table 3: Details of dilatometer temperature programs used in tests.

Experiment	**Heating Rate**	**Dwell Time**	**Cooling Rate**	**Stress Applied**
Type	**[°C/s]**	**[min.]**	**[°C/s]**	**[Yes or No]**
CCT	4.7	30	Various $t_{8/5}$	No
TTT	4.7	30	100	No
Mech. Aust.	4.7	30	100	Yes
Mech. M. & B.	100	-	100	Yes
TRIP Martensite	4.7	30	100	Yes
TRIP Bainite	4.7	30	100	Yes
Sub-Zero	4.7	30	300	No

3.1.1.3.1. Temperature Programs used for CCT Tests

In CCT tests, $t_{8/5}$ characteristic times were used as cooling rates and specimens were cooled immediately after the standard austenitization segment. Characteristic time $t_{8/5}$ is often referred to the time interval that elapses during cooling of specimen from 800°C to 500°C.

Total 14 different characteristic times $t_{8/5}$ were used in CCT tests and are shown in Table 4. These $t_{8/5}$ times were selected for investigation of the bainitic and pearlitic phase transformation boundaries on CCT curve. First one (M) is applied for determination of martensite start temperature. Second series (B) was selected for investigating the critical points for bainitic transformation. Third one (B+P) is involving both pearlitic and bainitic transformations. Fourth and last one (P) includes only pearlitic transformation. A representative temperature program for CCT tests was given in Figure 9.

Experiments that are in the boundaries of each series were performed more than one. It is observed that the results of the repeated experiments were in good agreement and overlap each other smoothly. Therefore, experiment that is not in the critical range, was not repeated and its result assumed representative for each related set.

Table 4: List of specimens used in CCT tests with $t_{8/5}$ times.

Experiment Set	**Series**	**Sample ID**	**Characteristic Time $t_{8/5}$ [s]**
No0	M	029	2.00
No1		012, 013	14.00
No2		014	16.00
No3		015	20.00
No3.4	B	028	23.00
No3.7		025	27.00
No4		016, 022	30.00
No4.4		027, 103	36.00
No4.7		024, 102	40.00
No5	B+P	017, 023, 101	44.00
No6		018, 026, 100, 106	50.40
No7		019, 104	62.80
No8	P	020, 105	87.00
No9		021	150.00

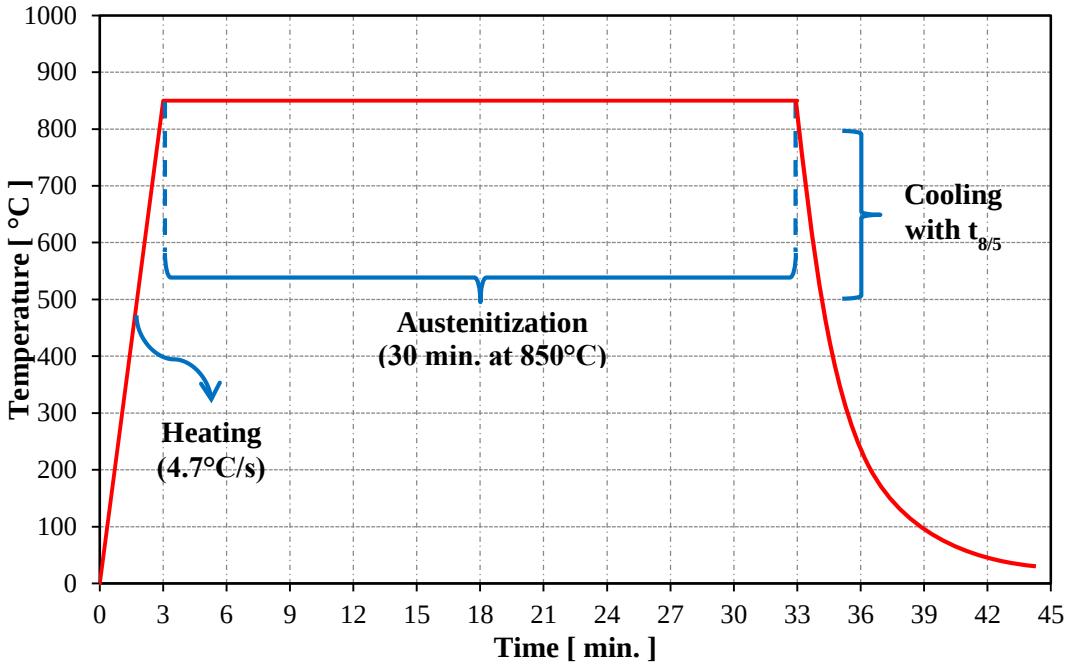

Figure 9: Representative Temperature Program for CCT Tests.

3.1.1.3.2. Temperature Programs used for TTT Tests

In TTT tests, subsequent to the standard austenitization segment, 100 °C/s cooling rate was applied to the specimens in order to cool it down to the isothermal hold temperature, at which phase transformation would like to be investigated. The temperature of the specimens were maintained at ±1 °C of isothermal hold temperature, while dilation of the samples were recorded. Specimen was kept at isothermal hold temperature until the completion of related phase transformation. Isothermal hold temperatures and dwell times for each TTT test were listed in Table 5. Furthermore, a representative temperature program for TTT tests was shown in Figure 10.

Experiments that are in the boundaries of each series were performed more than one. It is observed that the results of the repeated experiments were in good agreement and overlap each other smoothly. Therefore, experiments that are not in the critical range, were not repeated and its result assumed representative for each related set.

Table 5: List of specimens used in TTT tests.

Experiment Set	Sample ID	Isothermal Temp. [°C]	Dwell Time [s]
No300	052	300	4000
No350	051	350	1000
No400	046	400	400
No450	050	450	800
No475	049	475	6000
No500	048	500	2000
No550	047	550	800
No600	030, 043, 045	600	100
No650	044	650	100
No700	053	700	400

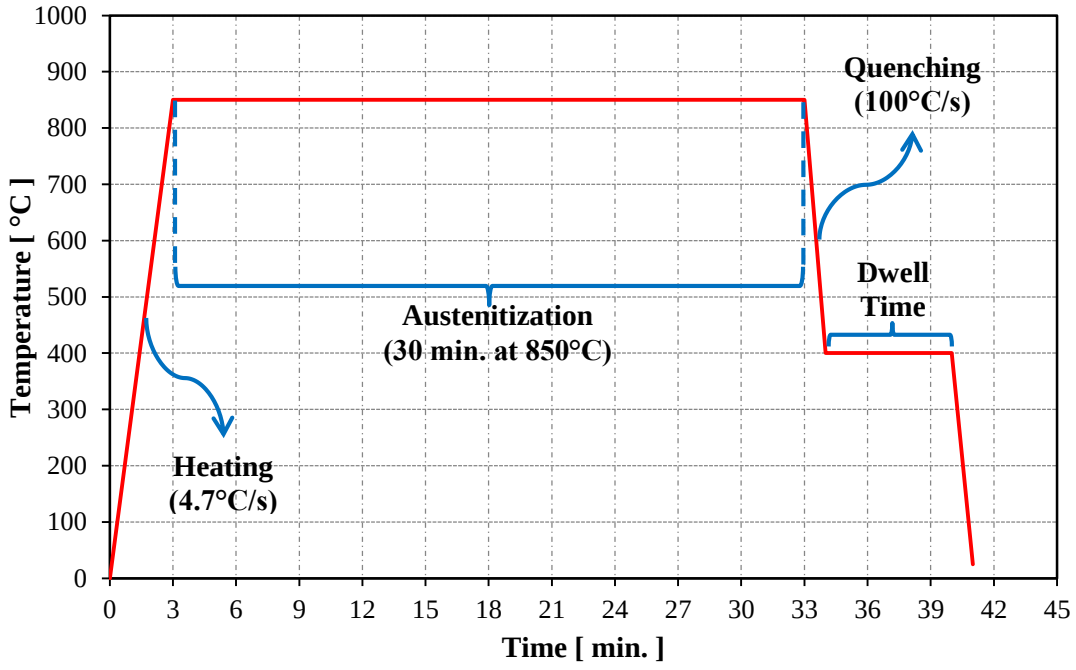

Figure 10: Representative temperature program for TTT tests.

3.1.1.3.3. Temperature Programs for Mechanical Tests of Austenite

In this set of experiments mechanical properties of meta-stable austenite wanted to be investigated. At first samples austenitized with standard austenitization segment, then immediately quenched to target temperature with 100 °C/s cooling rate. After the specimen reached the target temperature, compressive load was subsequently

applied to specimen with a strain rate of 0.01 s^{-1} at %2 strain. The temperature of the specimen was maintained at ±1 °C of hold temperature while both stress and strain of specimen were recorded. Specimen was kept at the hold temperature until %2 strain was given to specimen or until the applied load achieved to 2 kN. Parameters used in temperature programs of mechanical tests of austenite were given in Table 6. Moreover, representative temperature program for mechanical test of meta-stable austenite was given in Figure 11.

Table 6: Parameters used in temperature programs of mechanical tests of meta-stable austenite.

Experiment Set	**Sample ID**	**Temperature [°C]**	**Strain [%]**	**Strain Rate [s^{-1}]**
A850	009, 018, 905	850	2	0.01
A700	008, 017, 057	700	2	0.01
A600	007, 016, 052, 056	600	2	0.01
A500	006, 015, 050, 055	500	2	0.01
A400	005, 010, 014, 051	400	2	0.01
A300	012, 013	300	2	0.01

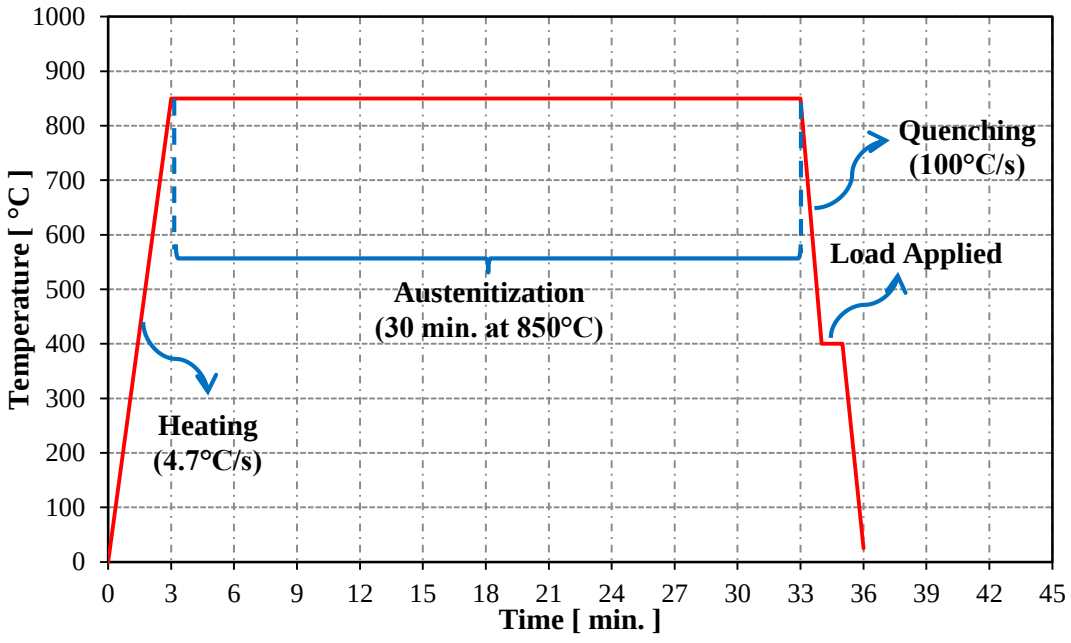

Figure 11: Representative temperature program for mechanical tests of meta-stable austenite.

3.1.1.3.4. Temperature Programs for Mechanical Tests of Martensite and Bainite

In mechanical tests of martensitic and bainitic phases, specimens had been already transformed to martensitic and bainitic phases. Therefore, it is only required to increase temperature of specimen up to hold temperature with a 100 °C/s heating rate at which the load would be applied. Compressive load was applied to the specimens at a given temperature, same as the mechanical tests of meta-stable austenite with a strain rate of 0.01 s^{-1} at %2 strain. Specimen was kept at ±1 °C of hold temperature until %2 strain was given to specimen or until the applied load achieved to 2 kN. Details of temperatures and parameters used in mechanical tests of bainitic and martensitic phases were given in Table 7 and Table 8 respectively. Furthermore, representative temperature program for mechanical tests of bainitic and martensitic phases was given in Figure 12.

Table 7: Parameters used in temperature program of mechanical tests of bainite.

Experiment Set	Sample ID	Temperature [°C]	Strain [%]	Strain Rate [s^{-1}]
B600	021, 031, 037, 150, 151	600	2	0.01
B500	022, 032, 038, 152, 153	500	2	0.01
B400	033, 039, 154, 155, 156	400	2	0.01
B300	029, 034, 040, 157	300	2	0.01
B200	029, 035, 041, 158	200	2	0.01
B100	030, 036, 042	100	2	0.01

Table 8: Parameters used in temperature program of mechanical tests of martensite.

Experiment Set	Sample ID	Temperature [°C]	Strain [%]	Strain Rate [s^{-1}]
M450	102, 131, 140	450	2	0.01
M400	107, 108, 133, 141	400	2	0.01
M300	110, 123, 132, 134, 138	300	2	0.01
M200	111, 112, 135, 136, 137	200	2	0.01
M100	113, 114, 125, 130, 139	100	2	0.01

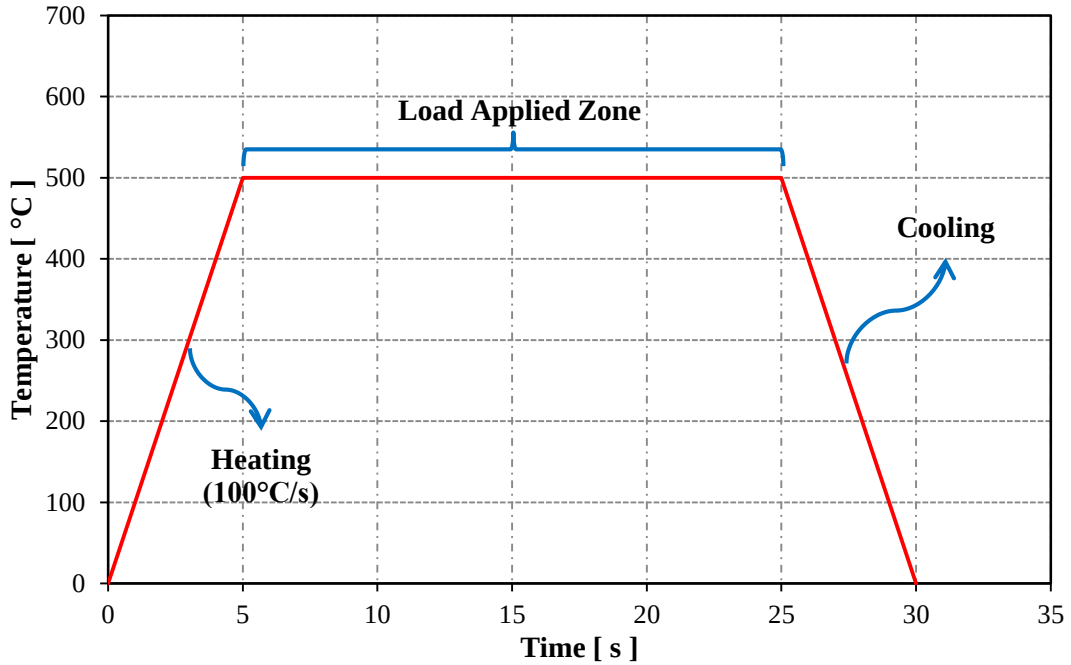

Figure 12: Representative temperature program for mechanical test of bainitic and martensitic phases.

3.1.1.3.5. Temperature Programs used in TRIP Tests for Bainitic Transformation

In TRIP tests of bainitic phase transformation, the effect of stress on phase transformation of austenite to bainite was investigated. Specimen, at first austenitized with the standard austenitization segment, and subsequently cooled down from 850 °C to 350 °C with 100 °C/s cooling rate. Temperature of the specimen was stabilized in the third step of temperature program for 1.5 seconds. After the temperature stabilization step, specimen was loaded immediately with various compressive forces which were given in Table 9. The load on specimen was held constant until the end of isothermal dwell time for letting to complete phase transformation of austenite to bainite took place. The loads applied to the specimens were always below the yield strength of austenite at a temperature of 350 °C, which was calculated as 178 MPa in mechanical tests of meta-stable austenite. Representative temperature program for TRIP tests of bainitic transformation was given in Figure 13.

Table 9: Loads applied on specimens at TRIP tests of bainitic phase transformation.

Experiment Set	Sample ID	Applied Stress [MPa]
No0	604	0
No5	651, 654	5
No20	652, 655	20
No40	656, 657	40
No50	650, 653	50
No100	600, 602	100

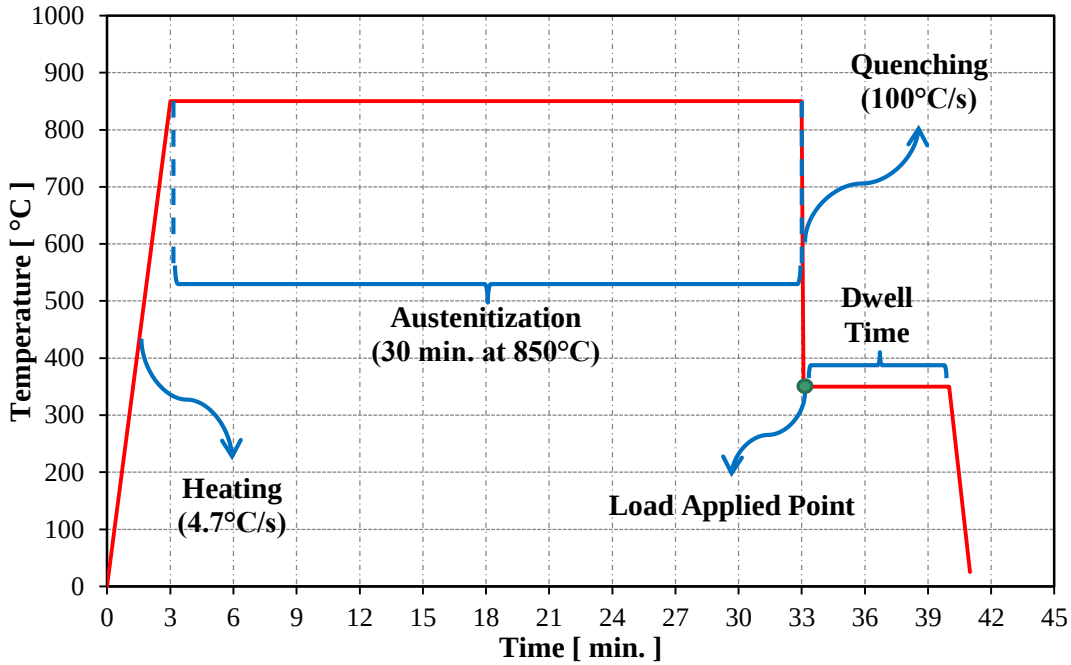

Figure 13: Representative temperature program for TRIP tests of bainitic phase transformation.

3.1.1.3.6. Temperature Program used in TRIP Tests for Martensitic Transformation

In TRIP tests of martensitic phase transformation, the effect of stress on displacive austenite to martensite phase transformation was investigated. Temperature program is same as in temperature program of TRIP tests of bainitic phase transformation. Same austenitization segment was applied and after the austenitization, specimen was cooled down to temperature of 350 °C as in TRIP tests of bainitic transformation. However, austenite to martensite phase transformation is known as displacive phase transformation. Hence, in order to investigate the stress effect,

various compressive forces were applied on the specimens immediately after target temperature of 350 °C was achieved. In the next step, specimen was cooled down to the room temperature (25 °C) with 10 °C/s cooling rate, while load on the specimen was held constant during cooling. The loads applied to the specimens were always below the yield strength of austenite at temperature of 350 °C. Detailed information about the parameters used in TRIP test of martensitic phase transformation can be found in Table 10. Furthermore, representative temperature program for TRIP test of martensitic phase transformation was shown in Figure 14.

Table 10: Loads applied on specimens at TRIP tests of martensite phase.

Experiment Set	**Sample ID**	**Applied Stress [MPa]**
No0	681, 684	0
No5	680, 686	5
No50	682, 687	50
No100	683, 685	100
No200	688	200
No300	689	300

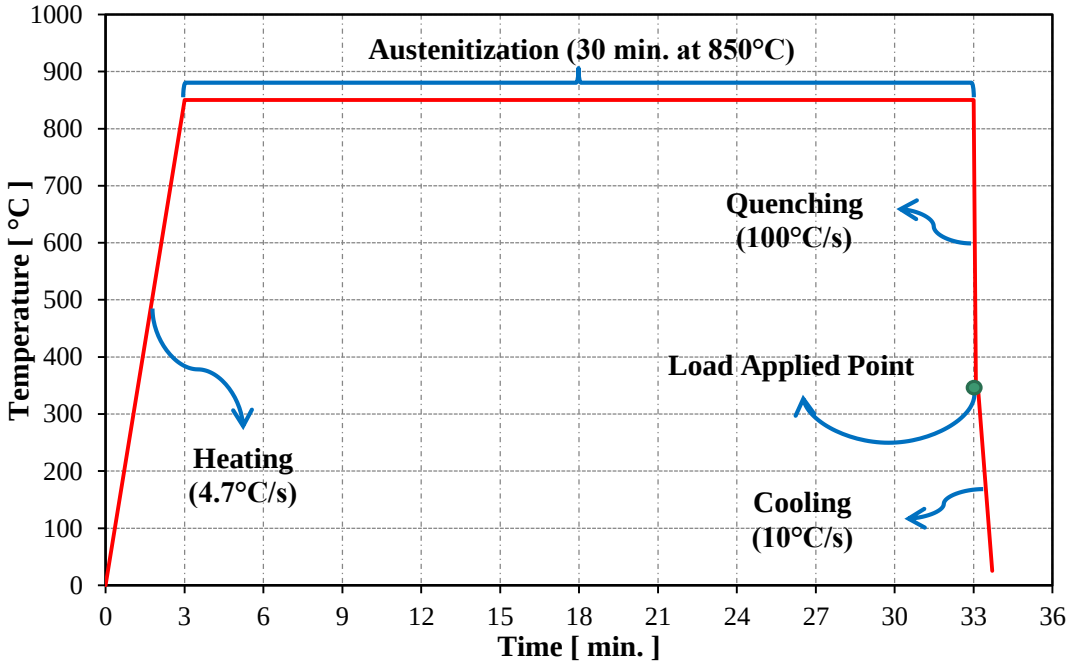

Figure 14: Representative temperature program for TRIP test of martensite phase.

3.1.1.3.7. Temperature Programs used for Sub-Zero Tests

Investigation of complete martensitic phase transformation is aimed in the sub-zero tests. Specimen was first austenitized then quenched down to -135°C with 300 °C/s cooling rate while dilation of the specimen is recorded. A representative temperature program for sub-zero tests was given in Figure 15.

There are total 7 tests conducted in these set of experiments, however, 5 of them were failed because they could not have achieved the targeted temperature (-135 °C). Eventually, two experiments were successfully conducted and analyzed.

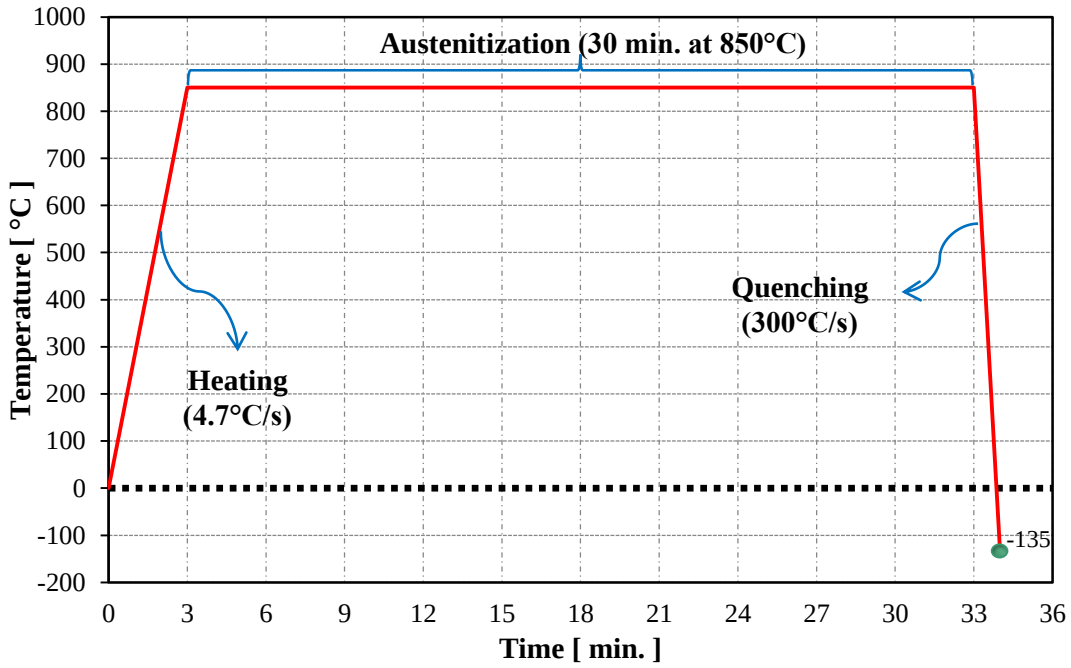

Figure 15: Representative temperature program for sub-zero tests.

3.1.2. XRD

Seifert XRD 3003 PTS is the XRD used in the study for measuring amount of retained austenite present in the microstructure of samples after performing the dilatometry tests or furnace experiments. The XRD system located in the R&D Department of ORS Bearings Inc.

The system basically consists of three parts, which are X-Ray generator tube, goniometer and X-Ray detector. The components of XRD system are shown and labeled in Figure 16.

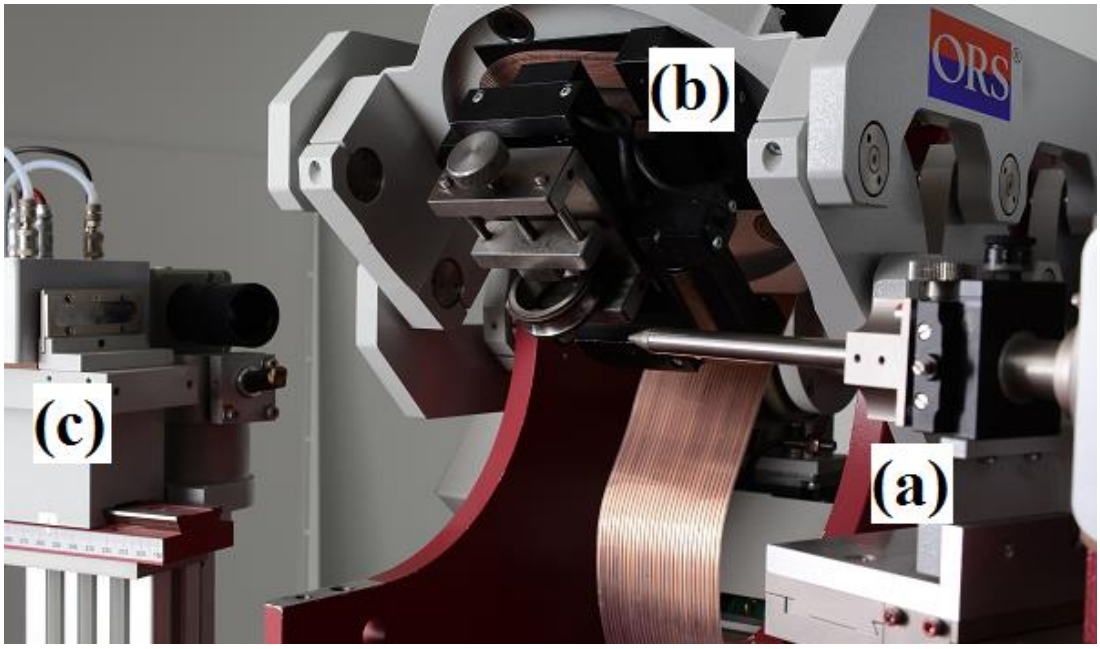

Figure 16: X-Ray Diffractometer (XRD), Seifert 3003 PTS. (a) X-Ray Generator Tube, (b) 5-Axis Goniometer and (c) Position Sensitive Detector (PSD).

X-Ray generator tube is the source of X-Rays produced and it is guided with collimator to the measurement point on specimen. 7-Axis goniometer is used on the system and the main purpose of the goniometer is moving the specimen in accordance with detector in order to have 2θ angle always be conserved between tube axis and detector axis at the measuring point. The detector used in the system is Position Sensitive Detector (PSD) in order to detect X-Rays diffracted from measurement point on the specimen.

3.1.3. SEM

Zeiss Evo LS15 SEM with LaB_6 filament at acceleration voltage of 0.2 - 30 kV was used for microstructural analysis of specimens. Resolution of the SEM is up to approximately 2 nm, and 1.000.000X magnification can be reached with using LaB_6 filament. Theoretical working distance is 8.5 mm and pressure range is 10 to 3000

Pa. Dimensions of chamber are diameter of 365 mm and height of 275 mm. SEM is located in Metal Forming Center of Excellence at Atılım University.

3.2. Evaluation Procedures and Results

Evaluation procedures and results for each experiment set were given in following subdivisions. Experimental results of 162 specimens were evaluated at dilatometry side of the work and details about the amount of evaluated specimens can be found in Table 11.

Table 11: Number of experiments evaluated in this study.

Experiment Set	**Evaluated Specimen**
CCT Experiments	25
TTT Experiments	12
Mechanical Experiments	89
TRIP Experiments	29
Sub-Zero Experiments	7
Total	**162**

3.2.1. Evaluation of a Dilatometric Curve

The dilation of specimen is measured and recorded during heating and cooling cycles by dilatometer. The relative change in length versus time or temperature plot known as the dilatometric curve. Evaluation of a dilatometric curve (Figure 17) is explained in this sub-division step by step. First of all, the dilatometric curve can be divided into four segment for this purpose. Straight lines on dilatometric curve usually commented as expansion or contraction during heating or cooling. Therefore, it can be commented as the segment A-B of the dilatometric curve in Figure 17 represents the thermal expansion during heating of the specimen. Change in slope observed on the dilatometric curve is often commented as commencing or completion of phase transformations. Thus, it can be said that, at the B-C segment of Figure 17 spheroidite to austenite phase transformation is took place. Change in length at constant temperature is not desired if specimen is not loaded. It can be actually

defined as an experimental error due to mostly thermal expansion of push-rods and it must be compensated in the numerical analysis part of the test. In this study, austenitization of specimen was completed in 30 minutes at 850 °C and within this time interval length change had been increased as it can be seen at C-D segment of Figure 17. This was due to thermal expansion of the silica push-rods used in dilatometer and also due to dissolution of carbide particles in austenite during austenitization of specimen. Expansion of silica push rods was compensated in numerical analysis part by shifting the point D together with D-E segment to the point "C" in Figure 17.

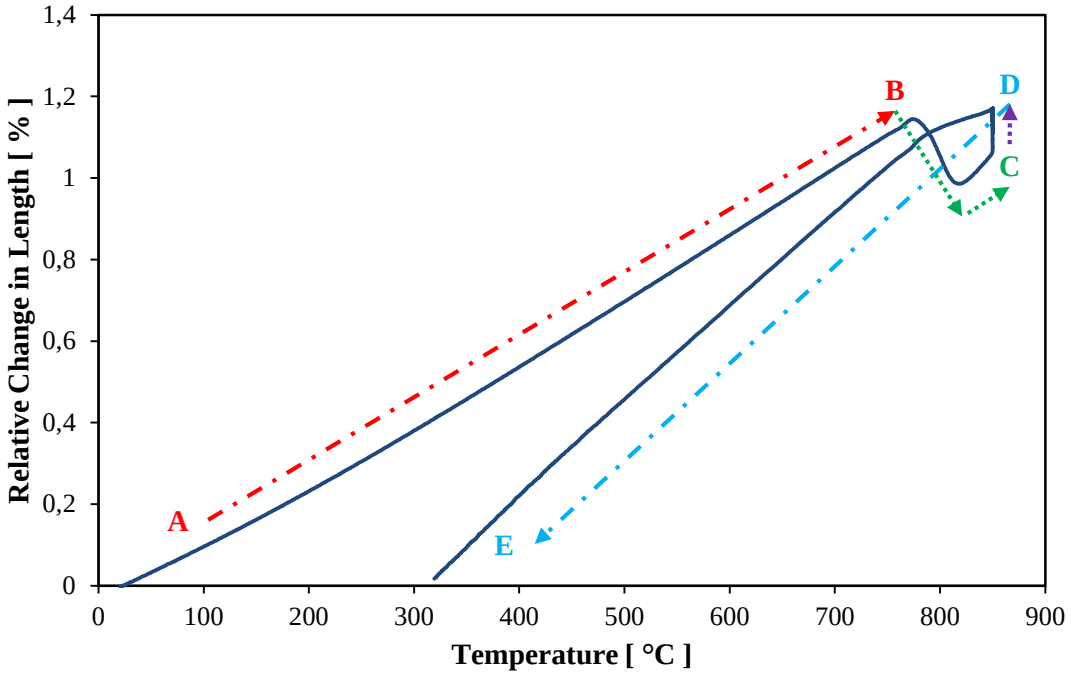

Figure 17: Relative change in length vs. temperature plot. "A-B" is heating segment, "B-C" is spheroidite to austenite phase transformation, "C-D" refers to thermal expansion of push rods, "D-E" is the cooling segment.

3.2.2. Determination of Time-Temperature-Transformation (TTT) Diagram

The progress of isothermal phase transformation can be estimated by commenting on dilatometric curve at isothermal hold temperature. There were total 10 tests conducted and details about these tests were given in Table 5.

3.2.2.1. Evaluation Procedure of TTT Tests

Evaluation procedure used for TTT tests might be explained with a representative example as following. Relative change in length versus time plot of test No300-052 is given in Figure 18. Time axis (x-axis) of this plot was re-arranged by defining end point of austenitization segment as the initial point for transformation. Specimen used in test No300-052 was quenched from 850 °C to 300 °C with 100 °C/s cooling rate with a dwell time of 4000 seconds in order to investigate isothermal phase transformation at 300 °C. Initial increase in strain observed at isothermal segment refers to the commencing of phase transformation while temperature remains constant.

Once the phase transformation completed, length of the specimen does not change. Initial and final points of phase transformation can be obtained simply by drawing horizontal tangent lines onto minimum and maximum strain points respectively as in Figure 18.

Austenite to bainite transformation was started at point “A” and completed at point “B” as it can be seen in Figure 18 with a form like S-shaped curve. It was assumed that, point “A” refers to %1 transformation and point “B” refers to %99 transformation completed for bainitic phase.

The graphical evaluation for determination of critical points of a TTT test is explained in previous passage, but the main drawback for evaluation procedure of TTT tests is theoretical determination of the critical points.

Kinetics of isothermal phase transformation of austenite can be well described by Johnson-Mehl-Avrami Equation (1) as explained in Chapter 2. Therefore, JMA equation was fitted onto the test results one by one for theoretical determination of critical points. For this purpose, relative change in length versus time plot must be converted into the phase fractions since JMA Equation is related with phase fractions and time.

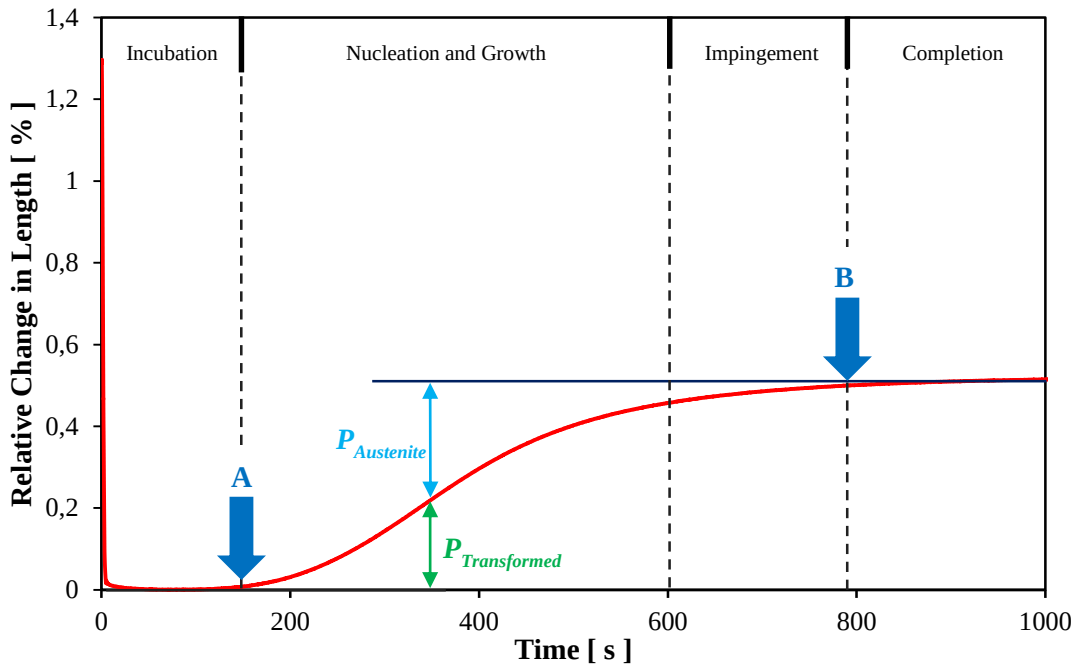

Figure 18: Relative change in length vs. time plot. Point "A" refers to %1 of transformation and point "B" refers to %99 of transformation.

In order to convert dilatometric curve into the phase fractions, linear mixing rule of dilation was used for phase transformations (21):

$$P(t) = \frac{l(t) - l_i(t)}{l_f(t) - l_i(t)} \tag{21}$$

where, $P(t)$ is phase fraction, $l(t)$ is length change at a given time *t* on dilatometric curve, $l_i(t)$ is intersection of horizontal line that is tangent to the minimum length change at time *t*, $l_f(t)$ is the intersection of time and horizontal line which is tangent to maximum point of the change in length shown on Figure 18. By using Equation (21), dilatometric curves were converted into percent phase transformed versus time plots as in Figure 19. JMA Equation was fitted on each transformation curve of TTT tests by reducing total RMS error with iterating the JMA parameters, isothermal rate constant *k(T)* and time exponent *n(T)*. S-Shape transformation curve and JMA fittings for four TTT tests can be seen in Figure 19.

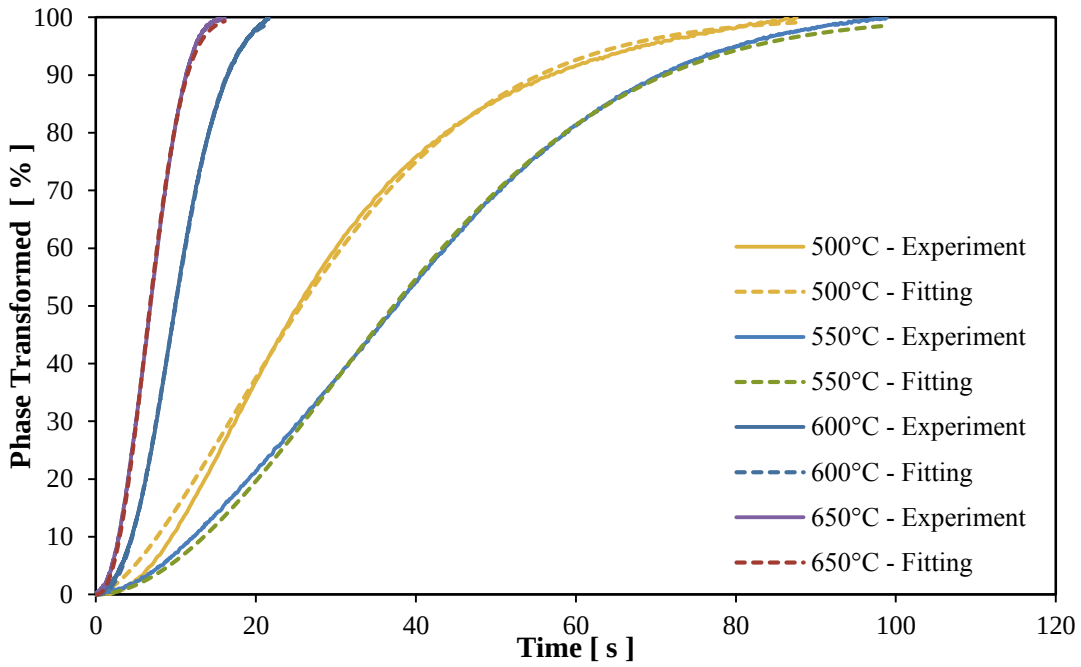

Figure 19: JMA fitted, % Phase transformed vs. time plot of some experiments.

This evaluation procedure applied for all set of TTT tests in order to determine critical points for phase transformations at related temperatures and results were given in the following topic. After determination of the critical points TTT diagram for 100Cr6 was plotted by connecting these critical points in accordance.

3.2.2.2. Results of TTT Tests

As it can be seen from the Figure 19 transformation curves and JMA fittings are in good agreement. Times for %1 and %99 transformations were calculated and obtained from these fittings. After calculation of critical times for transformation, they were connected with related temperatures in accordance in order to plot TTT diagram for steel 100Cr6 which is given in Figure 20. This TTT diagram is only valid for 30 minutes of austenitization at 850 °C. Moreover, TTT diagram found in the literature and computed by JMatPro® were also given in the figure as dashed lines in order to make a comparison with experimentally determined diagram.

Exponent *n* of the JMA Equation was calculated for each isothermal testing temperature and its' value varies between 1.56 and 2.4. It is known that the value should be vary between 1 and 4 by definition.

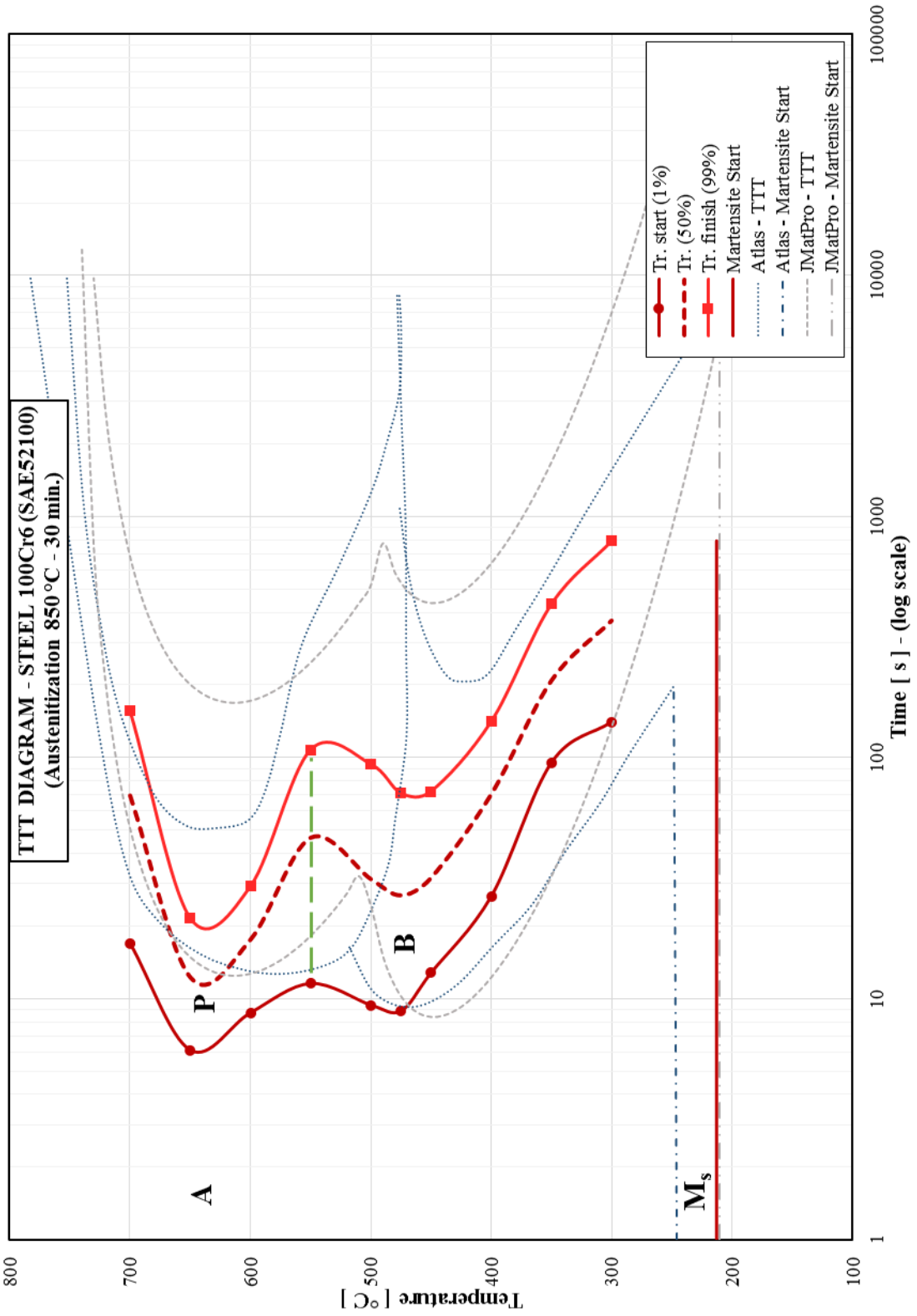

Figure 20: TTT Diagram of Steel 100Cr6. Austenitized at 850 °C for 30 minutes. Computed TTT Diagram with JMatPro and TTT Diagram given in Atlas [65] (Austenitization 860°C – 15 min.) also plotted for comparison.

The TTT diagram obtained from experiments is similar to diagram found in the literature [65] and the diagram computed via JMatPro®. The difference observed between the diagrams might be explained with differences in their austenitization conditions and differences in chemical compositions of 100Cr6. It is known that the amount of carbide dissolved in the austenite and chemical composition of the steel may affect the phase transformations. Therefore, TTT diagrams might be affected and shifted to shorter or longer times. Experimental conditions and evaluation procedures/methods can also be reasons of difference between the diagrams.

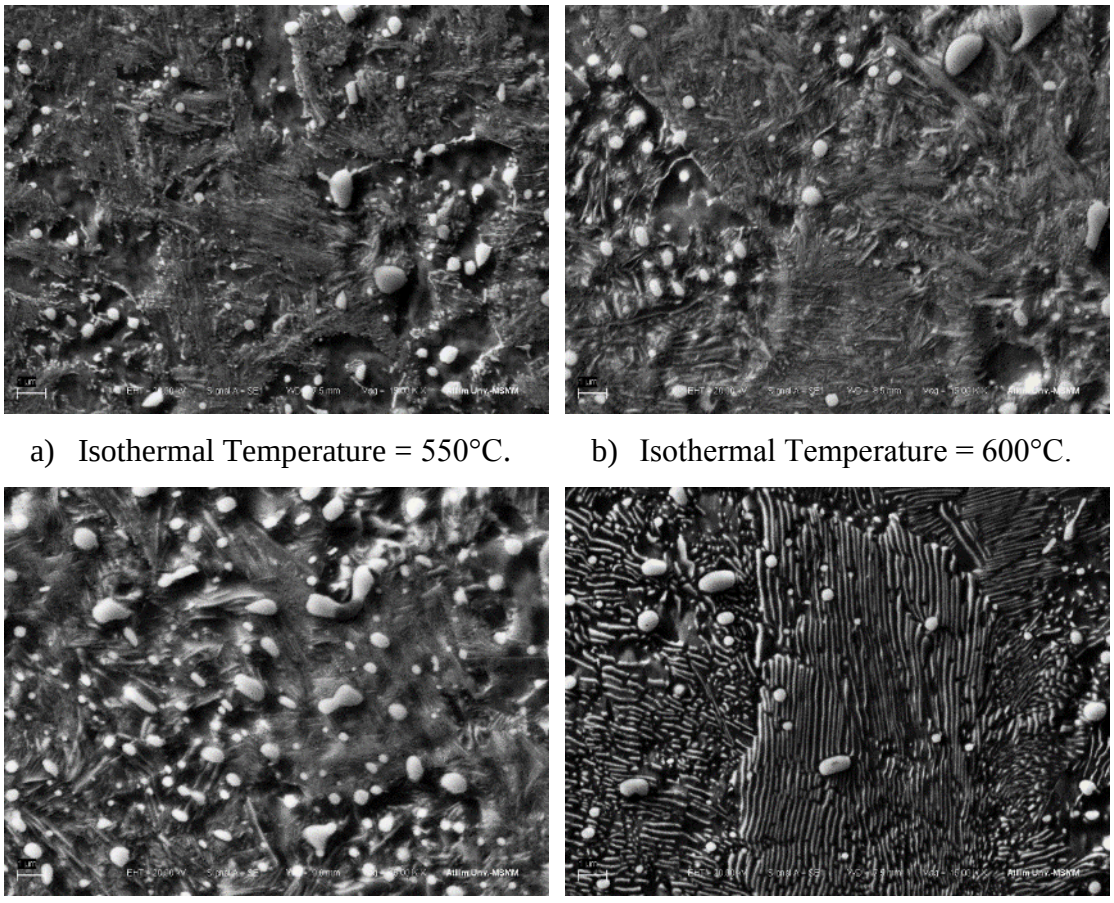

a) Isothermal Temperature = 550°C. b) Isothermal Temperature = 600°C.

c) Isothermal Temperature = 650°C. d) Isothermal Temperature = 700°C.

Figure 21: SEM Images of TTT specimens after experiments performed at various temperatures, x15000 magnification, and pearlitic microstructure with spheroidized carbides (bright).

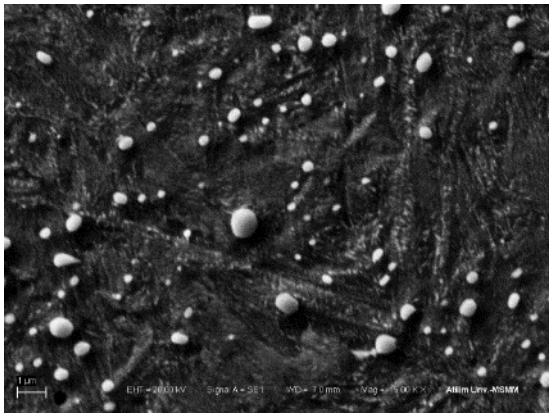

a) Isothermal Temperature = 300°C.

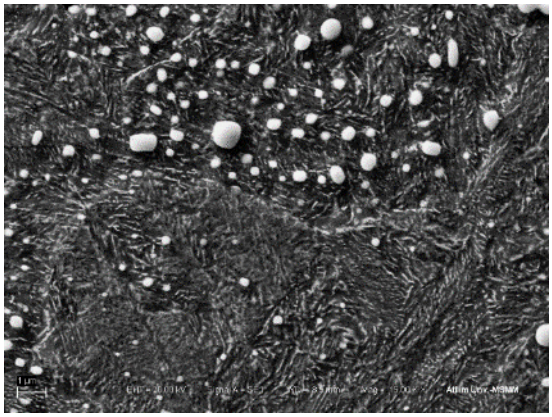

b) Isothermal Temperature = 350°C.

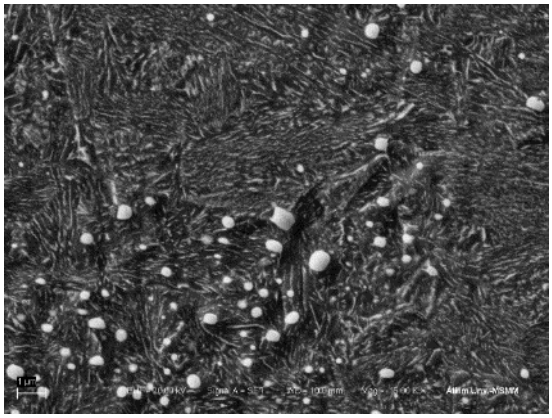

c) Isothermal Temperature = 400°C.

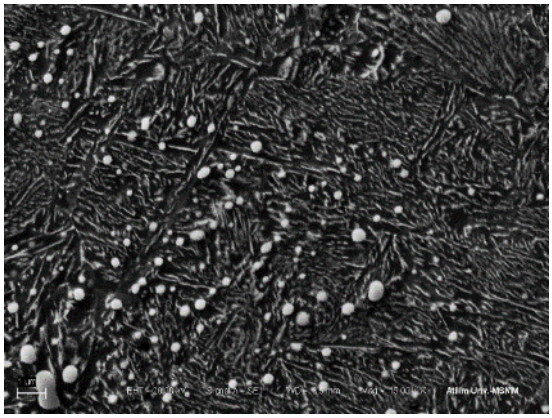

d) Isothermal Temperature = 450°C

e) Isothermal Temperature = 475°C

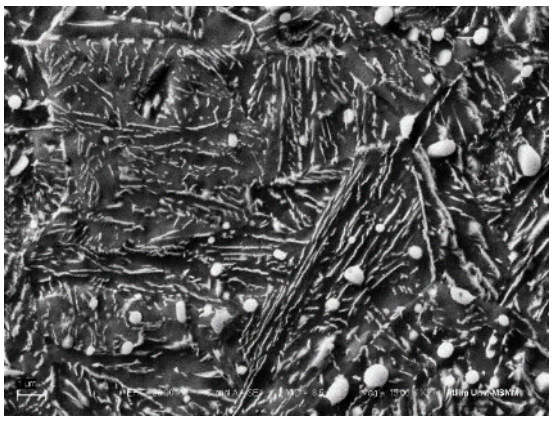

f) Isothermal Temperature = 500°C

Figure 22: SEM Images of TTT specimens after experiments performed at various temperatures, x15000 magnification, and bainitic microstructure with spheroidized carbides (bright).

SEM images of specimens are given in Figure 21 and Figure 22 with a same level of magnification (x15000). As it can be seen from all images, spheroidized carbide particles had not been completely dissolved in the austenite phase during austenitization so, undissolved spheroidized carbide particles (bright spheres) are present in the microstructures. Bainitic matrix can be observed on images of tests conducted below 550 °C. On the other hand, pearlitic matrix introduced as expected into the microstructures at temperatures above 550 °C. Moreover, transition from lower bainite to upper bainite can be seen in Figure 22 in conjunction with increasing the isothermal hold temperature from 300 °C to 550 °C. On the other side, coarse pearlite matrix and coarse pearlite lamellas can be clearly seen on Figure 21.Test results and microstructural images are in good agreement as expected. As a results, experimentally determined TTT diagram for 100Cr6 was verified with these microstructural images.

3.2.3. Determination of Continuous Cooling Transformation (CCT) Diagram

CCT diagram is more applicable in terms of continuous cooling processes such as quenching. Experimental determination of CCT diagram involves dilatometric experiments and evaluation procedure that are similar with TTT tests. Various $t_{8/5}$ characteristic times were used as cooling rates in CCT tests. There were total 25 experiments performed in order to plot CCT diagram of 100Cr6. The detailed information about experiments can be found in Table 4.

3.2.3.1. Evaluation Procedure of CCT Tests

Experiment No6-026 might be given as an example for the evaluation procedure of CCT tests. Hollow specimen was used in the test. At the beginning, it was austenitized, then cooled down to room temperature with an exponential cooling curve which was determined by $t_{8/5}$ characteristic time of 5.95 seconds.

As mentioned before, change in slope on the dilatometric curve is often commented as commencing or completion of phase transformations. It is expected that derivative of the dilatometric curve $d\left(\left(\frac{\Delta L}{L_0}\right)/L_0\right)/dT$ deviates from linearity during cooling as it can be seen at point "A" in Figure 23. Thus, this point can be commented as the

beginning of phase transformation. Derivative, $d\left((\frac{\Delta L}{L_0})/L_0\right)/dT$ returns linearity at point “B” as shown in Figure 23, which means phase transformation of austenite to ferrite partially completed. This evaluation procedure was applied to all CCT tests in order to determine critical points for phase transformations observed during CCT tests.

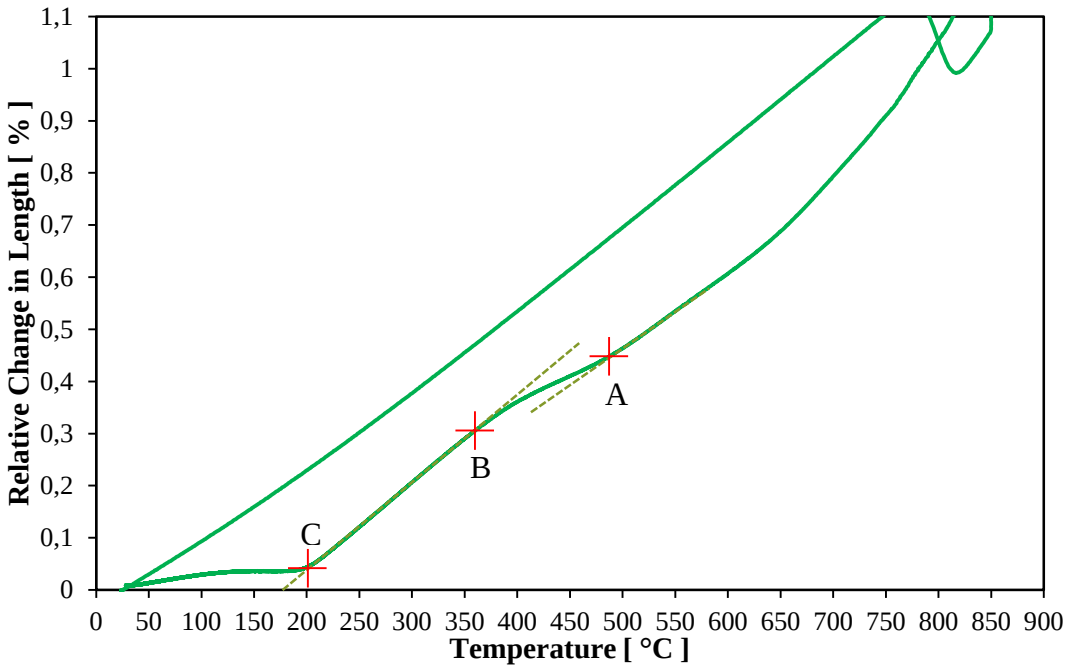

Figure 23: Relative change in length vs. temperature plot for CCT test No6-026. Point “A” represents beginning of austenite to bainite transformation, point "B" represents completion of austenite to bainite transformation and point "C" commented as the beginning of austenite to martensite transformation.

3.2.3.2. Results of CCT Tests

CCT diagram of 100Cr6 bearing steel was plotted by connecting determined critical points and it was given in Figure 24. This CCT diagram is only valid for 30 minutes of austenitization at 850 °C. Moreover, CCT diagram found in literature and diagram computed with JMatPro® were also given in the same figure as dashed lines in order to make a comparison with experimentally determined diagram. CCT diagrams are in good agreement. Differences observed between diagrams might be due to difference in composition or/and experimental conditions.

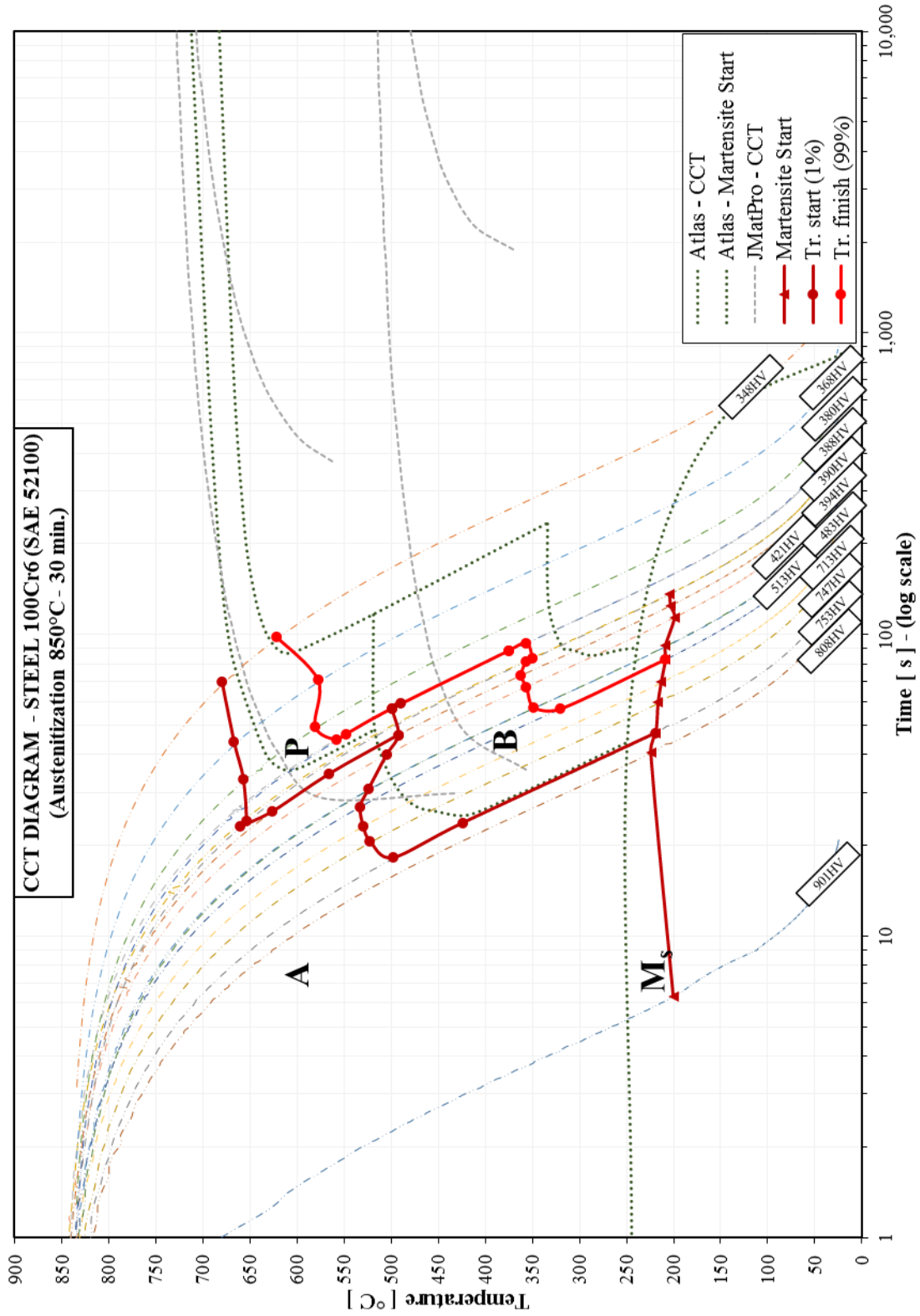

Figure 24: CCT diagram of steel 100Cr6. Diagram computed via JMatPro® and diagram found in Atlas [65] (Austenitization 860°C – 15 min.) also plotted for comparison. Cooling curves and hardness values are also indicated.

SEM images of specimens are given in Figure 25 to Figure 37 with a same level of magnification (10K X). As it can be seen from all images, spheroidized carbide particles had not been completely dissolved in the austenite phase during austenitization so, undissolved spheroidized carbide particles (bright spheres) are present in the microstructures. It must be noted that images are not clearly identified since during the continuous cooling multiple phase transformations are took place as expected.

Clear images were also obtained at a higher magnifications like 30K X for some specimens. However, it is not applicable for all specimens due to focusing problems encountered in SEM. In these set of images, images were intended to be given in same magnification level in order to compare them with each other.

A quantitative amount of phases or relative phase fractions could not obtained from these images. Nevertheless, traces of expected phases were observed at a higher magnifications as 30K X.

Test results and microstructural images are in good agreement as expected. As a results, experimentally determined CCT diagram for 100Cr6 was verified with these corresponding microstructural images.

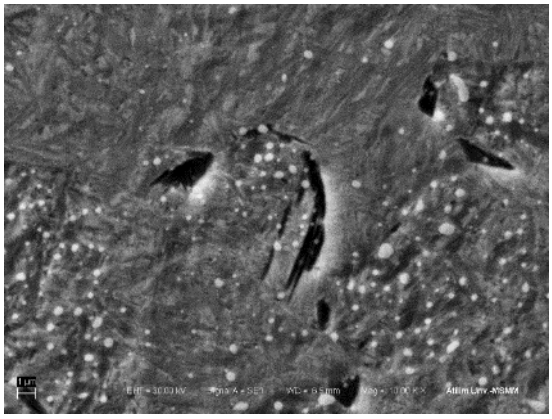

Figure 25: SEM Image of test No1 with $t_{8/5}$: 14 s. 10K X magnification. Martensitic microstructure with some spheroidized carbides (bright).

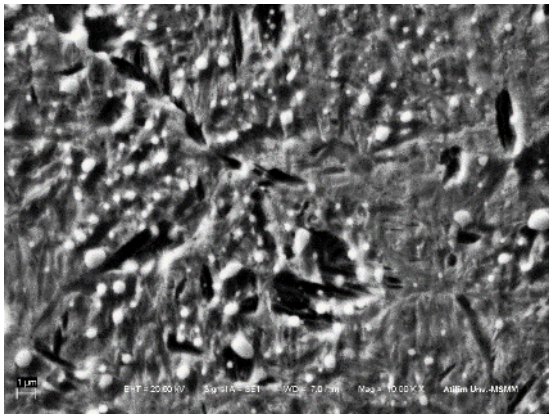

Figure 26: SEM Image of test No2 with $t_{8/5}$: 16 s. 10K X magnification. Martensitic and bainitic microstructure with spheroidized carbides (bright).

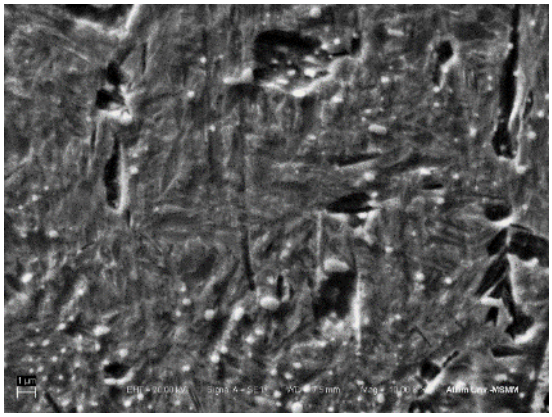

Figure 27: SEM Image of set No3 with $t_{8/5}$: 20 s. 10K X magnification. Martensitic and bainitic microstructure.

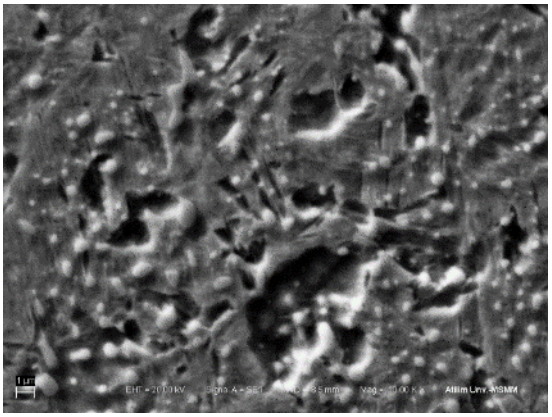

Figure 28: SEM Image set No3.4 with $t_{8/5}$: 23 s. 10K X magnification. Martensitic and bainitic microstructure.

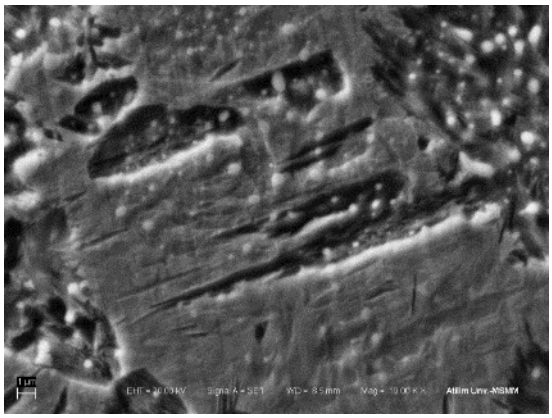

Figure 29: SEM Image of set No3.7 with $t_{8/5}$: 27 s. 10K X magnification. Martensitic and bainitic microstructure.

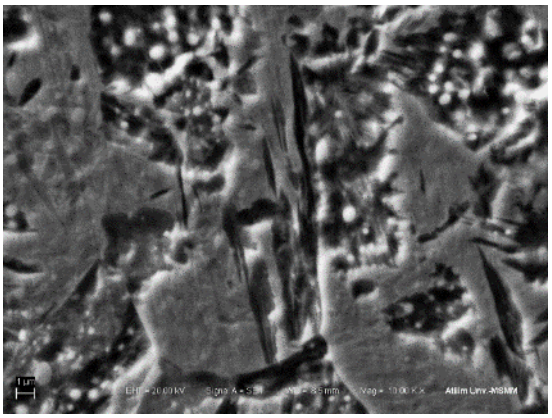

Figure 30: SEM Image set No4 with $t_{8/5}$: 30 s. 10K X magnification. Martensitic and bainitic microstructure.

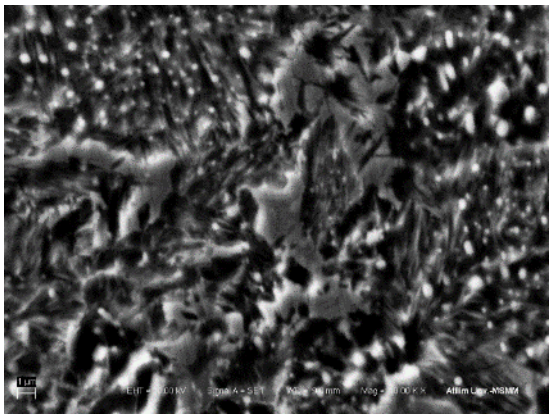

Figure 31: SEM Image of set No4.4 with $t_{8/5}$: 36 s. 10K X magnification. Martensitic and bainitic microstructure.

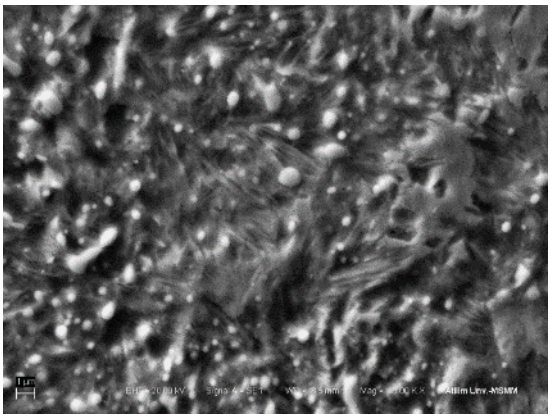

Figure 32: SEM Image of set No4.7 with $t_{8/5}$: 40 s. 10K X magnification. Pearlitic and bainitic microstructure.

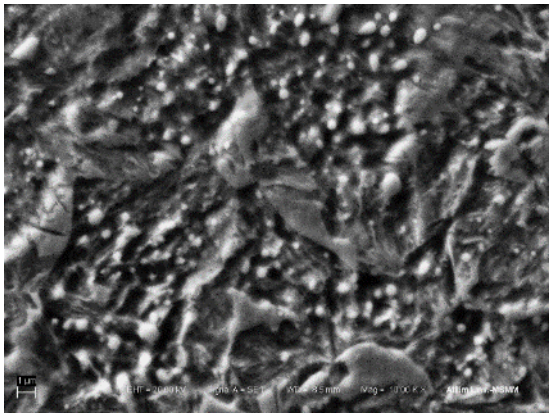

Figure 33: SEM Image of set No5 with $t_{8/5}$: 44 s. 10K X magnification. Pearlitic and bainitic microstructure.

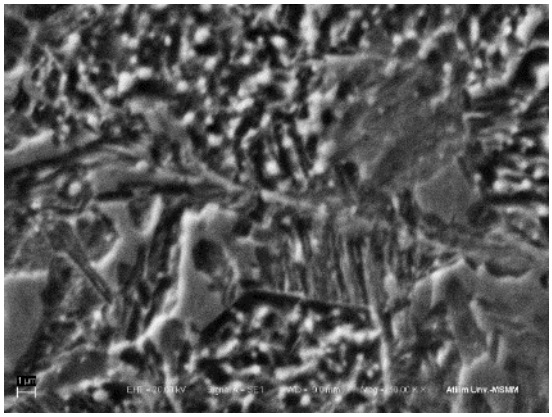

Figure 34: SEM Image of set No6 with $t_{8/5}$: 50.4 s. 10K X magnification. Pearlitic and bainitic microstructure.

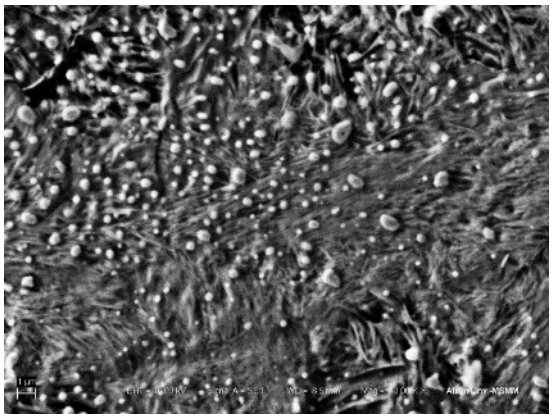

Figure 35: SEM Image of experiment from set No7 with $t_{8/5}$: 62.8 s. 10K X magnification. Pearlitic microstructure with spheroidized carbides (bright).

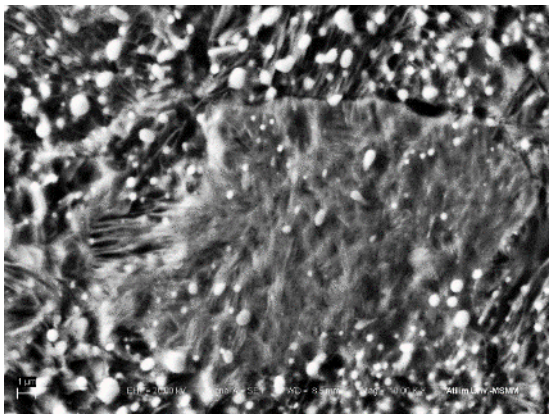

Figure 36: SEM Image of experiment from set No8 with $t_{8/5}$: 87 s. 10K X magnification. Pearlitic microstructure with spheroidized carbides (bright).

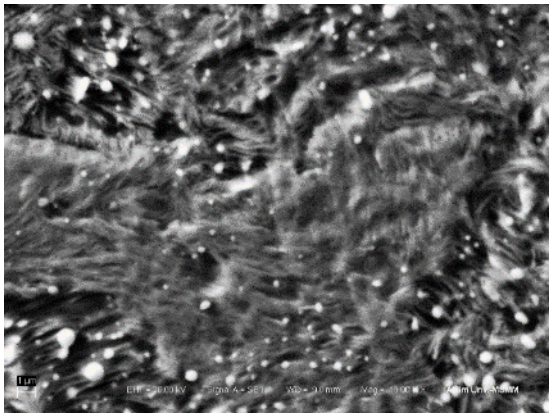

Figure 37: SEM Image of experiment from set No9 with $t_{8/5}$: 150 s. 10K X magnification. Pearlitic microstructure with spheroidized carbides (bright).

3.2.4. Determination of Critical Temperatures (Ms, Mf, Bs, Ac1 and Ac3)

Critical temperatures that were described in this section are martensite start temperature, martensite finish temperature, bainite start temperature, *Ac1* and *Ac3* temperatures.

Bainite start temperature (B_s) can be defined as the temperature at which austenite to bainite transformation begins during cooling. It is not a specific temperature since it changes with changing isothermal temperature for isothermal transformations and it varies with cooling rate in transformations occurred during continuous cooling.

The temperature at which austenite begins to form is usually defined as *Ac1* temperature and temperature at which austenite phase transformation completed from ferrite is represented as *Ac3* temperature.

Martensite start temperature (M_s), often defined as the temperature at which the transformation from austenite to martensite begins and martensite finish temperature (M_f), known as the temperature at which the transformation from austenite to martensite completed during quenching.

3.2.4.1. Evaluation and Calculation Procedure for Critical Temperatures

Beginning of austenite phase transformation, *Ac1*, was chosen as the temperature at which the derivative of $d\left((\frac{\Delta L}{L_0})/L_0\right)/dT$ first starts to deviate from linearity during heating from room temperature, where ΔL is change in length, L_0 is the initial length of sample and T is temperature. Transformation completion temperature for austenitic phase, *Ac3*, was determined at a point where the derivative of $d\left((\frac{\Delta L}{L_0})/L_0\right)/dT$ starting to bend back to the linearity from increasing the slope of dilatometric curve during heating. Briefly speaking, corresponding value in x-axis of local minima and maxima values of dilatometric curve represent phase transformation commencing and completion temperatures. Same austenitization segments were used in the all experiment sets as mentioned before. Thereby, both *Ac1* and *Ac3* temperatures can be easily calculated from any experiment set used in this study. CCT tests was selected for this purpose, so that *Ac1* and *Ac3* temperatures

were calculated one by one for each test in accordance and average values of these calculations were taken as the critical temperatures.

Critical points for bainitic phase transformation were determined with same procedure at determination of *Ac1* and *Ac3* temperatures.

On the other hand, transformation kinetics for martensite was also investigated in this study by using models explained in Chapter 2. Dilatometric curve obtained from sub-zero test was fitted on Koistinen-Marburger Equation (3). Consequently, critical temperatures for martensitic transformation can be theoretically calculated and results were given and discussed in following subdivision.

3.2.4.2. Results of Calculations for Critical Temperatures

Bainite start temperature was calculated and determined from CCT tests and results were given in Figure 24. *Ac1* temperature was calculated as 773 °C and *Ac3* temperature was calculated as 825 °C. Calculated *Ac1* and *Ac3* temperatures only applicable for 4.7 °C/s heating rate.

A section of the dilatometric curve (-135 to 300°C) obtained from the sub-zero test is given in Figure 38. As it can be seen from the figure, reverse S-shape form of dilatometric curve represents the martensitic phase transformation. Linear segments of dilatometric curve were extrapolated and indicated as dashed lines in Figure 38. These extrapolated straight lines are defined as the reference lines and they represent the regions for complete austenitic and martensitic phases. Once the reference lines were determined for austenitic and martensitic phases, lever rule was able to be applied on the dilatometric curve for theoretical determination of phase fractions as performed in TTT tests.

As a consequence, kinetic model of Koistinen-Marburger for martensitic phase transformation can be fitted onto experimental results as mentioned in Chapter 2, once dilatometric curve was converted into fractional transformation data with using this theoretical method. Measured retained austenite value for specimens of sub-zero test were less then %2 which is actually remains in undetectable range for XRD system used.

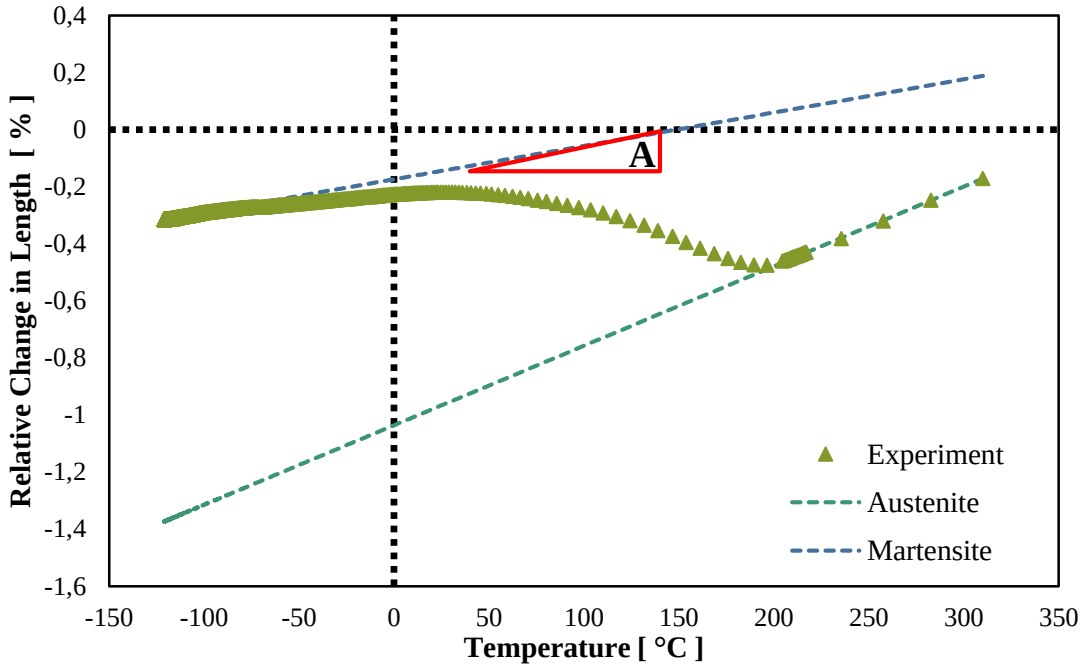

Figure 38: Sub-zero experiment No111 interval of (-)130 °C – (+)300 °C.

At the beginning of analysis procedure, Koistinen-Marburger model was tested in order to investigate kinetics of martensitic phase transformation. However, Koistinen-Marburger equation was not fitted well onto transformation data for a temperature range of 0-50 °C, including room temperature, as it can be seen in Figure 39. Therefore, Koistinen-Marburger equation has been modified by introducing an exponent *n* in order to fit the model well onto experiment results for the given temperature range with the following form in Equation (22):

$$P(T) = 1 - exp\left[-\Omega \cdot \left(M_s - T_f\right)^n\right] \quad ; \mathrm{T} \leq \mathrm{M_s} \tag{22}$$

where, *P(T)* is proportion of martensite transformed at a given temperature, M_s is the martensite start temperature, Ω is transformation rate constant, *n* is the exponent and T_f represents the temperature that is the proportion of martensite desired to be calculated. Equation (22) is equal to Koistinen-Marburger Equation (3) when $n = 1$.

The fittings of Koistinen-Marburger equation and modified one applied onto experimental result can be seen on Figure 39.

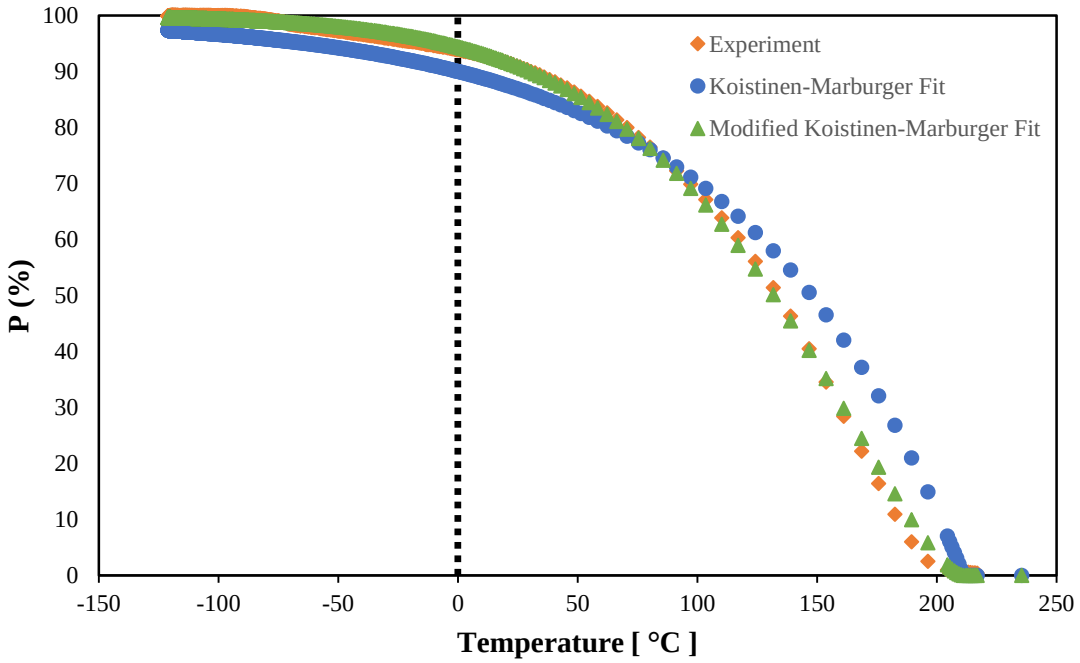

Figure 39: Phase transformed [%] vs temperature [°C] plot of sub-zero test and kinetic model fittings of Koistinen-Marburger and modified Koistinen-Marburger.

As it can be seen from the Figure 39, modified equation is in a good agreement with experimental data while former one diverges. Martensite start (0.7%) and martensite finish temperatures (99.9%) were calculated as 212±1 °C and -94±1 °C respectively from the modified equation. Material property Ω was calculated as 0.0109 for former Equation and 0.0098 for the modified one. In addition, exponent *n* for modified Equation is calculated as 1.455. Calculated values for material property Ω have similar values when compared with the literature which is 0.0107.

3.2.5. Determination of Thermal Expansion Coefficient

Definition of thermal expansion coefficient and related equations were discussed in Chapter 2. Calculation of thermal expansion coefficients of spheroidite, austenite and martensite were explained in this section.

Thermal expansion coefficients of spheroidite could be easily calculated from any experiment set used in this study since same austenitization segment was used in all sets of tests. Heating segment of tests is used for calculation of thermal expansion coefficient for spheroidized phase while cooling segment of tests is used for

calculation of thermal expansion coefficient for the austenitic phase. CCT tests were selected and evaluated for calculation of thermal expansion coefficients for austenitic and spheroidized phases.

A linear region on dilatometric curve that belongs to complete martensitic phase is needed for calculation of thermal expansion coefficient of martensite. Thus, sub-zero experiments were conducted, in which specimen first austenitized then cooled down -130 °C with 300 °C/s cooling rate.

3.2.5.1. Evaluation Procedure for Thermal Expansion Coefficient

Coefficient of thermal expansion might be basically defined as $\Delta\left(\left(\frac{\Delta L}{L_0}\right)/L_0\right)/\Delta T$ of dilatometric curve at the interval where $d\left(\left(\frac{\Delta L}{L_0}\right)/L_0\right)/dT$ remains constant. Specimens were heat-treated in preparation stage in order to begin the experiments with homogenous spheroidized microstructure. Therefore, linear expansion observed on dilatometric curve during heating to austenitization temperature could be used for calculation of thermal expansion coefficient for spheroidized phase (Figure 40).

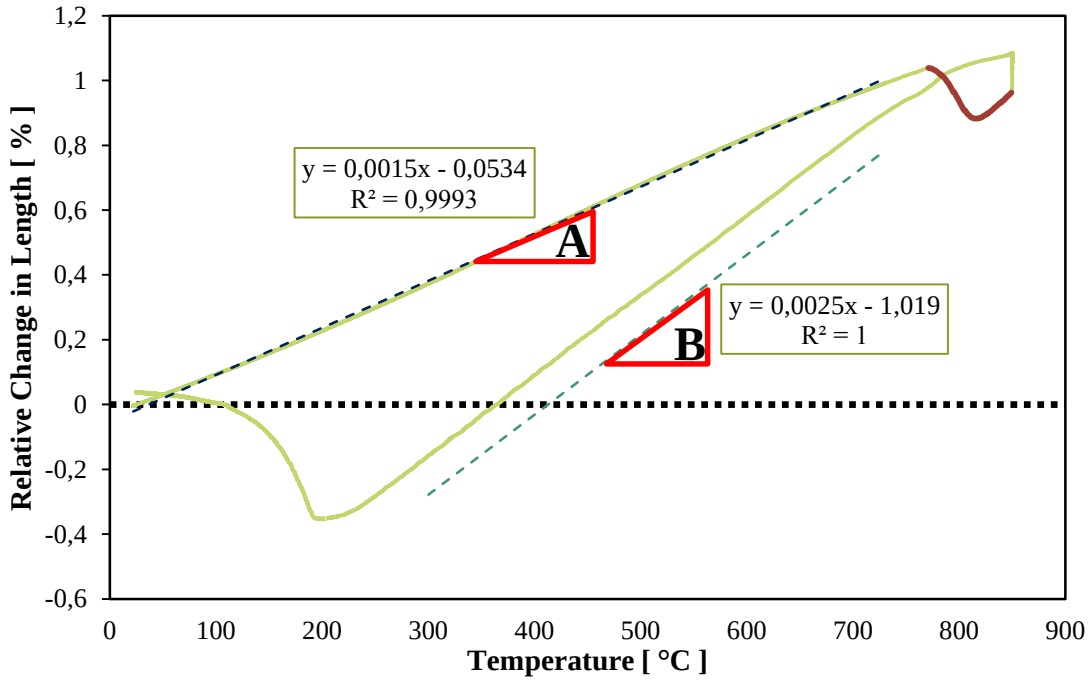

Figure 40: Relative change in length [%] vs. temperature [°C] representative plot for CCT tests. Slope of "A" refers to thermal expansion coefficient of spheroidite. Slope of "B" refers to thermal expansion coefficient of austenite.

Thermal expansion of austenite can be calculated with same evaluation procedure as thermal expansion of spheroidite. However, cooling segment of the experiments were used for this purpose since after the austenitization of specimen, behavior of the material changes in terms of contraction of austenitic phase when compared with the behavior of the material before the austenitization.

Thermal expansion coefficient of martensite was calculated from the experimental data of sub-zero tests. Martensitic phase formed on the specimens were confirmed via XRD measurements and according to XRD results, the amount of retained austenite available in the specimens were less than 2% as mentioned before.

Graphical representation of $\Delta\left(\left(\frac{\Delta L}{L_0}\right)/L_0\right)/\Delta T$ was given at Figure 38 for a temperature range -135°C to 300°C on relative change in length versus temperature plot of a sub-zero test. Slope of "A" in Figure 38 can be commented as the thermal expansion coefficient of martensitic phase.

3.2.5.2. Results for Calculations of Thermal Expansion Coefficient

Total 15 numbers of experiments were evaluated for determination of thermal expansion coefficient of austenite and spheroidite. The average values of these calculations were taken as thermal expansion coefficient of austenite and spheroidite, which are 22.2 ± 1.23 [10^{-6}/K] and 15.1 ± 0.22 [10^{-6}/K] respectively. Coefficient of thermal expansion of austenite found in literature [12] is 23.8 [10^{-6}/K] and it can be said that calculated results is in good agreement with the literature.

Total 2 numbers of experiments evaluated for determination of thermal expansion coefficient of martensitic phase. Average value of these calculations is 11.6 [10^{-6}/K] and the value is accepted as the thermal expansion coefficient of martensite. This value also corresponding to the value in the literature [12] 10.9 [10^{-6}/K].

3.2.6. Determination of Densities for Spheroidite, Austenite and Martensite

Densities of spheroidite, austenite and martensite phases were determined as a function of temperature by combining Buoyancy method and dilatometry. A precision balance with a draftshield was used in order to determine densities by

Buoyancy method. Dilatometric curves of CCT tests were used at dilatometry side of density calculations. Densities were also computed via JMatPro® in order to compare with the experimental results.

3.2.6.1. Evaluation Procedure for Densities of Phases

Firstly, martensitic samples and spheroidized samples were measured one by one with precision balance in a controlled environment at room temperature. Water was selected as a gauging fluid for buoyancy method. Temperature of the environment was recorded and effect of temperature on density of the water was taken into account during calculation of the density values. Unfortunately, The Buoyancy method is not applicable for density measurements at elevated temperatures since water was selected as a Buoyancy fluid and it boils at these elevated temperatures. Therefore, as mentioned before, a combination of Buoyancy method and dilatometry was used for determination of density values for each phase.

The average density value measured by Buoyancy method was accepted as the density value for spheroidite phase at reference temperature (25°C). Since, the density value was measured and determined with Buoyancy method and thermal dilation of related phase was obtained from dilatometry, Equation (14) could be used for calculating density value for spheroidite phase at elevated temperatures.

The Buoyancy method is not applicable for density measurements at elevated temperatures, where austenite is present in the microstructure. Furthermore, it is very difficult to obtain completely austenitic specimen at room temperature. Therefore, Buoyancy method could not be used for measuring the density value of austenitic specimen. In order to calculate the density of austenite, transformation strain and density values of spheroidite were used in Equation (12).

Transformation strain of spheroidite to austenite had been calculated at room temperature from the dilatometric tests. By the way, detailed information about calculation procedure used for transformation strains is given in following subdivision.

In consequence, density of austenitic phase was calculated with Equation (23), which has a re-arranged form of Equation (12):

$$\rho_A = \frac{\rho_S}{(\varepsilon_{S\to A}^{tr} + 1)^3} \tag{23}$$

where, $\varepsilon_{S\to A}^{tr}$ represents the transformation strain for spheroidite to austenite phase transformation at room temperature, ρ_A is density of austenite and ρ_S is density of spheroidite at room temperature.

Density of martensitic phase was calculated from Equation (13). The amount of retained austenite present in each martensitic specimen was determined by XRD. Only austenitic and martensitic phases were assumed to be present in the microstructure of the martensitic samples, therefore Equation (13) takes the following form (24):

$$\rho_{tot} = \rho_M \cdot P_M + \rho_A \cdot P_A \tag{24}$$

where, ρ_{tot} is the total density of martensitic sample, ρ_M and ρ_A are densities of martensitic and austenitic phases respectively and P_M and P_A are phase fractions of martensitic and austenitic phases respectively. Density of martensite was obtained by solving Equation (24) for two or more martensitic samples.

3.2.6.2. Results of Density Calculations

Results of density calculations for spheroidite, austenite and martensite are given in Figure 41 as a function of temperature. Results of JMatPro® calculations and density values found in literature [12, 13] were also indicated on the same figure for comparison.

As it can be seen on Figure 41, experimental results, computational results and literature data are in good agreement as expected. Detailed information about evaluation procedure used in JMatPro® calculations are given in Chapter 4.

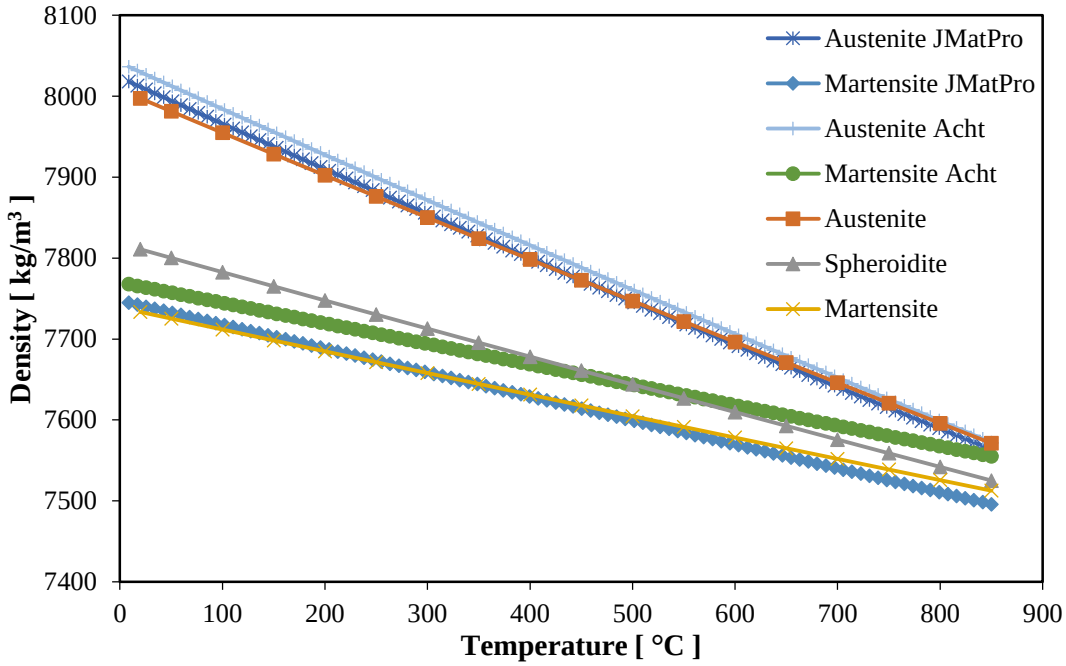

Figure 41: Densities of Spheroidite, Austenite and Martensite with respect to temperature. JMatPro® and literature [12, 13] values for densities are also shown.

3.2.7. Determination of Thermal and Transformation Strains

Thermal strain can be defined as strain developed as a result of temperature change and transformation strain can be defined as strain resulting from change in crystallographic structure during phase transformation. Detailed information about thermal strains and transformation strains were given in Chapter 2.

3.2.7.1. Evaluation Procedure for Thermal and Transformation Strains

Thermal strains and transformation strains were calculated by evaluating the dilatometric curves. Dilatometric curves obtained in CCT Tests were used for this purpose. First order linear regression lines were fitted onto regions where $d\left(\left(\frac{\Delta L}{L_0}\right)/L_0\right)/dT$ remains constant one by one for each related phase. The first order linear regression lines for martensite, spheroidite and austenite phases are shown on Figure 42. The linear relation between temperature and thermal strain was already explained in Chapter 2. Thus, thermal strains can be calculated for any phase at any

given temperature, when both transformation strain and thermal expansion coefficient values for related phase are known.

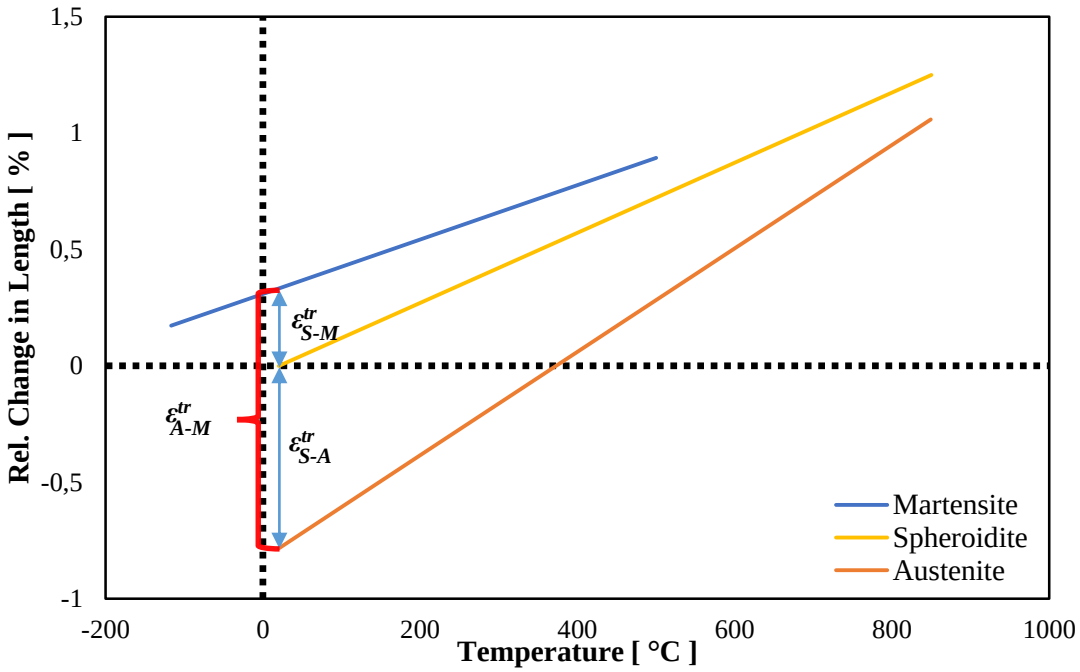

Figure 42: Thermal strains of martensite, spheroidite and austenite phases for steel 100Cr6. Transformation strains $\varepsilon^{tr}_{A\rightarrow M}$, $\varepsilon^{tr}_{S\rightarrow A}$ and $\varepsilon^{tr}_{S\rightarrow M}$ also indicated on the figure.

Differences in thermal strains between parent and product phases at room temperature were also indicated on Figure 42, which give the transformation strain for related phase transformation. The reference phase was taken as spheroidite during calculation for transformation strains since all samples were spheroidized and spheroidite was the initial phase for dilatometric tests.

Transformation strains might also be calculated from density measurements with the relation (12), when the relative amount of phase constituents are known. Transformation strain of martensite was calculated in such a way from the density values using Equation (12).

3.2.7.2. Results of Calculations for Thermal and Transformation Strains

Thermal strains calculated at temperatures 0°C and 1000 °C were given in Table 12. Transformation strains calculated at temperatures 20 °C and 850 °C were also given

in Table 13. As it can be seen from the results, experimentally determined transformation and thermal strain values are similar to values found in the literature [13].

Table 12: Thermal Strains calculated at 0 °C and 1000 °C.

Temperature:	**0 °C**	**1000 °C**
Thermal Strain for Spheroidite [-], ε_S^{th}	-3.01*10^{-4}	1.48*10^{-2}
Thermal Strain for Austenite [-], ε_A^{th}	-8.28*10^{-3}	1.39*10^{-2}
Thermal Strain for Martensite [-], ε_M^{th}	3.09*10^{-3}	1.48*10^{-2}

Table 13: Transformation Strains calculated at 20 °C and 850 °C.

Temperature:	**20 °C**	**850 °C**
Spheroidite to Austenite [%], $\varepsilon_{S\to A}^{tr}$	-7.83*10^{-1}	-1.91*10^{-1}
Austenite to Martensite [%], $\varepsilon_{A\to M}^{tr}$	1.12*10^{0}	2.44*10^{-1}
Spheroidite to Martensite [%], $\varepsilon_{S\to M}^{tr}$	3.32*10^{-1}	5.31*10^{-2}

3.2.8. Determination of Mechanical Properties of Austenite, Martensite and Bainite Phases

Flow curves for austenite, martensite and bainite phases were determined as a function of temperature using deformation dilatometry. Ramberg-Osgood Model (25) has been used in order to introduce stress-strain curves as a function of temperature into the heat treatment simulation code of SYSWELD®.

$$\sigma_{true} = K_{RO}\left(\varepsilon_i^{pl}\right)^{n_{RO}} \tag{25}$$

where, σ_{true} is the true stress, ε_i^{pl} is the plastic strain, K_{RO} and n_{RO} values represent material parameter and strain hardening exponent of Ramberg-Osgood model respectively.

Since the deformation measurement system (LVDT) of the deformation dilatometer measures total strain one must calculate ε_i^{pl} from total strain and elastic modulus before fitting the parameters to the model. Assuming an additive decomposition, total strain can be described as the sum of elastic (ε_i^{el}) and plastic (ε_i^{pl}) strains as in Equation (26). Moreover, thermal, transformation and transformation plasticity strains are not involved in the total strain given in Equation (26) since the dilatometry tests were conducted isothermally and they were all finished before the initialization of phase transformation.

$$\varepsilon_i^{tot} = \varepsilon_i^{el} + \varepsilon_i^{pl} \tag{26}$$

Equation (25) can be rearranged as the following form (27) by using Equation (26):

$$\varepsilon_i^{tot} = \frac{\sigma_{true}}{E_i} + K_{RO}\left[\frac{\sigma_{true}}{E_i}\right]^{n_{RO}} \tag{27}$$

where, ε_i^{tot} represents total strain measured by dilatometer for sample *i*, σ_{true} is the true stress, E_i is the elastic modulus of sample *i*, K_{RO} and n_{RO} values represent material parameter and strain hardening exponent of Ramberg-Osgood model respectively.

3.2.8.1. Evaluation Procedure for Mechanical Tests

True strain-true stress plots were obtained from deformation dilatometry tests and they were fitted onto Ramberg-Osgood model (25) for each phase at a given temperature.

At first, true plastic strain component of the dilatometric test was calculated by Equation (26) since the values for total strain and elastic strain components were both known. Total strain was obtained from dilatometric tests and elastic strain component was calculated from dividing total stress to elastic modulus of related phase at a given temperature. Modulus of elasticity was obtained from JMatPro® calculations since stiffness of the dilatometer was not adequate for determination of elastic modulus for steels. After calculating plastic strain component of the dilatometric test, Ramberg-Osgood model parameters K_{RO} and n_{RO} were fitted

iteratively by reducing total RMS error between plastic strain component of the test and calculated value from the model. A representative example given in Figure 43 shows a good agreement established between measured data and the fitting.

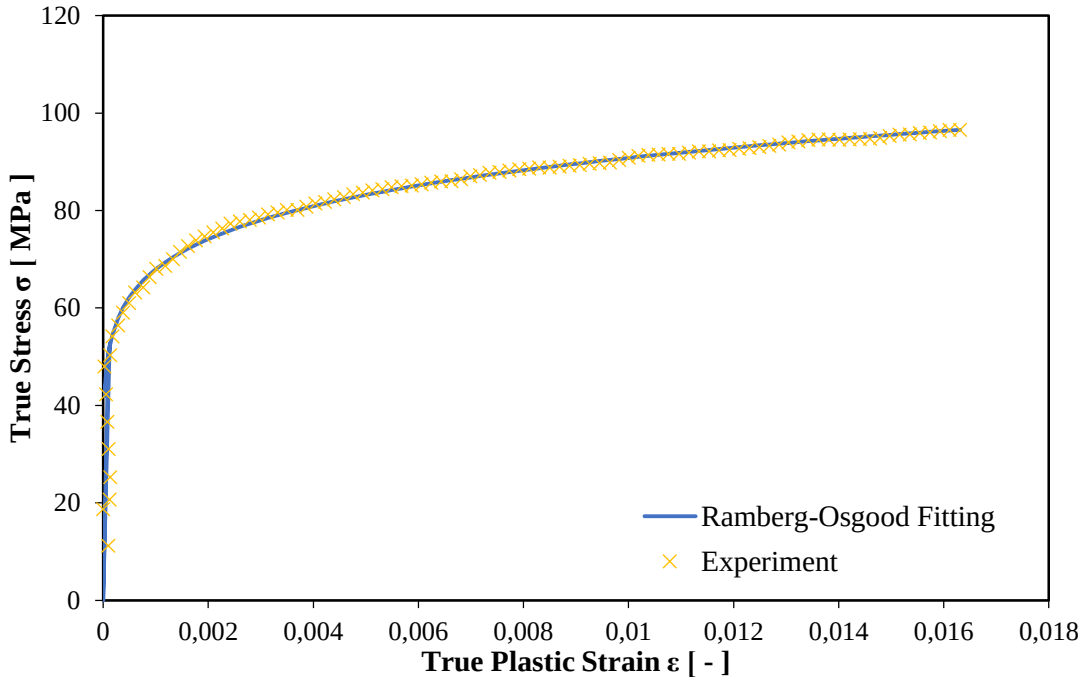

Figure 43: Ramberg-Osgood Model fitting for mechanical test of austenite at 850°C.

After determining the Ramberg-Osgood parameters for each phase and for each temperature, the temperature dependency of the parameters K_{RO} and n_{RO} were determined by fitting the calculated values onto linear or polynomial regression lines with a suitable order. This procedure was applied for all phases and results can be found in following subdivision.

3.2.8.2. Results of Mechanical Tests

Calculation results and fitted regression lines for material parameter K_{RO} were given in Figure 44, Figure 46 and Figure 48 for austenite, bainite and martensite phases respectively. Furthermore, temperature dependency of hardening exponent n_{RO} and regression lines fitted were given in Figure 45, Figure 47 and Figure 49 for austenitic, bainitic and martensitic phases respectively.

In mechanical test of meta-stable austenite, flow-curves were obtained for a temperature range between 300°C to 850°C since martensite start temperature was calculated as 212±1 °C and below 300°C, austenite might be transformed into martensite. In order to describe mechanical properties of austenite below 300°C, fittings of calculated K_{RO} and n_{RO} values for a temperature range 300°C-850°C were extrapolated to room temperature.

In mechanical tests of martensitic and bainitic phases it was aimed to reach at least %1 strain at elevated temperatures, however dilatometer was not able to reach required stress level for %1 strain for both martensitic and bainitic phases even at the elevated temperatures. Furthermore, martensitic and bainitic phases could not have plastically deformed below 300 °C since the force needed for plastic deformation of martensitic and bainitic phases is much higher than the force that is able to be applied by dilatometer. Therefore, experiments conducted below 300 °C temperature was not taken into consideration for determination of mechanical properties of martensitic and bainitic phases.

In consequence, fittings of calculated K_{RO} and n_{RO} values for a temperature range above 300°C were extrapolated to room temperature in order to investigate mechanical properties of martensitic and bainitic phases. It must be noted that the results given in this section only applicable up to %1 strain for martensitic and bainitic phases.

Dashed lines shown on the figures are referred as the extrapolated regions due to above mentioned problems in order to describe and investigate the tendency of K_{RO} and n_{RO}.

As it can be seen from the Figure 44, Figure 46 and Figure 48, calculated values for material parameter K_{RO} show a linear relationship with temperature. On the other hand, hardening exponent n_{RO} values do not have clear relationship with temperature as it can be seen in Figure 45, Figure 47 and Figure 49.

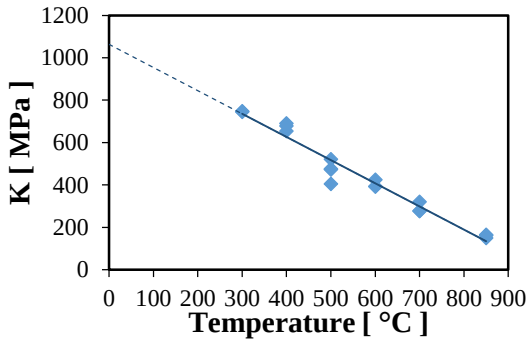

Figure 44: Results of calculations for mechanical tests of austenite and regression line fitted for material parameter K_{RO} w.r.t. temperature.

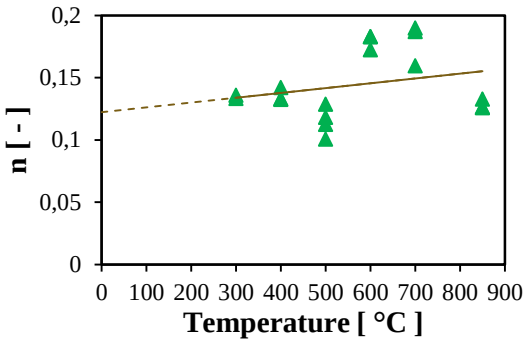

Figure 45: Temperature dependency of hardening exponent n_{RO} and regression line fitted onto calculated values of mechanical tests of austenite.

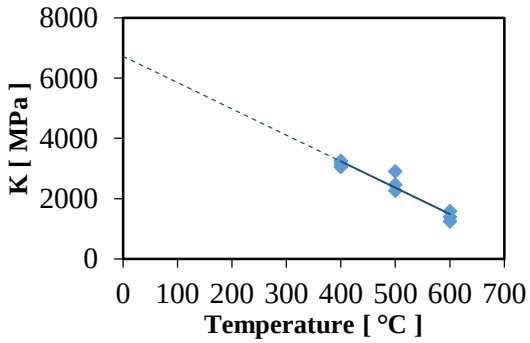

Figure 46: Results of calculations for mechanical tests of bainite and regression line fitted for material parameter K_{RO} w.r.t. temperature.

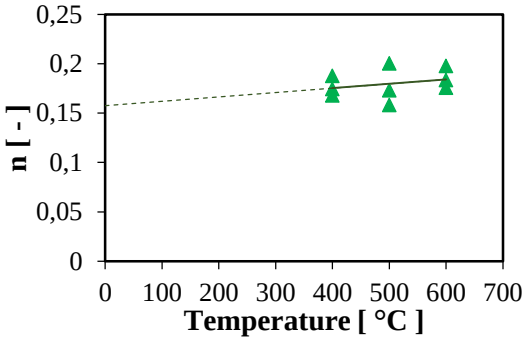

Figure 47: Temperature dependency of hardening exponent n_{RO} and regression line fitted onto calculated values of mechanical tests of bainite.

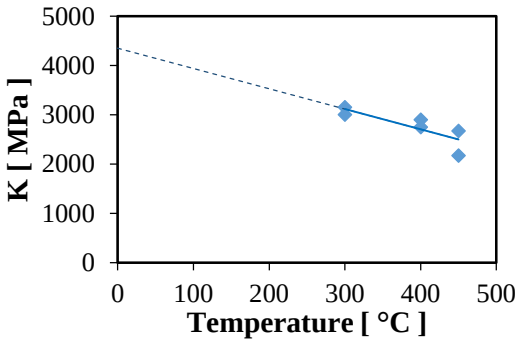

Figure 48: Results of calculations for mechanical tests of martensite and regression line fitted for material parameter K_{RO} w.r.t. temperature.

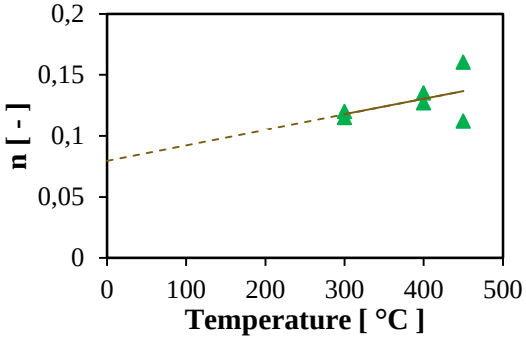

Figure 49: Temperature dependency of hardening exponent n_{RO} and regression line fitted onto calculated values of mechanical tests of martensite.

Flow curves calculated from Ramberg-Osgood model with K_{RO} and n_{RO} fittings for austenitic, bainitic and martensitic phases were given as a function of temperature in Figure 50, Figure 51 and Figure 52 respectively. Flow curves found in the literature [12] are also indicated on the same figures in order to make a comparison between them.

Calculated flow curves for meta-stable austenite are in good agreement with flow curves available in the literature [12] as it can be seen in Figure 50. Calculated flow curve for martensite also compared in Figure 52 with flow curve found in the same literature. Flow curves for martensite are converging quite well at elevated temperatures, while they are diverging with decreasing temperature.

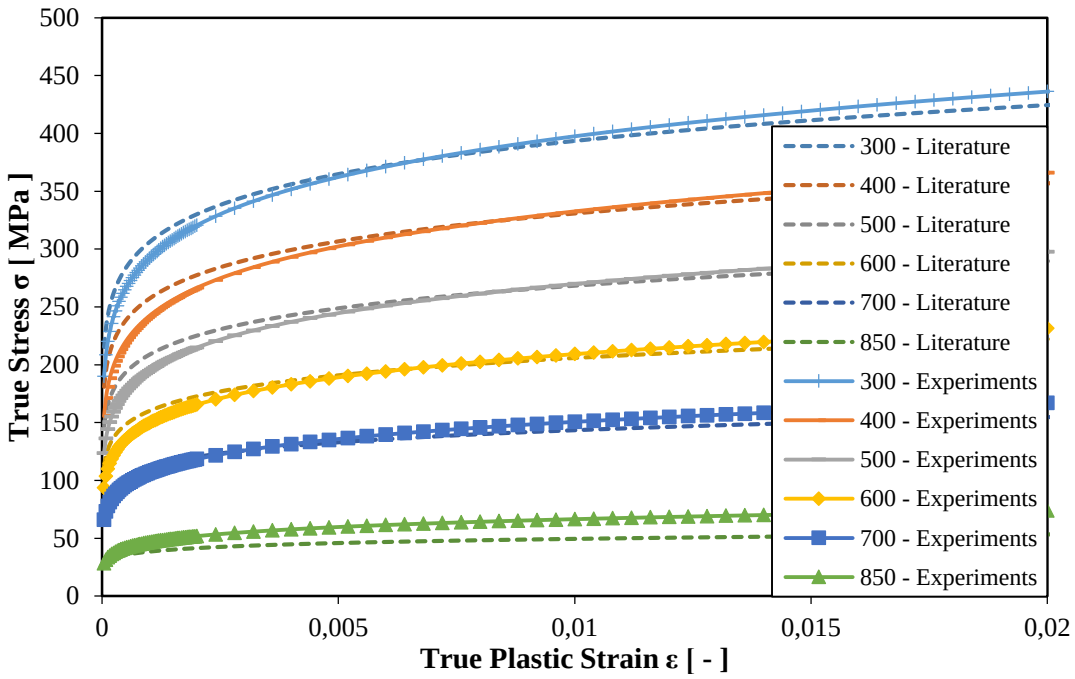

Figure 50: True stress vs. true plastic strain plots for meta-stable austenite for a temperature range 300°C-850°C. Flow curves from the literature [12] are also indicated.

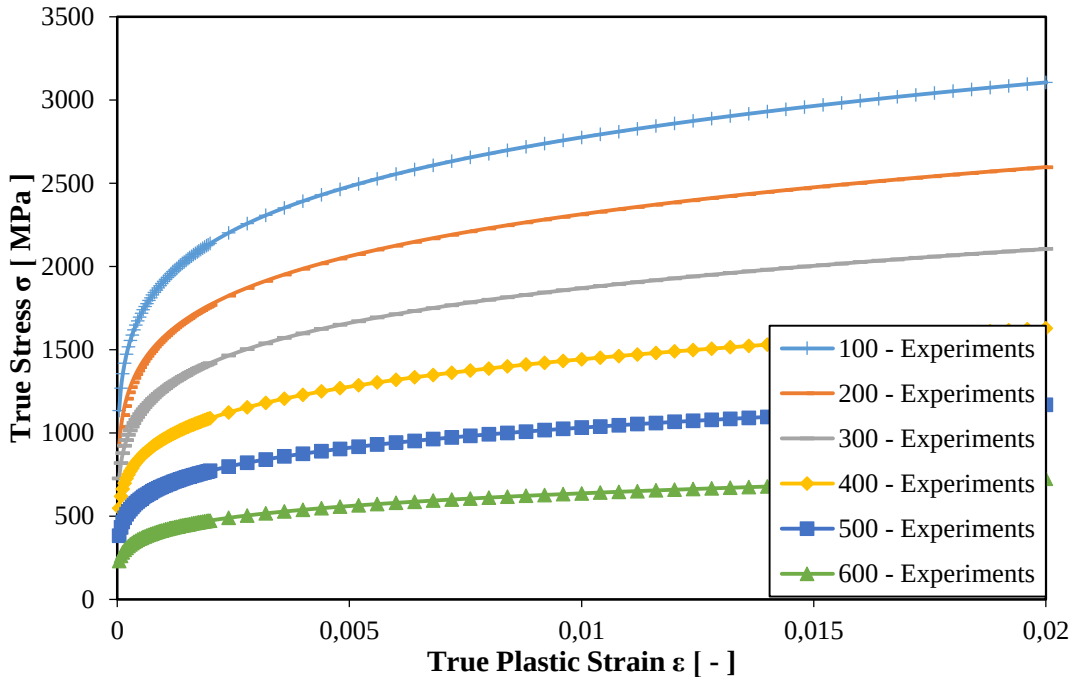

Figure 51: True stress vs. true plastic strain plots for bainitic phase for a temperature range 100°C-600°C.

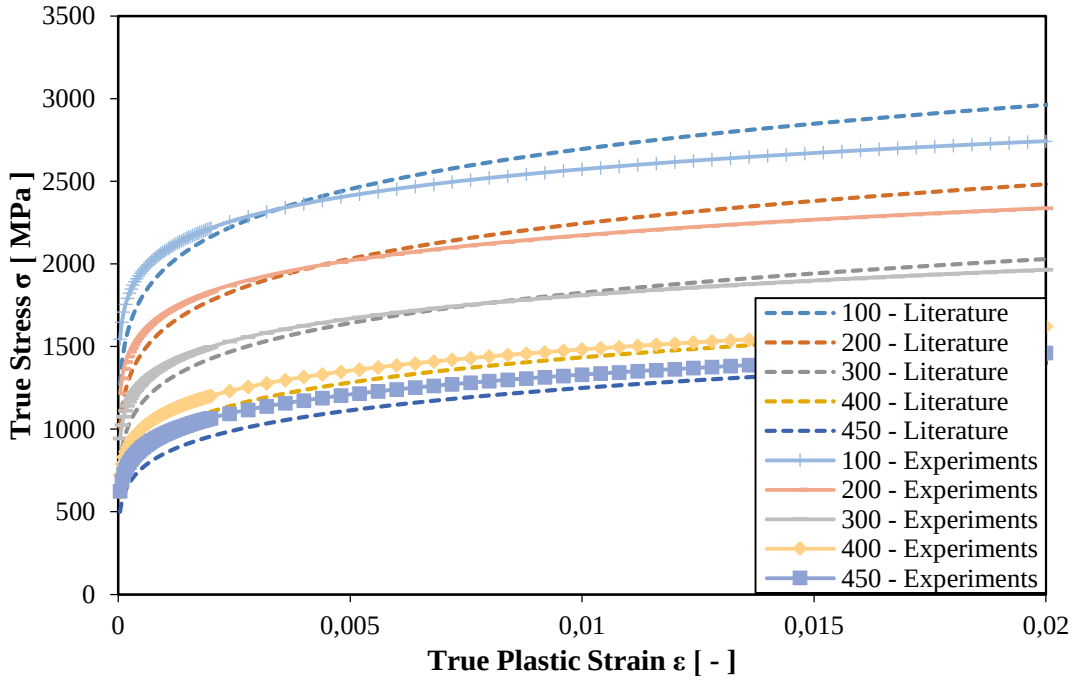

Figure 52: True stress vs. true plastic strain plots for martensitic phase for a temperature range 100°C-450°C. Flow curves found in literature [12] are also indicated.

Yield strengths, σ_y, of austenitic, bainitic and martensitic phases were calculated in accordance with Ramberg-Osgood equation (25) at 0.005% proof stress (28):

$$\sigma_y = K_{RO}(0.00005)^{n_{RO}} \quad (28)$$

Results were given in Figure 53, Figure 54 and Figure 55. Yield strengths found in the literature and values computed via JMatPro® are also indicated on the same figures. Furthermore, both linear and second order polynomial fittings were tested and they are indicated on the figures. However, linear fittings were taken into consideration since they have reasonable values when compared with second order polynomial fittings in terms of their extrapolated values at room temperature.

As it can be seen from the figures, experimentally determined yield strengths for meta-stable austenite and martensite are in good agreement with the literature. On the other side, computed yield strengths via JMatPro® are showing different tendency from both experimental and literature values since it does not include fracture mechanisms in computations.

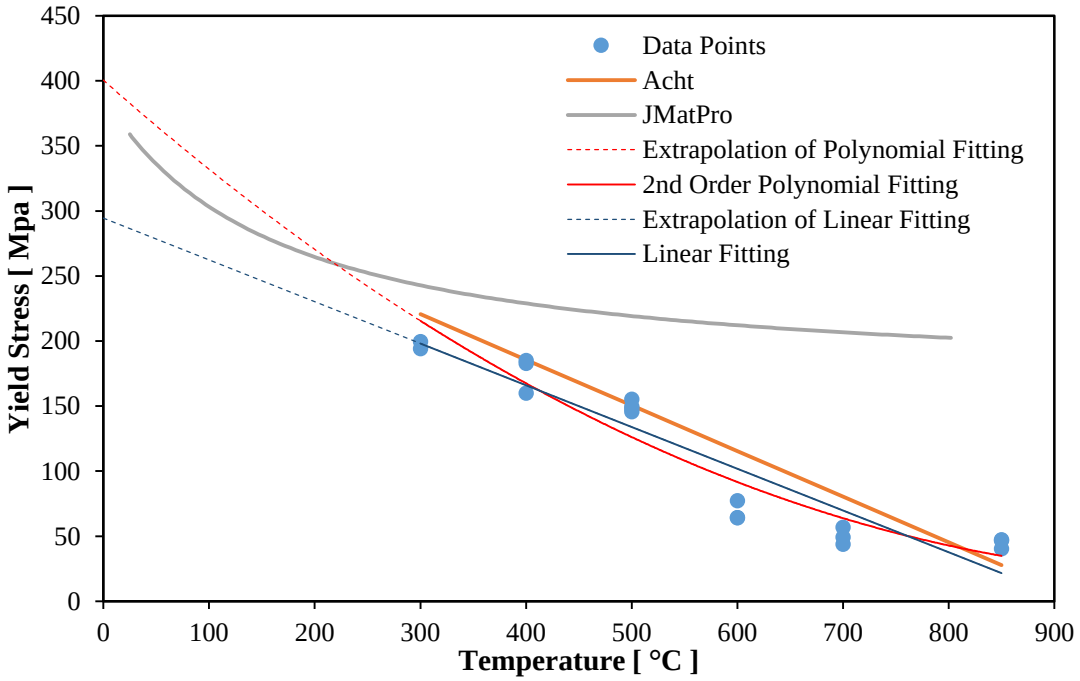

Figure 53: Yield strengths of meta-stable austenite as a function of temperature. Yield strengths found in literature and computed via JMatPro® are also indicated.

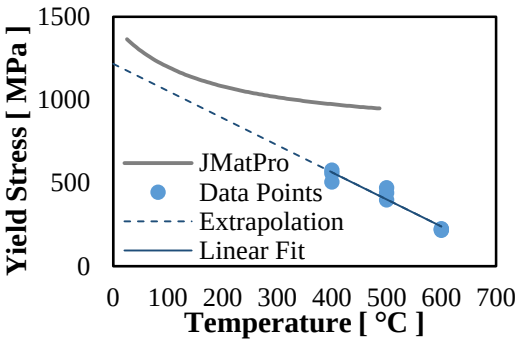

Figure 54: Yield strength of bainitic phase with respect to temperature.

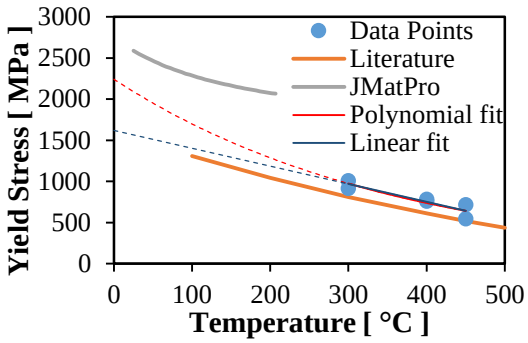

Figure 55: Yield strength of martensitic phase as a function of temperature.

3.2.9. Determination of the Effect of Stress on Phase Transformations

In this part of the study, the effect of uniaxial compressive stresses on bainitic and martensitic phase transformations was aimed to be investigated with stressed dilatometry. As it can be seen from Equation (4), transformation plasticity is characterized with transformation plasticity parameter (K^{tp}) which was calculated with an evaluation procedure given in following section.

3.2.9.1. Evaluation Procedure for TRIP Tests

Difference between longitudinal strains of stress-free sample and stressed one for the related transformation gives the transformation plasticity. The relationship was defined in Equation (29) for a given temperature:

$$\varepsilon^{tp}(P) = \varepsilon(\sigma, P) - \varepsilon(\sigma = 0, P) \tag{29}$$

where, P is the fraction of phase and transformation of related phase is finished when P = 1, which means the transformation plasticity has its maximum value and often called as extent of transformation plasticity.

In order to investigate the effect of stress on bainitic phase transformation, applied stress and temperature were held constant during the test until phase transformation was completed. Therefore, extent of transformation was taken into account in calculations since the phase transformation was completed. Difference between longitudinal strains of stress-free sample and stressed ones for the bainitic transformation can be seen in Figure 56. Relative change in length versus time

curves were obtained from stressed dilatometry tests. The raw data obtained from the tests fitted onto JMA equation as described in TTT tests for theoretical calculation of end points of bainitic phase transformations at different stress levels.

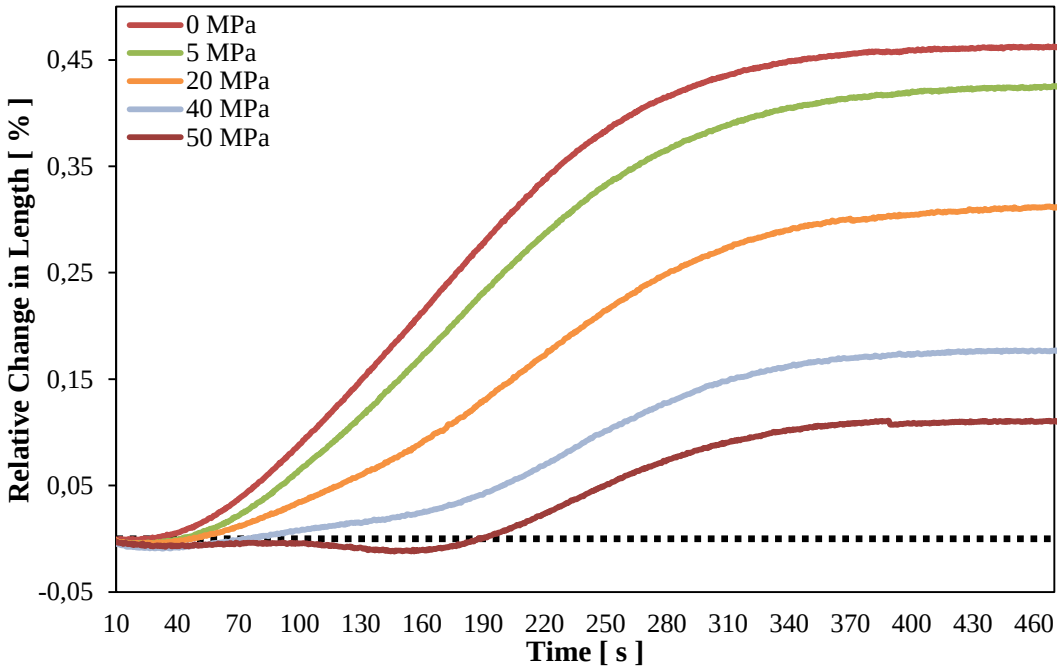

Figure 56: The effect of stress on bainitic phase transformation.

In order to investigate the effect of stress on martensitic phase transformation, various uniaxial stresses were applied to the specimens at 350°C and held constant during cooling to the room temperature with 10°C/s cooling rate. It is expected that martensitic phase transformation could not be completed at room temperature since M_f calculated as -94±1 °C. Progress of transformation plasticity function *f(z)* must be introduced for calculation of transformation strain as in the Equation (4) when phase transformation is not completed. However, progress of transformation plasticity function would be subtracted from the equation if strain at the end of phase transformation is known. Therefore, modified Koistinen-Marburger equation (22) was fitted onto dilatometric curves then the curves were extrapolated according to their modified Koistinen-Marburger fittings until completion of their transformations (99.9%). Longitudinal strains at the extrapolated end for each stress levels were

obtained from these fittings. In order to fit the modified equation phase fractions must be obtained by applying lever rule to the dilatometric curve as discussed before. Thus, thermal strains for austenitic and martensitic phases were calculated for each test in order to apply the lever rule. Thermal strain of austenite was calculated from the test. However, thermal strain for martensitic phase was not known since martensitic transformation was not completed. In order to determine thermal strain of martensite for each test, retained austenite values of specimens measured and iteratively matched for giving same results with lever rule. The amount of retained austenite present in the specimens was measured via XRD. In consequence, dilatometric curves obtained from the TRIP tests and extrapolated curves (dashed lines) can be seen in Figure 57.

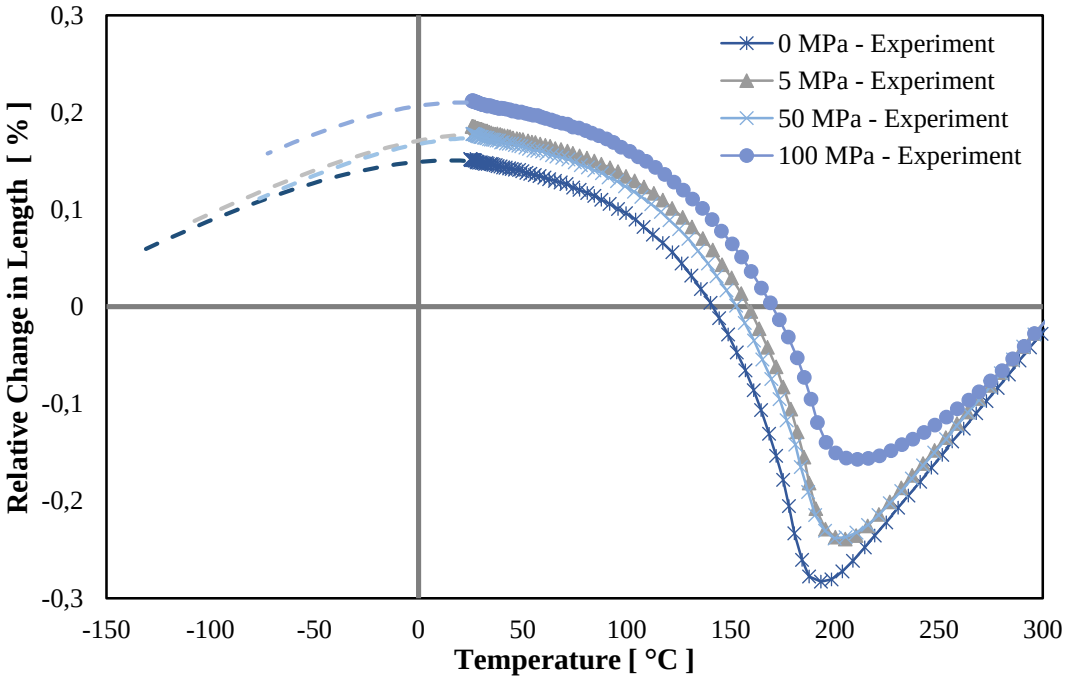

Figure 57: Modified Koistinen-Marburger fitted dilatometric curves of TRIP tests of martensitic transformation. Extrapolated regions are indicated as dashed lines.

3.2.9.2. Results of TRIP Tests

Transformation plasticity strain versus applied stresses for both bainitic and martensitic phase transformations are given in Figure 58 and Figure 59 respectively.

It must be noted that, TRIP tests were performed at temperature of 350 °C under various uniaxial compression stresses as explained before. Therefore, results are only applicable for 350 °C and uniaxial compression stresses within a range 0 MPa to 100 MPa.

As it can be seen from Figure 58 and Figure 59 , transformation plasticity strains (ε^{tp}) have linear relationship with the applied stresses for both bainitic and martensitic phase transformations. The slope of the straight lines indicated on the figures can be commented as transformation plasticity parameter (K^{tp}) as stated in Equation (4). The transformation plasticity parameter was calculated as $1.06*10^{-5}$ MPa^{-1} and $6.82*10^{-5}$ MPa^{-1} for martensitic and bainitic phase transformations respectively.

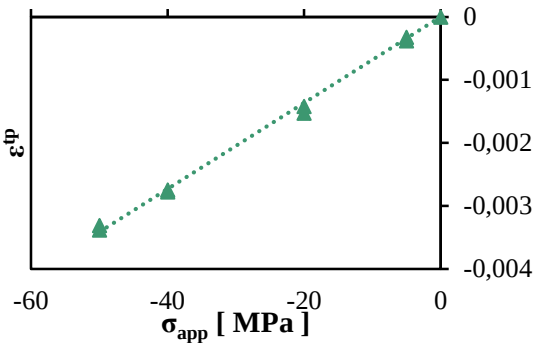

Figure 58: Transformation plasticity strain vs. applied load plot for bainitic phase transformation.

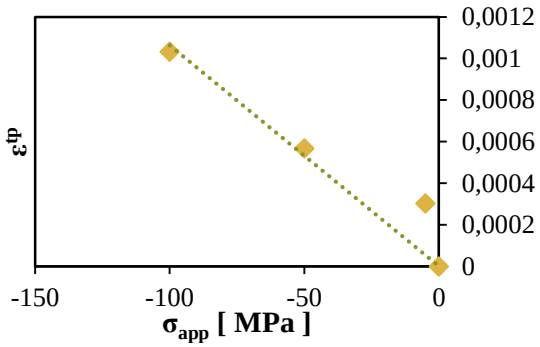

Figure 59: Transformation plasticity strain vs. applied load plot for martensitic phase transformation.

In addition to experimental determination of K^{tp}, there are models available for the calculation of K^{tp} in the literature [29, 55, 57, 58]. Greenwood and Johnson were published their model (30) in 1965. After the work published by Greenwood and Johnson, Abrassart (31), Leblond (32) and Dalgic (33) were developed models for the calculation of K^{tp} which are mainly based on the former model of Greenwood and Johnson. The models are given as follows:

$$K^{tp} = \frac{5}{6} \cdot \frac{1}{\sigma_y^a} \cdot \frac{\Delta V}{V} \tag{30}$$

$$K^{tp} = \frac{1}{4} \cdot \frac{1}{\sigma_y^a} \cdot \frac{\Delta V}{V} \tag{31}$$

$$K^{tp} = \frac{2}{3} \cdot \frac{1}{\sigma_y^a} \cdot \frac{\Delta V}{V} \tag{32}$$

$$K^{tp} = c \cdot \frac{1}{\sigma_y^a} \cdot \frac{\Delta V}{V} \tag{33}$$

where, σ_y^a is the yield strength of austenite at a given temperature, $\frac{\Delta V}{V}$ is the volume change during phase transformation and c is temperature dependent factor for the model developed by Dalgic and it may take a value between 0.25 and 0.83. As it can be seen from the equations, the models mainly related with yield strength of austenite and change in volume due to phase transformation.

Models were tested and the results for martensitic phase transformation are given in Figure 60. In order to calculate K^{tp} with these models, volume change and yield strength of austenite must be known as a function of temperature. The change in volume was obtained from the dilatometric tests performed for TRIP tests of martensitic phase. Change in volume could not be measured by the dilatometer since dilatometer has only one extensometer which is used for measuring longitudinal strains of the specimen. Therefore, change in volume was calculated by longitudinal strains obtained from the dilatometric tests with following relation (34):

$$\frac{\Delta V}{V} = 3\frac{\Delta l}{l} \tag{34}$$

Yield strength of austenite had been already determined as a function of temperature in mechanical tests of meta-stable austenite. After calculation of K^{tp} as a function of temperature with the theoretical models, integral sum of the curves given in Figure 60 were taken and calculated values determined as K^{tp} value for a temperature range between 0°C to 210°C. However, the integral sum, which was calculated from the model developed by Leblond, was determined as K^{tp} value for martensitic transformation since SYSWELD® is using Leblond model for calculation of transformation plasticity constant.

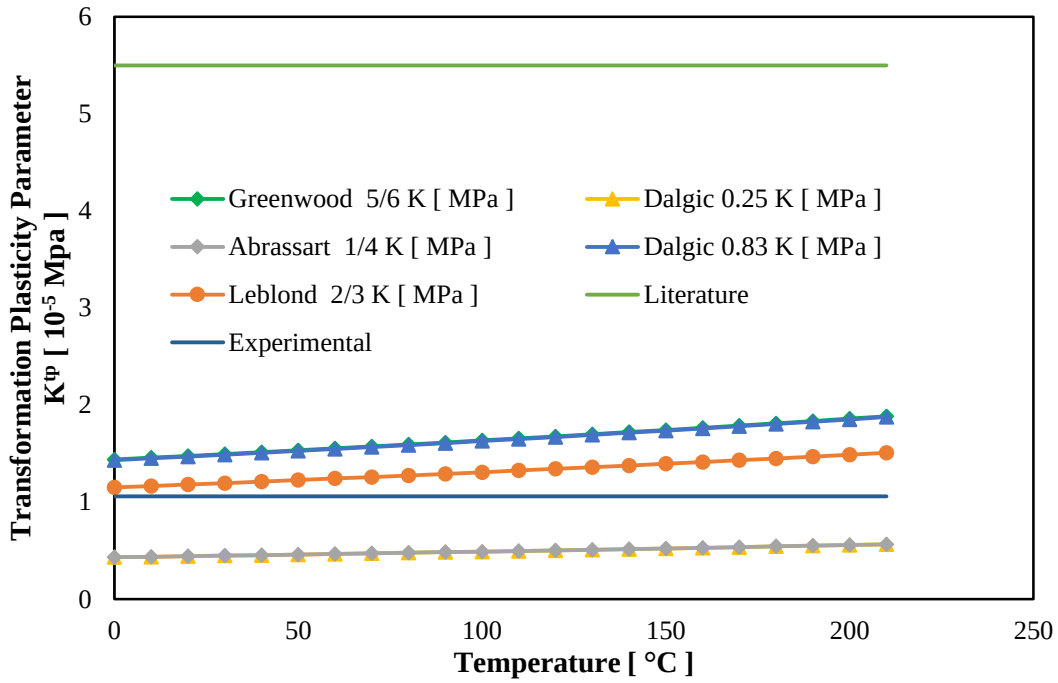

Figure 60: Theoretically calculated transformation plasticity parameter vs. temperature plot for martensitic phase transformation.

Experimentally determined and theoretically calculated values of transformation plasticity constants for both bainitic and martensitic phases are given in Table 14. Values found in the literature [58] for K^{tp} are also given in the same table. As it can be seen from the Table 14, results for bainitic transformation are good agreement while results for martensitic transformation are not. The difference observed in the results for martensitic transformation could be due to difference in calculation procedures or in experimental conditions.

Table 14: Results for calculations of transformation plasticity constants of bainitic and martensitic phases at 350 °C.

Phase	**Experimental**	**Theoretical**	**Literature**
Bainite [10^{-5} MPa^{-1}]	6.82	5.08	7,24
Martensite [10^{-5} MPa^{-1}]	1.06	1.32	5,42

Experimentally and theoretically determined K^{tp} values were tested in a through-hardening simulation of a conical ring and results are given in Chapter 5.

CHAPTER 4

COMPUTATIONAL DETERMINATION OF MATERIAL PROPERTIES

4.1. General

Determination of material properties in order to use in through-hardening simulations was aimed in this study. In addition to experimentally determined material properties in the previous chapter, several properties are also needed for through-hardening simulations such as specific heat, thermal conductivity, enthalpy, Young's modulus and Poisson's ratio. The effect of these properties on through-hardening simulations is negligible as experienced in preliminary study. However, simulations cannot be initialized without these material properties. Therefore, density, specific heat, thermal conductivity, enthalpy, Young's modulus and Poisson's ratio values for steel 100Cr6 were intended to be calculated with computational methods.

4.2. Theory

Computational techniques for material property determination is undergoing a rapid development. Phase constitution as a function of temperature and chemical composition might be calculated with traditional thermodynamics. However, there exist a separation of material properties and the thermodynamic properties. There is currently available software namely, JMatPro®, which enhances the thermodynamic calculations to make quantitative calculations possible with physical and microstructural parameters and the material properties [15]. The quantitative calculation for the requested material property is obtained via thermodynamic calculations by taking into account of theoretical material models and property databases. In multicomponent systems, material properties needed such as Young's

modulus, Poisson's ratio and densities are calculated by pair wise mixture models for each phase.

Material properties are well calculated with using computational techniques, there are a lot of work published that JMatPro® had been used for calculation of material properties and works also consist of verification of computational results with corresponding experiments [15-20, 66-68]. Calculation procedure for material properties of any steel can be summarized in four steps (Figure 61).

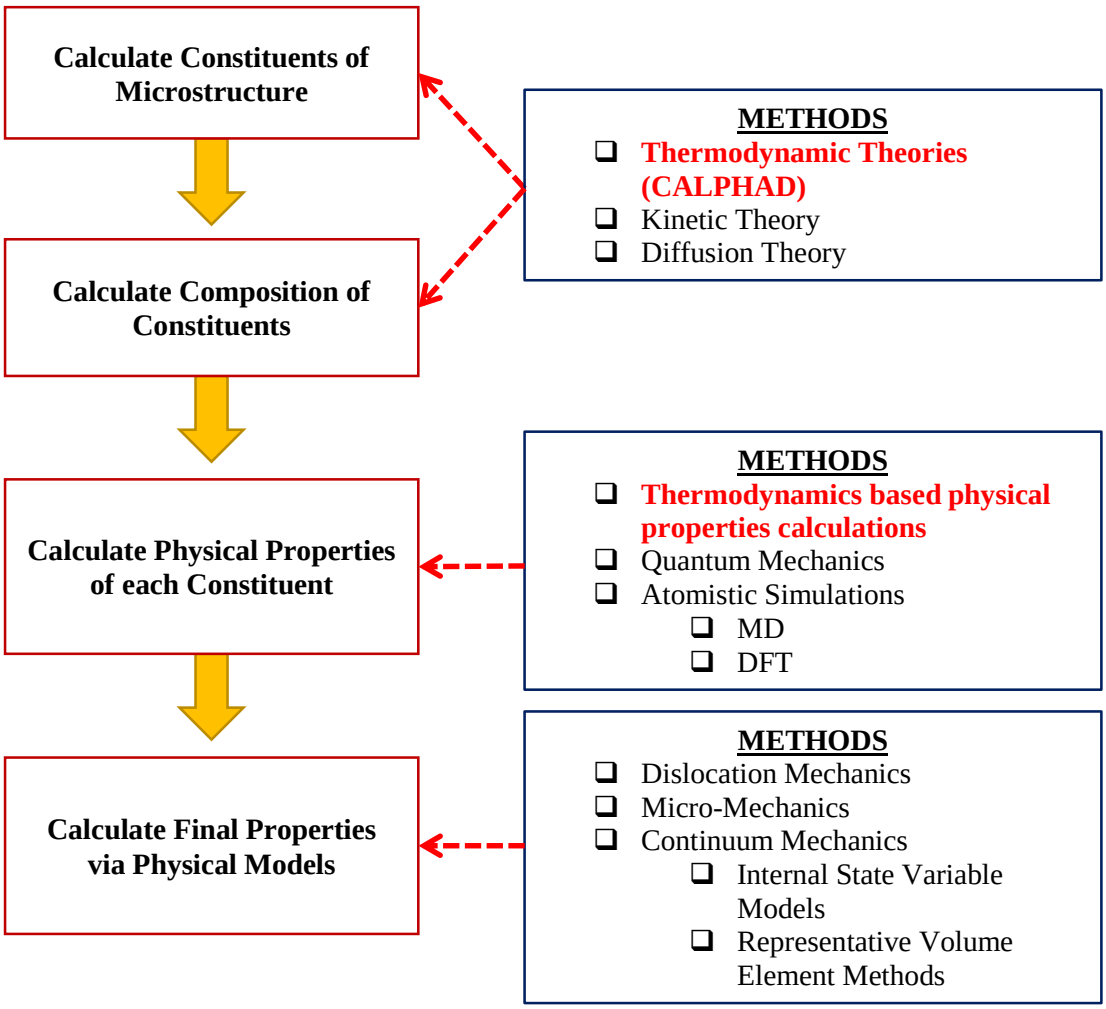

Figure 61: Calculation procedure for material property and methods used for each calculation step.

At first, chemical composition of the steel is used as an input data for the software. Then, CALPHAD method is used in order to determine fractions of phases. Basic

principle of CALPHAD method is the minimization of excess free energy which can be expressed as follows (35):

$$G = \sum_i X_i G_i^0 + RT \sum_i X_i \ln X_i + \sum_i \sum_{j>i} X_i X_j \sum_v \varphi_v (X_i - X_j)^v \quad (35)$$

where, i and j are element indexes in a phase, G^0 is the Gibbs free energy of pure components, φ_v is interaction terms (based on pairwise interactions), X_i and X_j are the mole fractions of elements i and j.

In the third step, determination of properties of each phase is done with thermodynamic based material property calculation. JMatPro® uses basic equation for the Gibbs free energy of a multi-component solution phase, which includes Gibbs free energy of pure components, ideal entropy and interaction terms as expressed in Equation (35). Model that is used in JMatPro® is analogue and based on the Gibbs free energy equation. Interaction parameter is same but not identical with the analogue one as given in Equation (36):

$$P = \sum_i X_i P_i^0 + \sum_i \sum_{j>i} X_i X_j \sum_v \omega_{ij}^v (X_i - X_j)^v \quad (36)$$

where, P is the material property, i and j are element indexes in a phase, P^0 is the property of the phase in the pure element, ω_{ij}^v is a binary interaction parameter, X_i and X_j are the mole fractions of elements i and j.

At the last step of calculation, property of phase mixture is determined by composite theory. Calculation starts for each individual phase then final mixture of phases can be determined by mixture models given in Equations (37) and (38) which is taking into account of the effect of microstructure on final material property. For upper bound of mixture model, following Equation (37) is used;

$$P_{mix} = \sum_{i=1}^{i=j} X_i P_i \quad (37)$$

and for lower bound Equation (38) is used;

$$\frac{1}{P_{mix}} = \sum_{i=1}^{i=j} \frac{X_i}{P_i} \tag{38}$$

where, P_{mix} is the property of mixture, i and j are element indexes in a phase and X_i is the mole fraction of elements i.

4.2.1. Calculation of TTT and CCT diagrams

Furthermore, the code is able to calculate TTT and CCT diagrams almost accurate for general steels, including medium to high alloy steels, tool steels and 13%Cr steels [19, 68]. Thermodynamic models together with kinetic phase transformation models is used for in case of calculating TTT and CCT diagrams. The model used for transformation mainly based on the model developed by Kirkaldy [69] and co-workers. The modified model of Kirkaldy is given in Equation (39):

$$t(P,T) = \frac{1}{\alpha(N)\Delta T^q D} \int_0^P \frac{dP}{P^{2(1-P)/3}(1-P)^{2P/3}} \tag{39}$$

where, $\alpha(N) = \beta^{(N-1)/2}$ and β is an empirical coefficient, N is the ASTM grain size D is an effective diffusion coefficient ΔT is the undercooling below the temperature where austenite is unstable with respect to ferrite, q is an exponent dependent on the effective diffusion mechanism, and P is the fraction transformed.

Once the TTT diagram is calculated it can be transformed into a CCT diagram by the rule of additivity as mentioned in Chapter 2 [68-71]. There are several works published about determination of TTT and CCT diagrams by JMatPro® and their comparison with corresponding experimental results and the literature [19, 68, 72].

4.3. Calculation and Evaluation Procedure

Chemical composition of the material required in order to calculate material properties with calculation procedure mentioned in previous sub-division. Therefore, calculations were based on chemical composition of 100Cr6 as given in Table 2.

Grain size was taken as 7.4 ASTM and austenitization temperature was taken as 850 °C at first. The composition of the austenite present at this temperature is calculated

directly by taking into account of carbide and other second phases present at this quenching temperature. Thus, the code fails in a partial austenitization case. It assumes the case is in the cementite transition temperature so that it calculates 1.81 Wt.% cementite and 98.17 Wt.% austenite present in the microstructure. After then, the code calculates transformation for austenite was taken place in equilibrium at 850 °C for 98.17Wt% austenitic microstructure. Furthermore, it neglects the dissolution of carbide particles during the austenitization which can affect and change the martensite start temperature. As a solution, a trick was suggested by developers of the code in order to achieve similar austenitization condition as in dilatometric tests.

The trick is related with martensite start temperature which was determined experimentally and supposed to be calculated also by the code as 212±1 °C. If the martensite start temperature will able to be obtained at the end of calculation, it can be commented as the amount of austenite decomposed is same with the corresponding dilatometric tests. That's why, martensite start temperature obtained in calculations must be same the temperature obtained from the dilatometric tests. It can be done by changing quenching temperature. Therefore, austenitization temperature was chosen as 812 °C in order to obtain same martensite start temperature with dilatometric tests.

The code computed weight fractions of phases 3.46 Wt.% and 96.52 Wt.% in the microstructure at 812 °C for the cementite and austenite phases respectively. Uniform cooling with a 10 °C/s cooling rate was chosen for quenching properties.

4.4. Results

The effect of diminutive differences in chemical composition on thermo-physical properties were also investigated. Consequently, it was observed that the effect is not significant as it can be seen from the results given in Figure 62.

The difference in compositions can be seen in Table 15. "Composition 1" is the composition used in this study and "Composition 2" is the standard composition for 100Cr6.

Table 15: Compositions used for computational part of the study.

	C	Cr	Si	Mn	Al	Cu	Mo	Ni	O	P
Composition 1	0.99	1.43	0.24	0.36	0.017	0.1	0.02	0.06	$5e^{-5}$	0.016
Composition 2	0.99	1.47	0.25	0.35	0.050	0.3	0.1	0.1	$15e^{-4}$	0.025

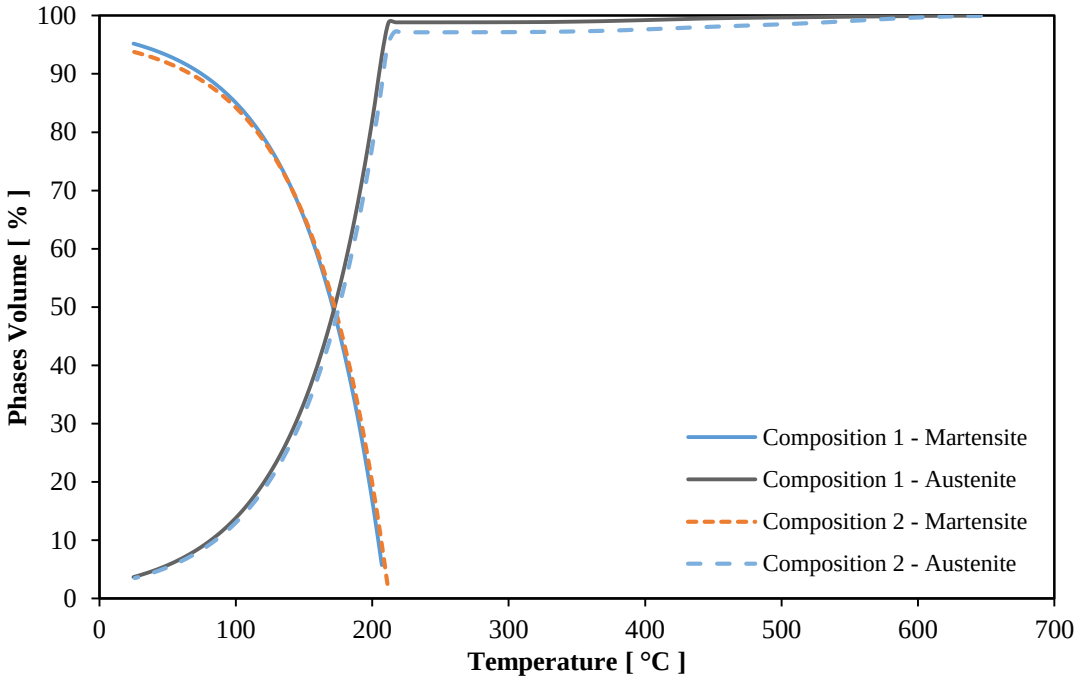

Figure 62: Comparison of phase amounts between diminutive differences in chemical composition of steel 100Cr6. "Composition 1" is the composition used in this study and "Composition 2" is standard composition for 100Cr6.

Thermo-physical properties, density, specific heat, thermal conductivity, enthalpy, Young's modulus and Poisson's ratio, were computed for each phase and results were given in Figure 63, Figure 64, Figure 65, Figure 66, Figure 67 and Figure 68 respectively as graphical representations. Data available in the literature [12, 13] were also indicated on the figures in order to make a comparison with computed results. From these figures, it can be commented that good agreements for the properties, density, specific heat, thermal conductivity and enthalpy, have been established between the computed results and the literature.

On the other side, Young's modulus and Poisson's ratio for the austenitic phase different from the literature as in Figure 67 and Figure 68. This is due to instrument used for measuring the dilation during mechanical tests in the experimental work of Acht et. al. [12]. Stiffness of the instrument and the method for measuring the dilation of the specimen may affect the flow curve measured. It is highly doubted that the measured data in the experiments they performed consists of the dilation of the punches and other components of the instrument itself as in experiments performed in this study.

TTT and CCT diagrams computed according to ASTM grain size 7.4 and austenitization temperature was taken as 812 °C due to problems mentioned above. Results were given in Chapter 3 together with experimentally determined diagrams and diagrams found in the literature.

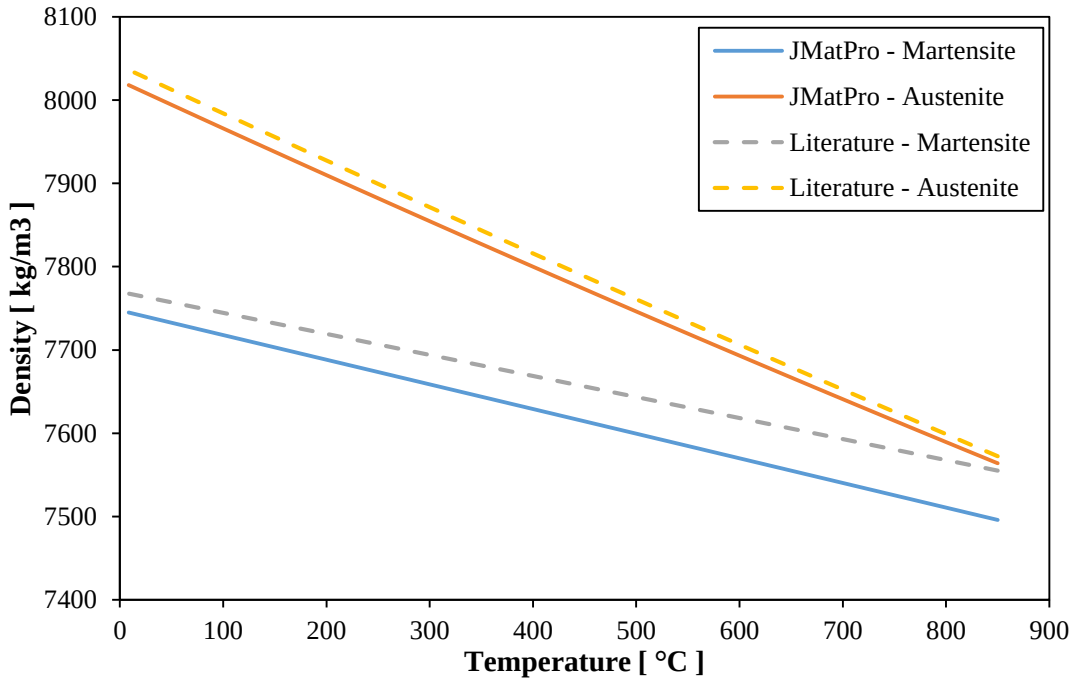

Figure 63: Comparison of density values computed (solid) and found in the literature (dashed) for martensitic and austenitic phases as a function of temperature.

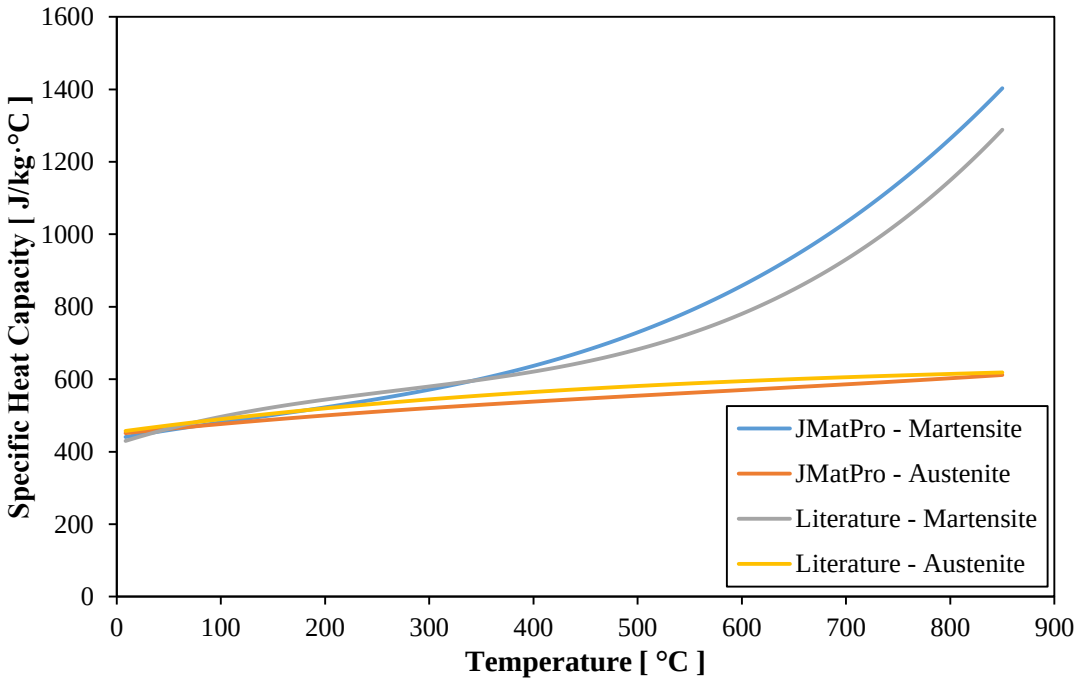

Figure 64: Specific heat for each phase of 100Cr6 with respect to temperature.

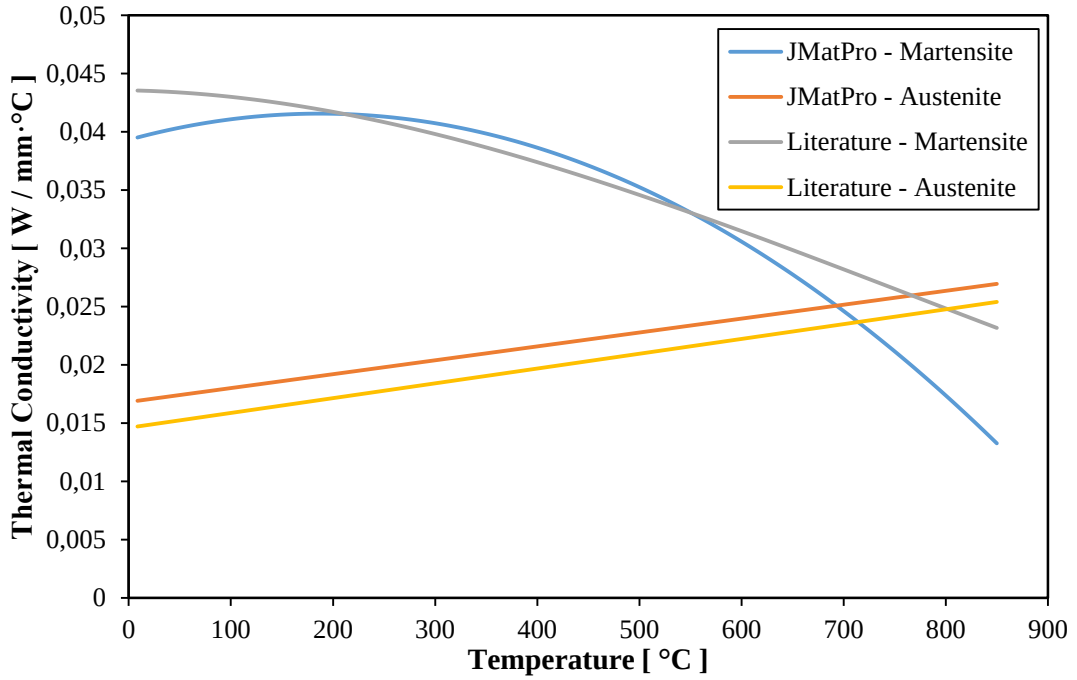

Figure 65: Thermal conductivity for each phase of 100Cr6 with respect to temperature.

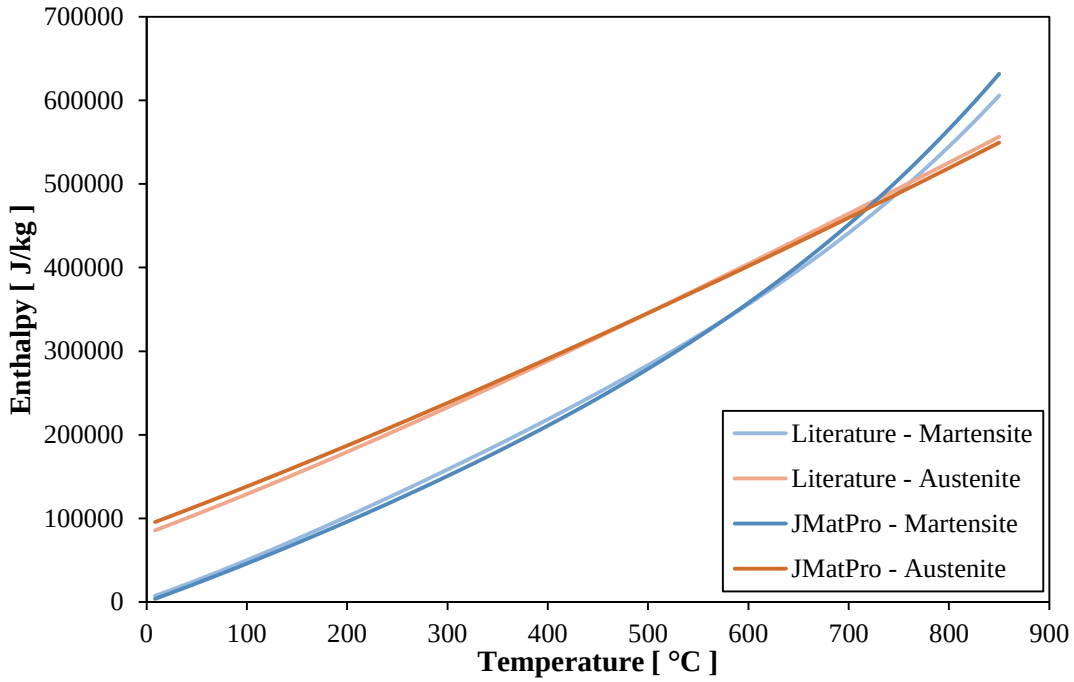

Figure 66: Enthalpy for each phase of 100Cr6 with respect to temperature.

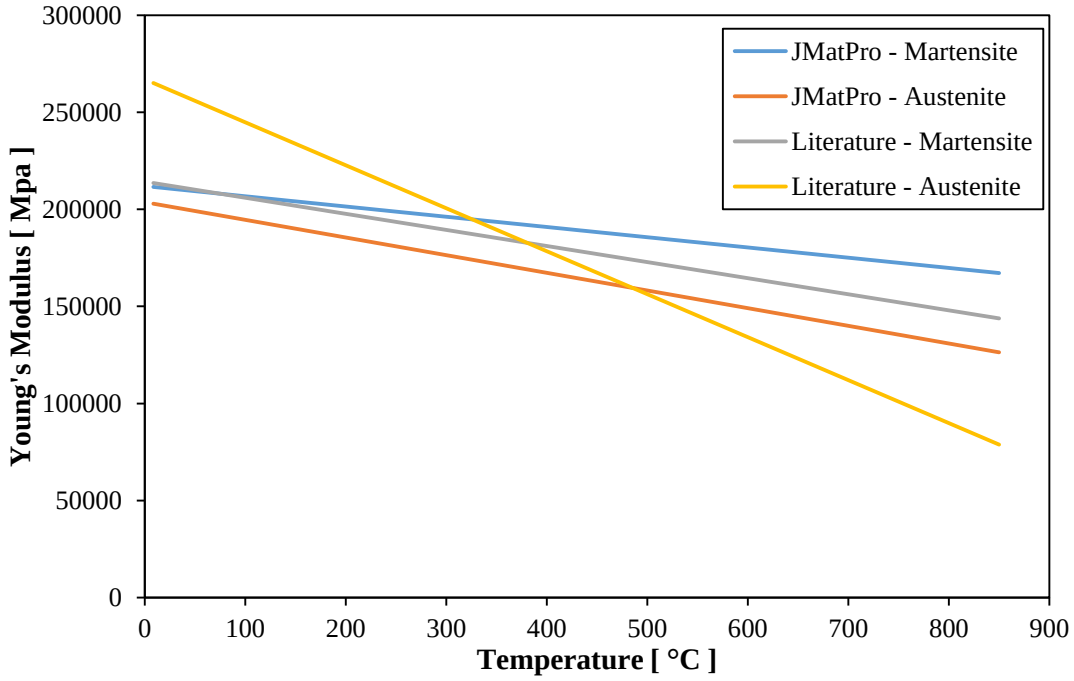

Figure 67: Young's modulus for each phase of 100Cr6 with respect to temperature.

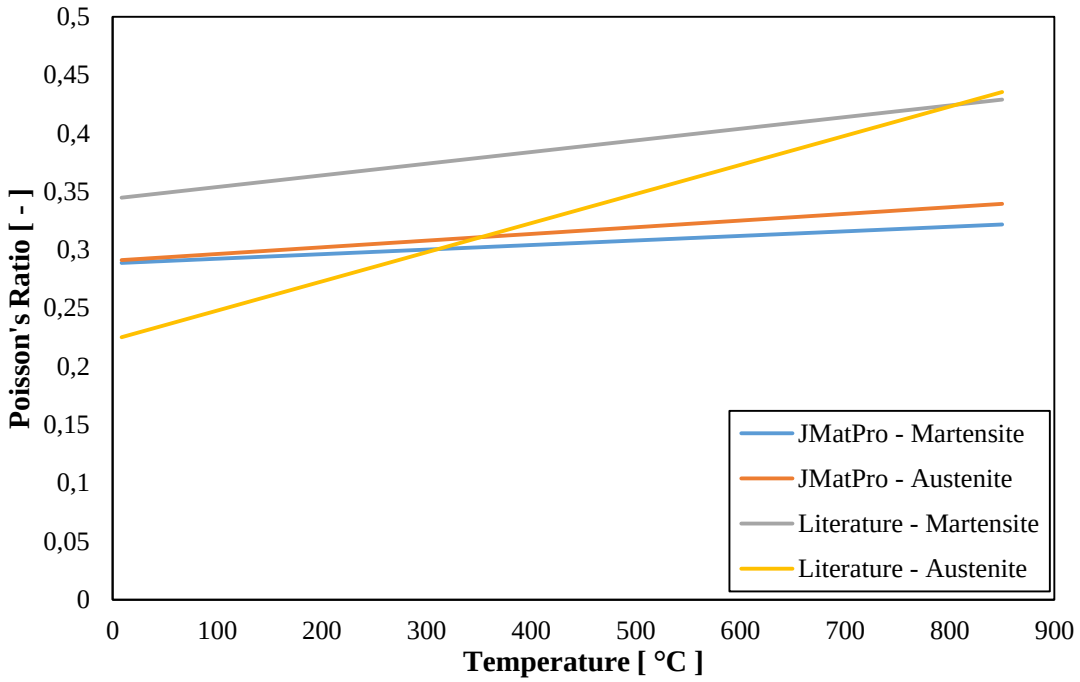

Figure 68: Poisson's ratio for each phase of 100Cr6 with respect to temperature.

Additionally, thermo-physical properties for the soft phase were also computed with JMatPro®. However, their results were not given in these graphical representations since they were summarized in Table 16, Table 17 and Table 18 as polynomials with respect to temperature. The values given in Table 16, Table 17 and Table 18 for related material properties must be used with following relation (40):

$$P(T) = A_o + A_1T^1 + A_2T^2 + A_3T^3 + A_4T^4 \quad (40)$$

where, *P(T)* is the material property at a given temperature, *T* is temperature and A_n is the constant for related material property which is given in Table 16, Table 17 and Table 18.

Table 16: Summary for calculated and determined Thermo-Physical Properties.

Property	Phase	A_0	A_1	A_2	A_3	A_4
Specific Heat Capacity [J/kg·°C]	**Martensite**	436.51	0.4875	$-6.16*10^{-04}$	$1.62*10^{-06}$	
	Austenite	448.67	0.3007	$-2.49*10^{-04}$	$1.42*10^{-07}$	
Enthalpy [J/kg]	**Martensite**	55776.99	436.65	$2.42*10^{-01}$	$-1.99*10^{-04}$	$3.99*10^{-07}$
	Austenite	147540.57	450.35	$1.45*10^{-01}$	$-7.68*10^{-05}$	$3.37*10^{-08}$
	Spheroidite	-17.59	0.4354	$2.20*10^{-04}$	$-1.21*10^{-07}$	$2.43*10^{-10}$
Thermal Conductivity [W / mm·°C]	**Martensite**	0.0393	$2.40*10^{-05}$	$-6.43*10^{-08}$		
	Austenite	0.0168	$1.19*10^{-05}$			
Density [kg/m^3]	**Martensite**	7738.13	-0.2661			
	Austenite	8005.31	-0.5136			
	Spheroidite	7816.67	-0.3443			
Thermal Strain with Transformation Strain, T_{ref} 20°C [-]	**GKZ to M**	$-8.28*10^{-03}$	$2.22*10^{-05}$			
	GKZ to A	$3.09*10^{-03}$	$1.17*10^{-05}$			
Transformation Strain, T_{ref} 20°C [%]	**GKZ to M***	0.3325				
	GKZ to A**	-0.7835				
	A to M***	1.1160				

M: Martensite, A: Austenite, GKZ: Spheroidite, (*) GKZ to M: Spheroidite to Martensite Transformation, (**) GKZ to A: Spheroidite to Austenite Transformation, (***) A to M: Austenite to Martensite Transformation.

Table 17: Summary for calculated and determined Thermo-Mechanical Properties.

Property	Phase	A_0	A_1
Ramberg-Osgood Parameter n_{RO} [-]	**Martensite**	$7.97*10^{-02}$	$1.27*10^{-04}$
	Austenite	$1.22*10^{-01}$	$3.88*10^{-05}$
	Bainite	$1.58*10^{-01}$	$4.44*10^{-05}$
Ramberg-Osgood Parameter K_{RO} [MPa]	**Martensite**	$4.35*10^{+03}$	-4.11
	Austenite	$1.06*10^{+03}$	-1.09
	Bainite	$6.73*10^{+03}$	-8.74
Coefficient of Thermal Expansion α [10^{-6} °C^{-1}]	**Martensite**	11.69	
	Austenite	22.19	
	Spheroidite	15.06	
Young's Modulus E [MPa]	**Martensite**	$2.12*10^{+05}$	$-5.27*10^{+01}$
	Austenite	$2.04*10^{+05}$	$-9.10*10^{+01}$
Poisson's Ratio [-]	**Martensite**	0.344	0.0001
	Austenite	0.223	0.00025

Table 18: Summary for calculated and determined Thermo-Metallurgical Properties.

Property	**Phase**	**A_0**
Critical Temperatures for *GKZ* to *A* Transformation [°C]	**Ac1**	773.4
	Ac3	817.3
M_s Temperature (Ref. transformation at %0.7) [°C]	**A to M*** **	212 ± 1
M_f Temperature (Ref. transformation at %99.9) [°C]	**A to M**	-94 ± 1
Koistinen-Marburger Constant Ω [-]	**A to M**	102.001
Koistinen-Marburger Exponent *n* [-]	**A to M**	1.455
Transformation Plasticity Constant K^{tp} [1/MPa]	**A to M**	$1.06*10^{-05}$
	A to M (Theoretical)	$1.32*10^{-05}$
	A to B** **	$6.82*10^{-05}$

M: Martensite, A: Austenite, B: Bainite, (***) A to M: Austenite to Martensite Transformation, (****) A to B: Austenite to Bainite Transformation.

CHAPTER 5

JUSTIFICATION AND EVALUATION OF MATERIAL DATA SET

5.1. Implementation of the Material Data Set into SYSWELD®

In this study, construction of a material data set for steel 100Cr6 was aimed in order to use the data set in heat treatment simulations. After the experimental and computational work presented in the previous chapters, constructed data set was implemented into SYSWELD® simulation software for this purpose.

At first, the material data set was converted into a polynomial functions of temperature for a range of 0-1000°C. Degree of the polynomials were determined for each material property and for each phase respectively. Values standing between two data points can be calculated by the simulation code if it is given as a first-degree/linear polynomials. On the other side, if the degree of polynomials higher than one, then the related property is introduced as a table to the code. After the implementation of the material data set, verification simulations were performed and results were compared with both numerical and experimental results found in the literature.

5.1.1. Implementation of Thermo-Physical Properties

Thermo-physical properties of 100Cr6 such as thermal conductivity, specific heat, enthalpy and density values were implemented to the code one by one for each phase. Thermal conductivity [W/(mm·K)] values of ferritic and austenitic phases were introduced as a table and as a linear function respectively, while specific heat [J/(kg·K)] was introduced as tables for both phases. Moreover, enthalpy [J/kg] and

density [kg/mm^3] values of ferritic, martensitic and austenitic phases were defined to the code as tables.

5.1.2. Implementation of Thermo-Metallurgical Properties

Thermo-metallurgical properties of 100Cr6 were implemented as phase transformation data for each phase in accordance with metallurgical models defined in the code. The code includes JMA and Leblond metallurgical models and these models might be used for diffusional phase transformations. Furthermore, for displacive phase transformations, Koistinen-Marburger model had been implemented to the code and it can be used with diffusional models simultaneously. However, as mentioned in Chapter 3, Koistinen-Marburger model was not giving good results at the room temperature when compared with the experimental results. That's why, Koistinen-Marburger model was modified in order to give better results as discussed in Chapter 3. SYSWELD® is giving an opportunity to users that transformation kinetics can be defined with Simplified Fortran codes by user. However, the user-programmed transformation kinetics cannot be used together with metallurgical transformation models included in the code. The code also has a shared library USMETA routine which includes metallurgical transformation model of JMA. Modified Koistinen-Marburger model was added onto USMETA routine in order to solve this problem. However, there is no need to use diffusional phase transformation models for the case given in following sub-division since only martensitic phase transformation is expected to be occurred due to given quenching conditions. Therefore, only modified Koistinen-Marburger model was defined to the code as a transformation model by Simplified Fortran program.

5.1.3. Implementation of Thermo-Mechanical Properties

Thermo-mechanical properties of 100Cr6 such as elastic modulus, Poisson's ratio, thermal strain, yield strength and hardening behavior of the steel were defined to the code separately for each related phase. Elastic modulus [MPa], Poisson's ratio [-] and thermal strains [1/°C] for austenitic and martensitic phases were defined as linear polynomials while yield strength [MPa] for each phase introduced as tables. Furthermore, hardening behavior of austenitic and martensitic phases were

implemented to code as tables at a given temperatures by extracting the yield strength value from nominal stress values of related phase. Transformation plasticity constant, K^{tp}, was defined as constant value for all phases since the code assumes transformation plasticity is equal for all phases.

5.2. Through-Hardening Simulation for Conical Bearing Ring

In this part, through-hardening process for outer ring of conical bearing was studied. Verification of the data set performed for the through-hardening simulation of the conical bearing ring and results were compared with numerical results obtained by Acht [13].

Acht et al. [13] had been studied through-hardening process of conical bearing ring which was made from 100Cr6 and dimensions of the outer ring were given in Figure 69. Furthermore, they have supported their numerical results with experimental results. In performed simulations, same process parameters and conditions were used as in the work of Acht et al. in order to make a meaningful comparison.

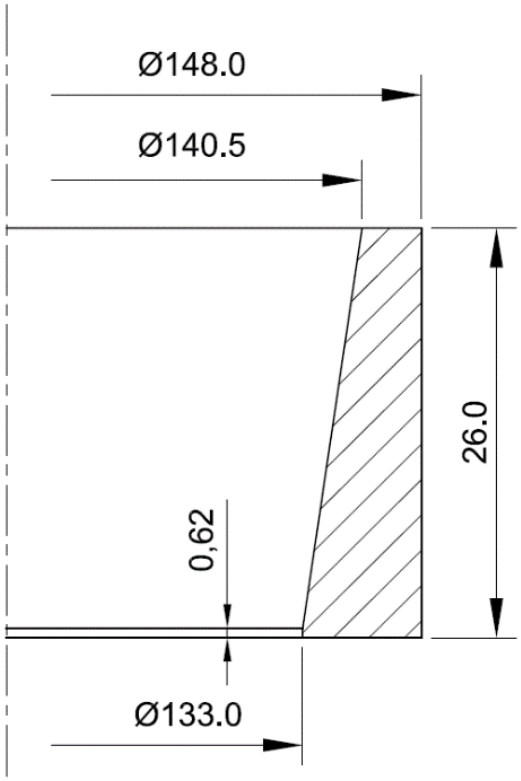

Figure 69: Conical bearing ring used in through-hardening simulation.

5.2.1. Details of Simulation

For verification of the data set, simulations were performed with finite element software code, SYSWELD®, using 2-D axi-symmetrical option with isotropic strain hardening model.

First step for the simulation is meshing of the geometry. Half of the ring is modelled in 2-D since axi-symmetrical option is used. The mesh given in Figure 70 has been generated manually, then it was subdivided via automatic mesher. Important nodes, which are used as data points for comparison of the simulation results, are also indicated on the same figure with boundary conditions.

Element type was selected as 8-noded quadrilateral elements with reduced integration since it is known that quadrilateral type of elements are giving good results when compared with 4-noded elements in the case of bending load by avoiding shear locking. Moreover, in order to reduce computation time and efficiency, reduced integration is used with quadrilateral elements. There are 1300 quadrilateral elements with 4071 nodes used in the simulations.

As an initial condition, it is also assumed that component has a homogenous temperature distribution through-out its cross-section with austenitic microstructure. Therefore, %100 austenitic phase was defined as an initial phase for all of the elements and all of the nodes.

The conical bearing ring was quenched to the room temperature from a temperature of 850 °C inside a gas nozzle field. Heat transfer coefficients for the gas flow over the component were taken as 444 W/(m^2K) for sides, 205 W/(m^2K) for bottom face, and 317 W/(m^2K) for the top face of the conical ring.

Boundary conditions for heat transfer coefficients are shown in Figure 70 as blue arrows. Clamping applied on the ring in y-direction, $U_y=0$, is also shown in the same figure as a red arrow.

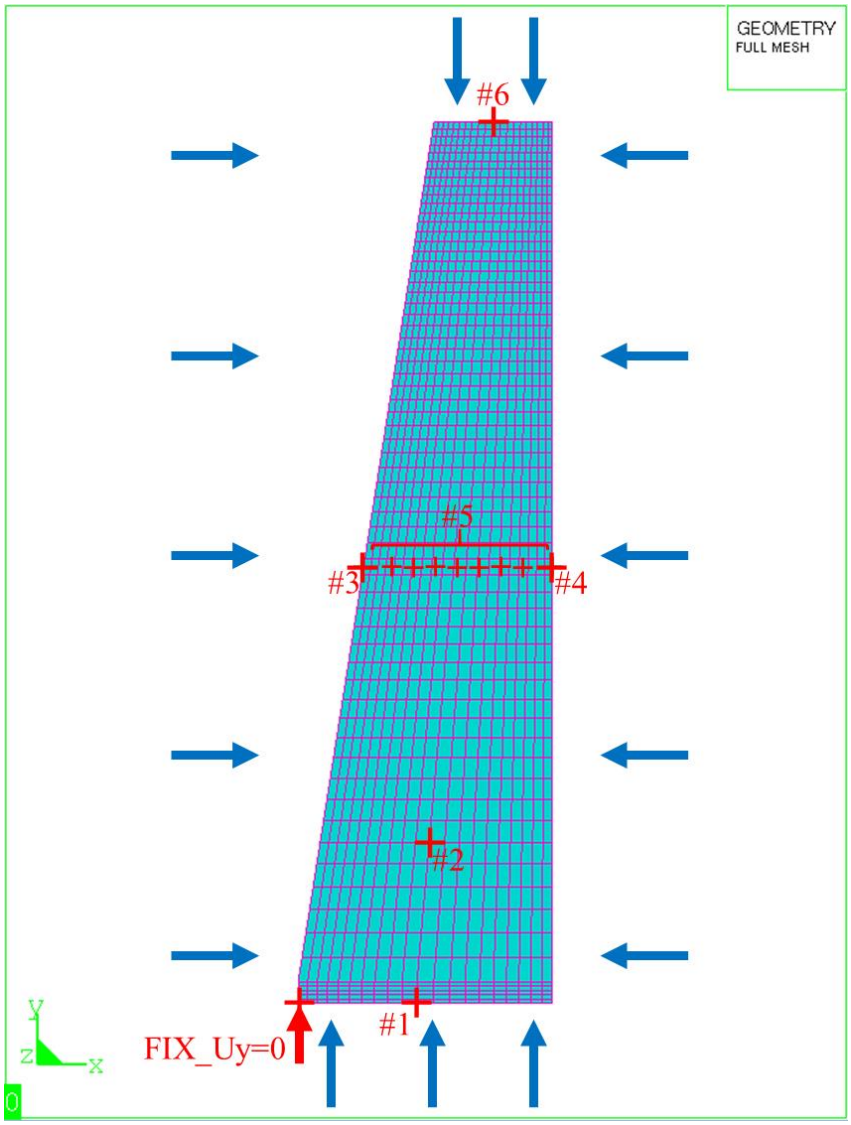

Figure 70: The mesh used in simulations. Boundary conditions (arrows) and important nodes (+) are also indicated. #1 bottom side, #2 core, #3 inner side, #4 outer side, #5 group of nodes represented as line and #6 top side.

5.2.2. Results

5.2.2.1. Cooling Curves

A comparison of cooling curves with the literature is given in Figure 71. Detailed view of the same figure is given in Figure 72. As it can be seen from the Figure 71, cooling curves obtained from simulation and cooling curves given in the literature are in good agreement regardless of the position of nodes.

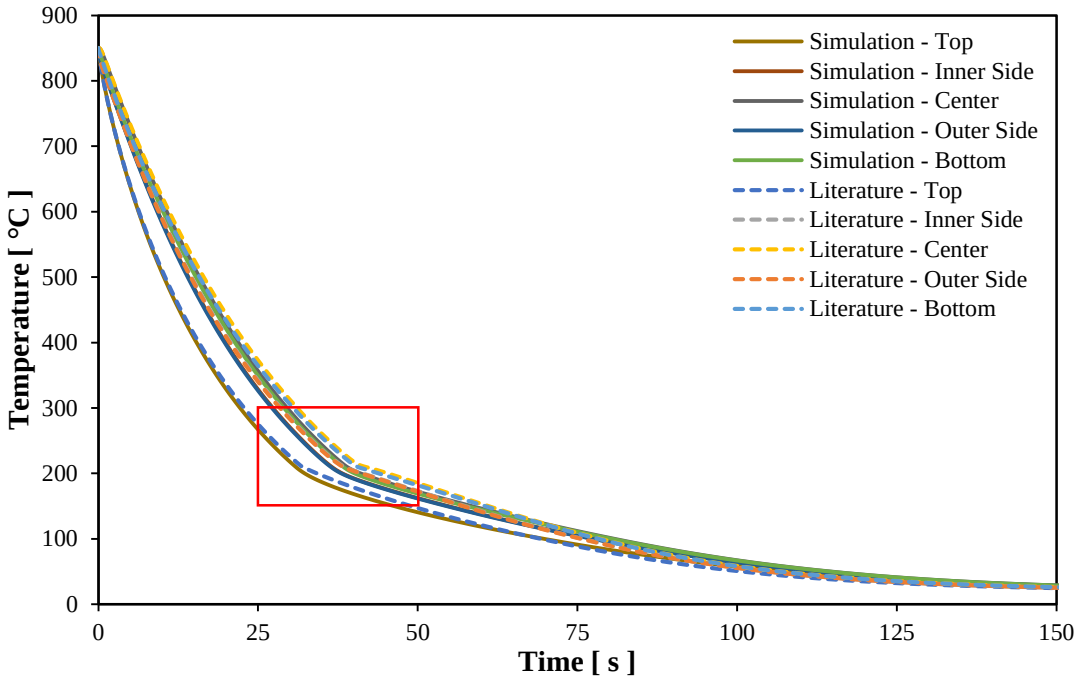

Figure 71: Comparison of cooling curves obtained from simulations with literature.

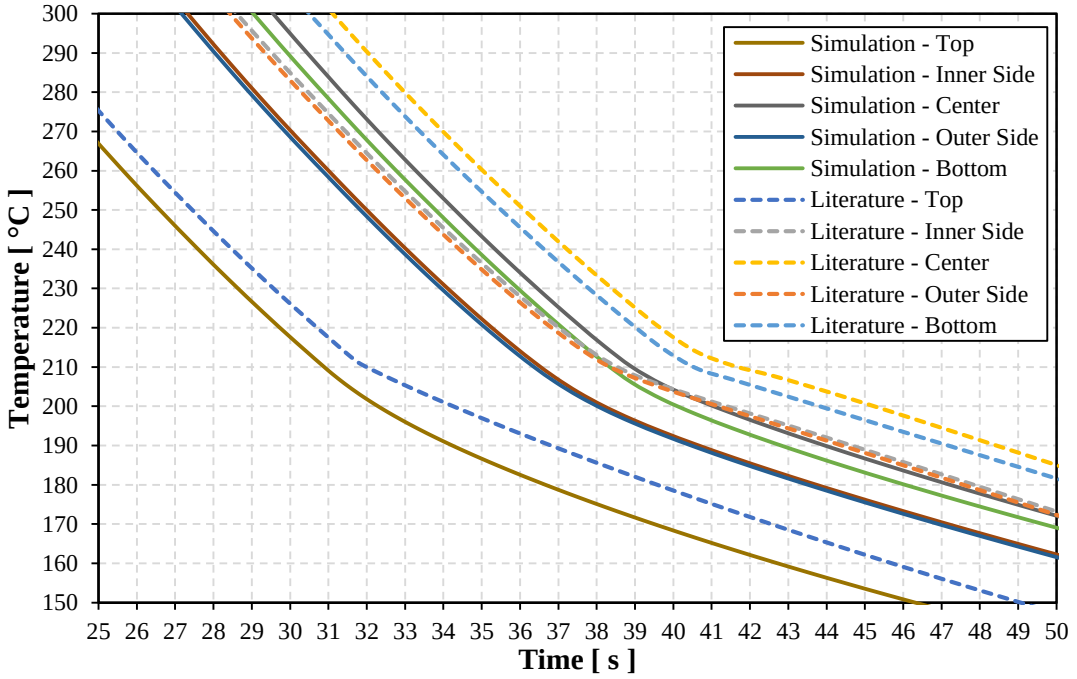

Figure 72: Detailed view of cooling curves given in Figure 71.

The ring is completely cooled down to room temperature approximately in 150 seconds as it can be seen from the Figure 71.

It is thought that the temperature difference observed between literature and our simulation is probably due to difference in transformation kinetics used for simulations. Koistinen-Marburger model was modified and modified version was used in this study because of the problems explained in Chapter 3.

As it can be seen from the cooling curves, temperature is increased around martensite start temperature which is due to latent heat released by commencing of phase transformation.

It is also observed that, relatively thin top-side of the ring was cooled down faster than other sides about 50-70°C as it can be seen from Figure 72 which is resulting to completion of phase transformation earlier at the top-side than the bottom-side of the ring. This temperature difference is might be due to ring geometry and due to difference in heat transfer coefficients (HTC) applied for each side of the ring.

5.2.2.2. Phase Proportions

Figure 73 shows the comparison of martensitic transformation between simulations and the literature. The resulting phase constituents after simulations consist of mostly martensitic phase with %10 retained austenite as expected. Since retained austenite value was taken into consideration during the creation of the material data set, good agreement also established between experimental value and simulated value which is %3 lower than the experimental value (%13 ± 1.5).

As it can be seen from the Figure 73, Martensitic phase fractions of the simulation and the literature are different at room temperature. The difference observed between simulation and literature at room temperature is about %5 for martensitic phase. Minor differences between phase proportions of the literature and the simulated values might be due to different kinetic models used for displacive phase transformations in simulations.

Detailed view of red box indicated on Figure 73 is given in Figure 74. As it can be seen from Figure 74, maximum difference between core and top face of the ring is about %17 for martensitic phase. This difference is due to temperature gradient

generated during cooling with effect of HTC and geometry as explained in the previous sub-section.

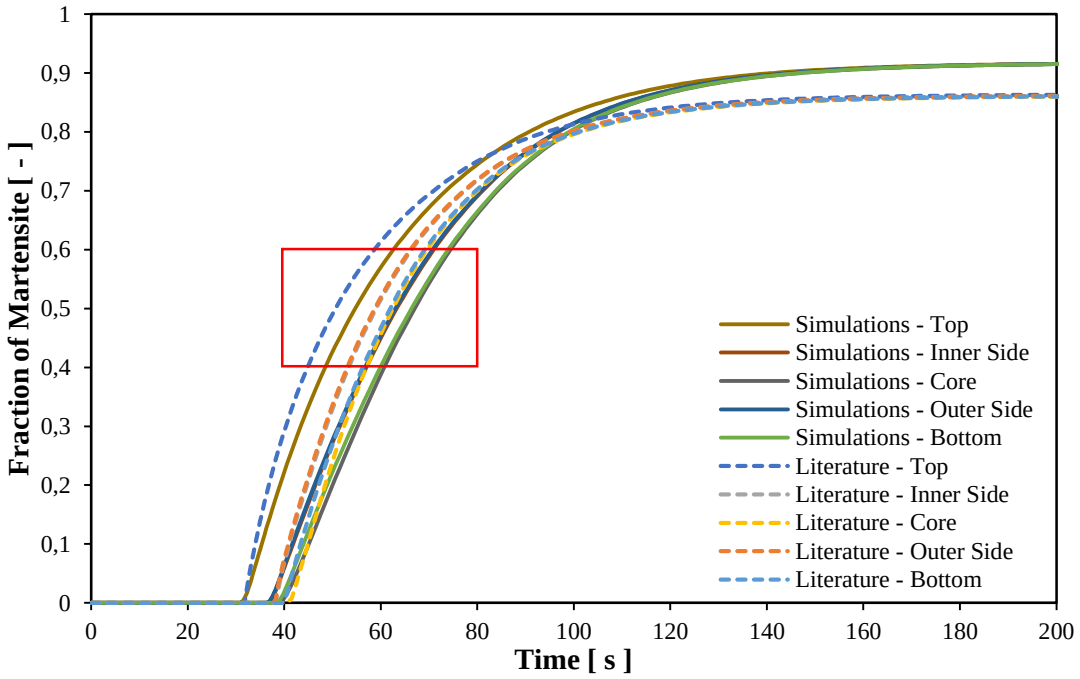

Figure 73: Phase fraction of martensite during quenching. Comparison of martensitic transformations results with the literature.

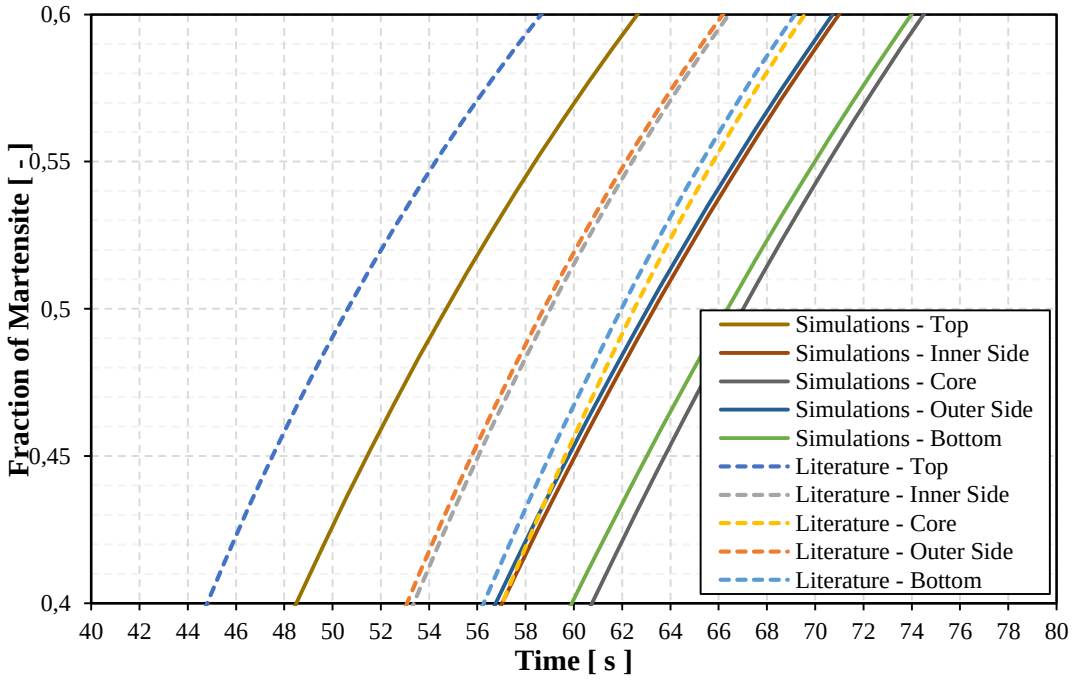

Figure 74: Detailed view of the red box indicated in the Figure 73.

5.2.2.3. Dimensional Changes

In Figure 75 and Figure 76, results of the dimensional change of the ring and tilting behavior of the ring were shown. In Figure 75, outer radius of the ring for both simulations and literature were given while in Figure 76 bottom-side of the ring was represented.

Experimentally and theoretically calculated TRIP constants were tested as mentioned in Chapter 3 and simulation results for both TRIP constants are given in Figure 75 and Figure 76.

Ring shows a tendency to tilt towards to center of its axis during high pressure gas quenching as it can be seen from the Figure 75 and Figure 76. This tendency is represented at Figure 77 schematically. TRIP constant taken as $7x10^{-5}$ [MPa] for the work in the literature and taken as $1.06x10^{-5}$ [MPa] and $1.32\ x10^{-5}$ [MPa] for simulations performed in this study.

The amount of tilting is highly dependent on TRIP constant therefore, difference in TRIP constant may affect the tilting behavior significantly [73]. Stresses might be generated due to temperature gradient in axial direction which is resulting in TRIP effect. This phenomena was corrected as it can also be seen from the results of simulations given in Figure 75 and Figure 76.

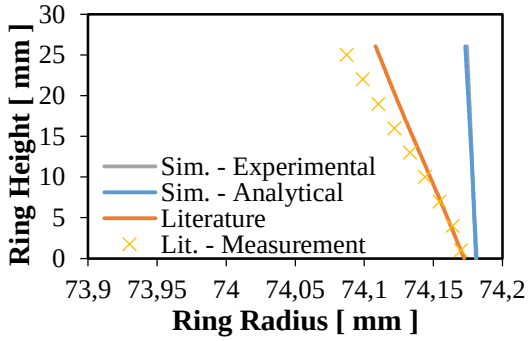

Figure 75: Changes in outer radius of conical bearing ring.

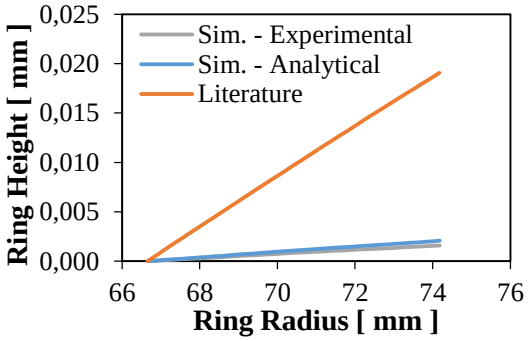

Figure 76: Changes in bottom face of the conical bearing ring.

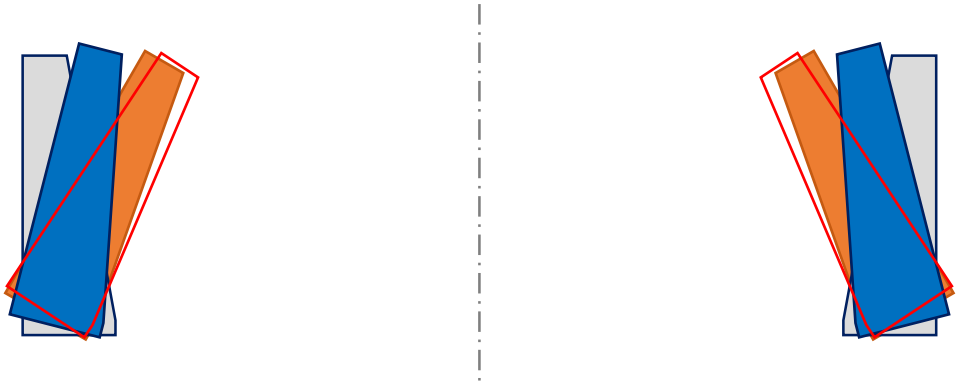

Figure 77: Representative tilting of the rings. Nominal shape (gray) and deformed shapes for both literature (orange) and simulations performed (blue) are also given. Measurement results found in the literature indicated as red line.

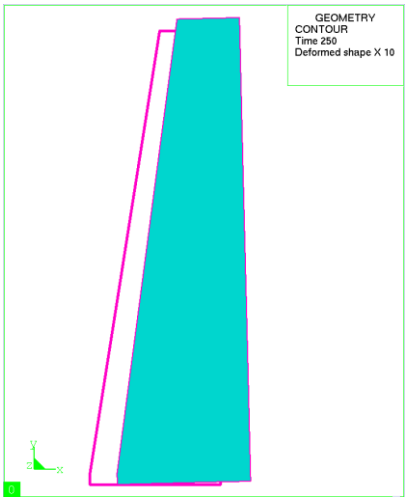

Figure 78: Final shape of conical ring for the literature data [13] (green). Shape of the ring before the simulation is indicated as the red box.

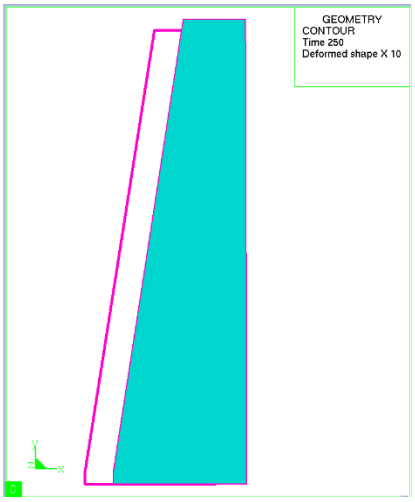

Figure 79: Final shape of conical ring for data set created for this study (green). TRIP constant taken as 1.06×10^{-5} [MPa].

Final shape of the ring is shown in Figure 78 and Figure 79 for both literature and simulation. As it can be seen from the Figures, ring expanded after heat treatment process, as expected. Additionally, tilting behavior towards to center of the ring axis might also be observed from these Figures.

5.2.2.4. Evolution of Stresses during Quenching

During quenching of the conical ring, evolution of the internal stress field can be summarized in 4 critical stages as in follows. At the first stage, surface cools faster

than the core since quenching gas is immersed to the surface first. However, it should be noted that, as it can be seen from the cooling curves given in Figure 71 and Figure 72 bottom side surface of the ring cools slower than other surfaces. Thermal contraction is observed due to cooling of austenite at the first stage. Different thermal contraction levels might be observed due to thermal gradient between surface and core of the ring (Figure 80). Tensile stresses are generated on the surface of the ring while on the other side compressive stresses are present at the core (Figure 80).

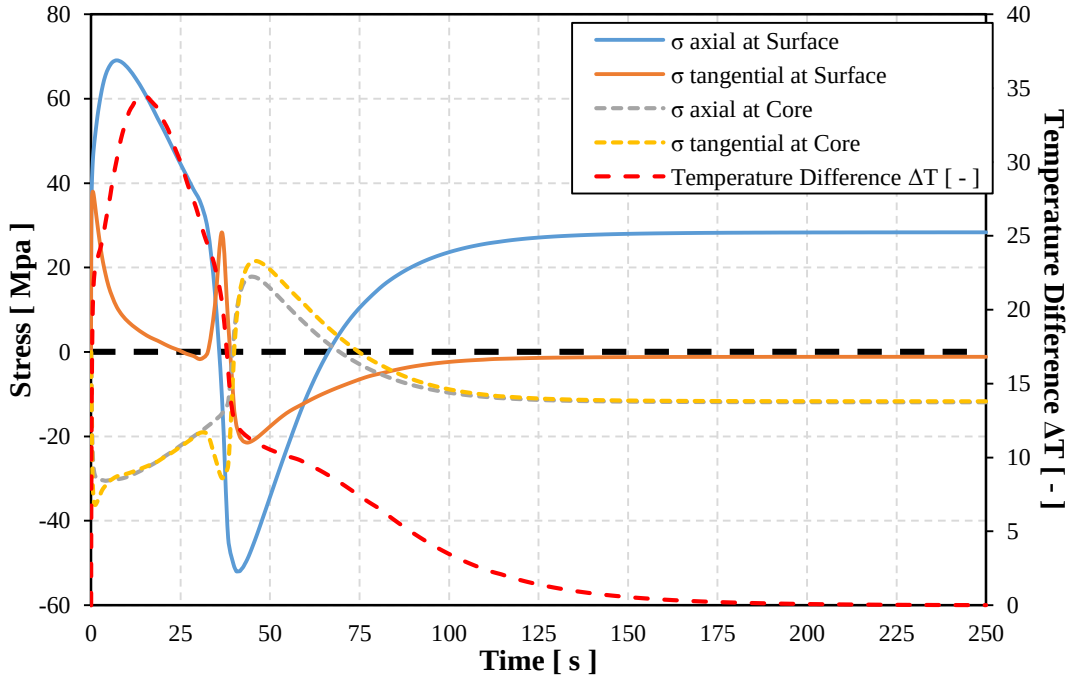

Figure 80: Variation of axial and tangential components of internal stresses at core and surface during quenching with temperature difference between core and surface of the conical ring.

Maximum internal stress level is observed on the conical ring at the time of 7 seconds for our case and 16 seconds for the work in the literature. As it can be seen from the Figure 81 and Figure 82 tangential component of the internal stress for our case is observed as 97 MPa and axial component is observed as 69 MPa since temperature gradient is maximum at that point.

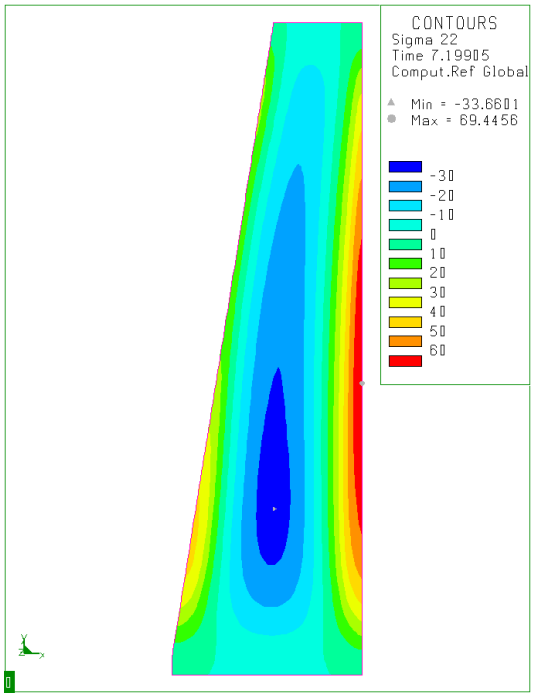

Figure 81: Distribution of axial component of the internal stresses observed on the conical ring at 7th seconds.

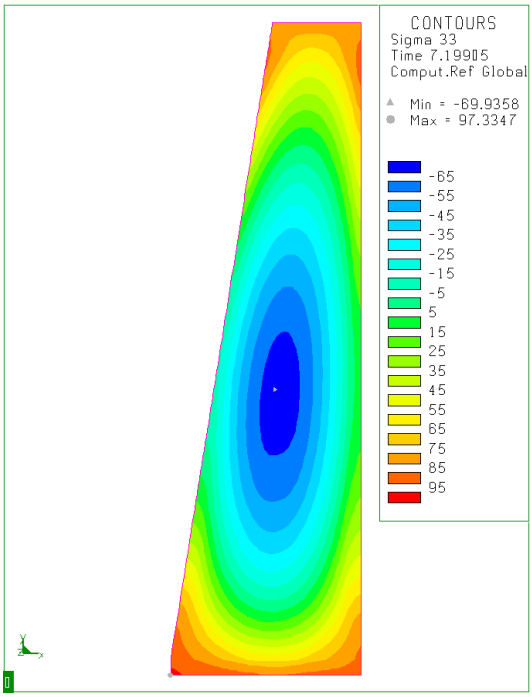

Figure 82: Distribution of tangential component of the internal stresses observed on the conical ring at 7th seconds.

At the second stage of the quenching, martensitic phase transformation is introduced. Surface reaches M_s temperature before the core and martensitic phase transformation begins from the surface while austenitic phase at the core shrinks with decreasing temperature (Figure 80). Because of the initiation of martensitic phase transformation on the surface, surface tries to expand and gets into compression while core withstand it with tensile stresses (Figure 83).

The distribution of internal stresses through cross-section of the ring are given in Figure 84 and Figure 85 for axial and tangential components of the internal stresses at a time of 40 seconds, when the martensitic phase transformation was initiated at the surfaces.

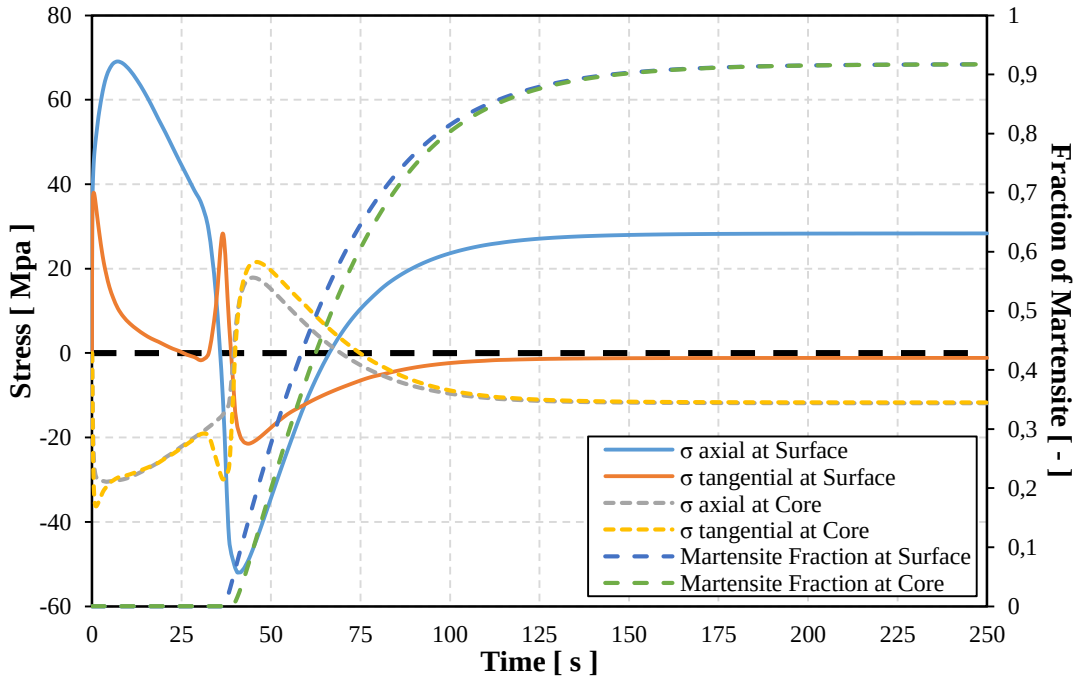

Figure 83: Variation of axial and tangential components of internal stresses at core and surface during quenching with fraction of martensite calculated at core and surface of the conical ring.

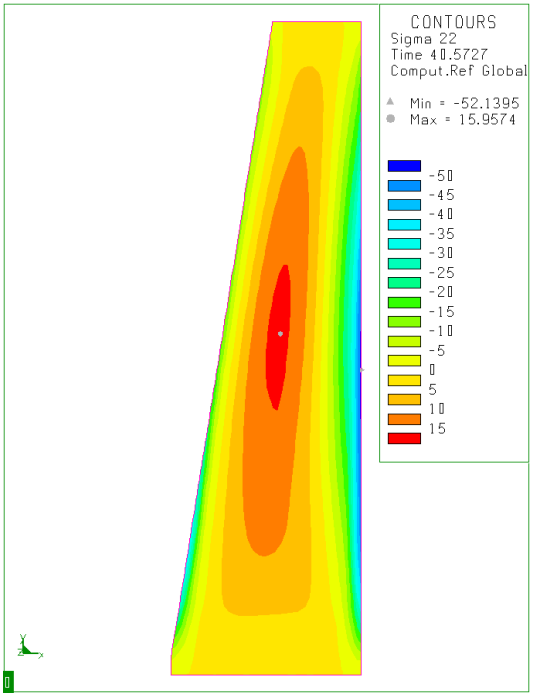

Figure 84: Distribution of axial component of internal stresses observed on the conical ring at 40th seconds.

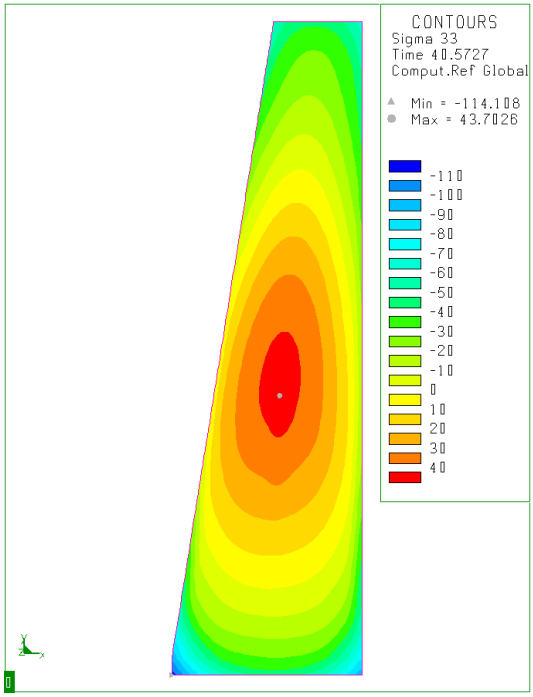

Figure 85: Distribution of tangential component of internal stresses observed on the conical ring at 40th seconds.

Internal stresses are not large enough for classical plastic deformation of austenite as it can be seen from the Figure 86. However, the deformation observed on the ring occurs almost only by transformation plasticity. Von Mises stresses calculated at core and surface of the ring is below the yield strength of austenite for temperature interval of 750°C to 25°C. Although, Von Mises stress calculated at surface of the ring is observed as higher than theoretical yield strength of austenite for the temperatures above 750°C. That's why, it can be said that small amount of classical plastic deformation might be occurred at the outer surface of the ring for a short period of time.

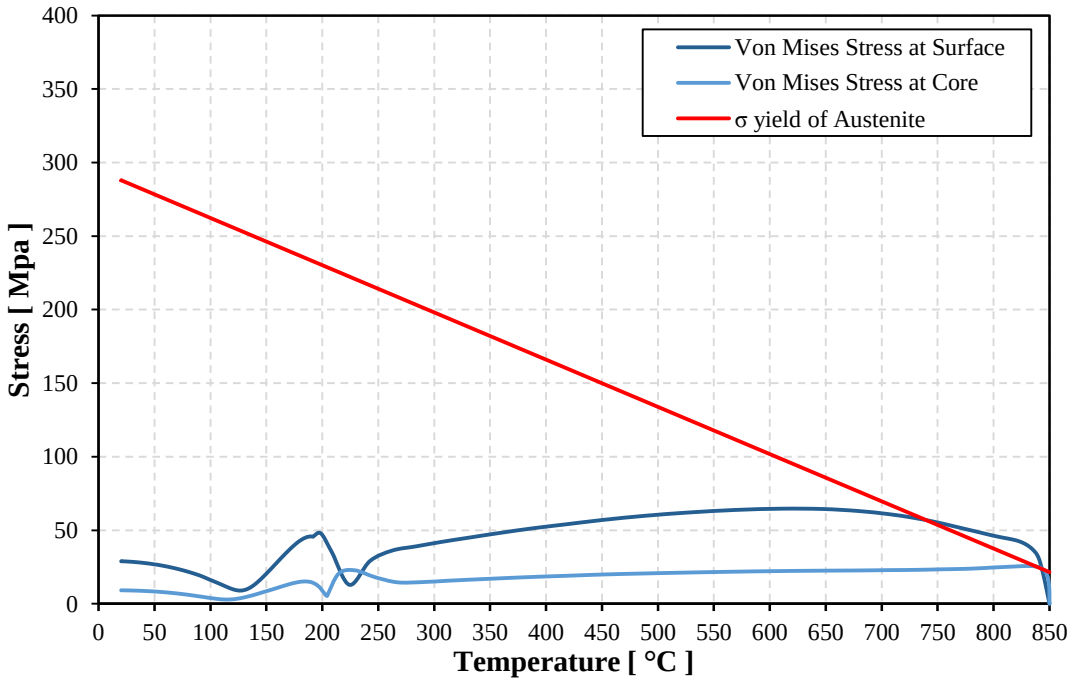

Figure 86: Von Mises Stresses calculated for conical ring at the core and surface. Yield strength of austenite is also indicated.

At the third stage of quenching, surface is completely transformed to the martensitic phase while martensitic phase transformation is initiated at the core. Surface expands with the effect of phase transformation while surface responds with contraction due to cooling of martensitic phase. The core gets into compression stresses and surface tries to balance it with tension.

At the last stage of quenching, phase transformations are almost completed for both surface and the core of the ring. Internal stresses for both core and surface of the ring decrease due to thermal contraction during cooling throughout of cross-section. The distribution of axial and tangential components of residual stresses at the end of simulation are given in Figure 87 and Figure 88. As it can be seen from the figures, residual stresses are decreased to the lower levels as expected.

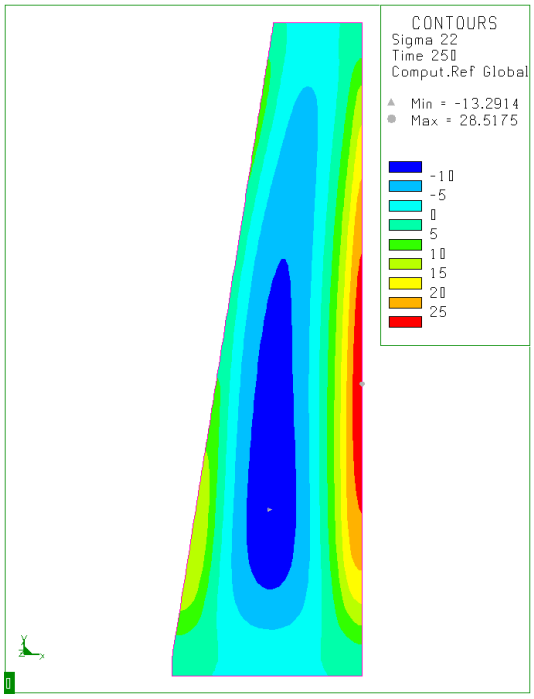

Figure 87: Distribution of axial component of residual stresses observed on the conical ring at 250th seconds.

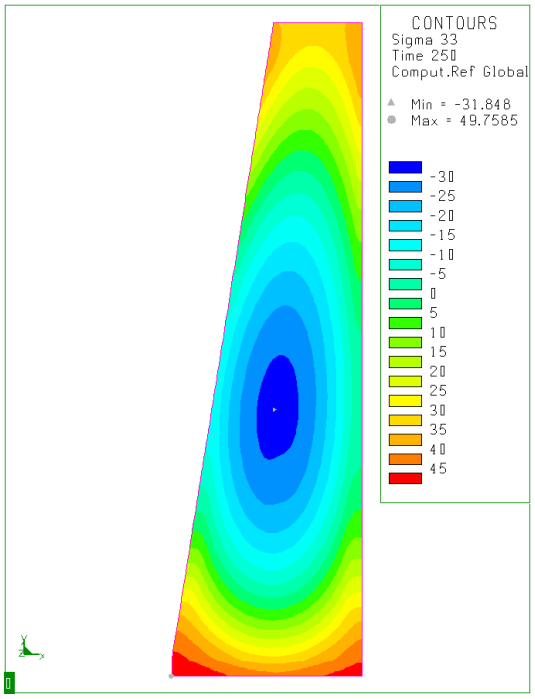

Figure 88: Distribution of tangential component of residual stresses observed on the conical ring at 250th seconds.

Internal stresses observed for the group of nodes represented as #5 in Figure 70 are given in Figure 89 and Figure 90 for axial and tangential components of internal stresses respectively. Literature data is also represented in the same Figures for comparison. As it can be seen from the figures, axial and tangential components are in good agreement with the literature.

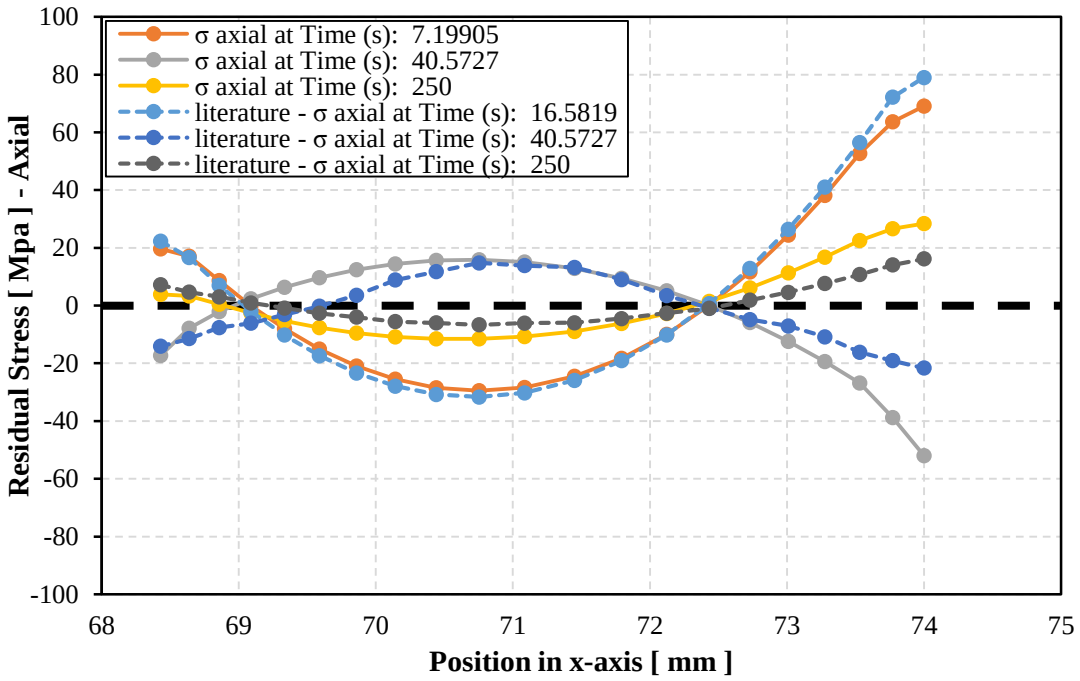

Figure 89: Variation of axial components of residual stresses along the cross-section of conical ring for a group of nodes of #5 for both simulations and literature.

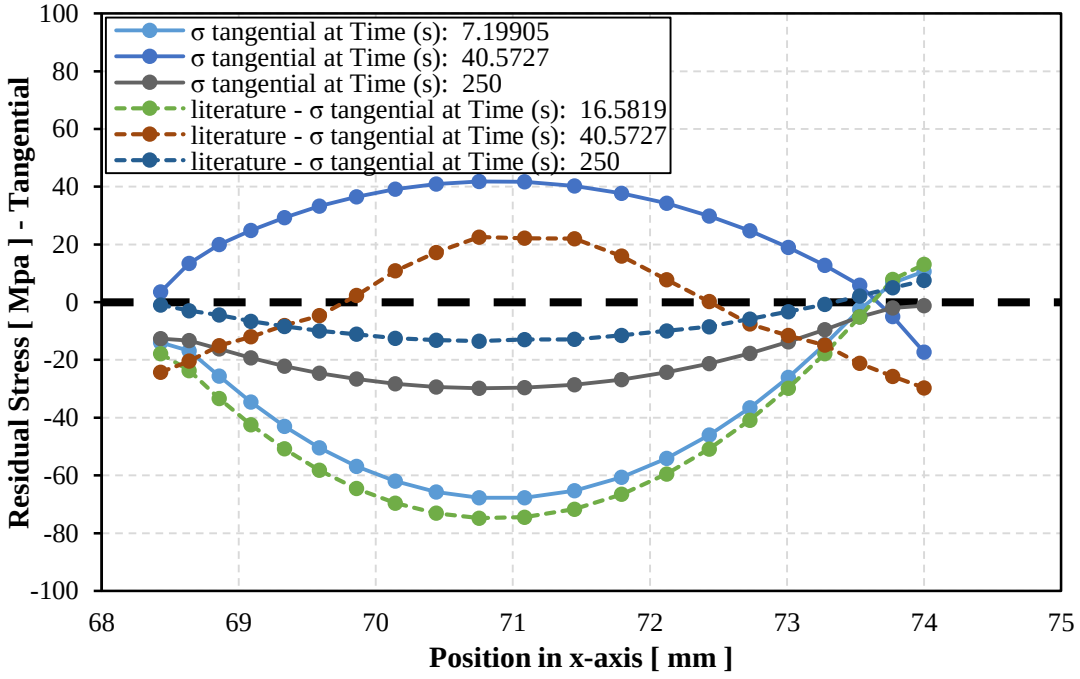

Figure 90: Variation of tangential components of residual stresses along the cross-section of conical ring for a group of nodes of #5 for both simulations and literature.

CHAPTER 6

CONCLUSION AND OUTLOOK

Through hardening is important process for manufacturing of bearing rings in order to have reliable material properties and service life of the final product. However, it can be a source of vital and irreversible product losses. Prediction of final properties of component gain a critical role for preventing these production losses. In order to achieve high quality of product without production loss and production rate, heat treatment parameters that affect the final properties of the component have to be studied. Thus, finite element method can be used as a tool for investigating the dependence of the heat treatment process parameters on final product properties.

Furthermore, through hardening is a multi-physics process that includes thermo-metallurgical, thermo-mechanical and thermal properties which can be evaluated with the help of finite element simulation software solutions nowadays. However, finite element simulation needs thermo-metallurgical, thermo-mechanical and thermo-physical material properties in advance. The material properties needed for simulations directly decide the simulation results so, in order to obtain more precise results, true and sensitive material data input to the simulation becomes crucial. In other words, material characterization is needed for success in finite element simulation of through hardening.

In this study, temperature dependent physical properties (thermal expansion coefficient), temperature dependent mechanical properties (flow curves, yield strengths, transformation strains, thermal strains) and phase transformation kinetics (TTT/CCT diagrams, critical temperatures, and effect of stress on phase

transformation) were determined using dilatometry methods for 100Cr6 bearing steel.

Thermal expansion coefficient was calculated from dilatometric experiments for spheroidite, austenite and martensite phases. The results were compared with the values present in the literature and a good agreement observed between those.

Transformation strains and thermal strains of spheroidite, austenite and martensite phases were also calculated by method described in the Chapter 3 using XRD, dilatometry and precision balance. The results were compared with the literature and they are also in good agreement.

Flow curves for meta-stable austenite, bainite and martensite phases were obtained from deformation dilatometry experiments. Experimentally obtained flow curves for each related phase were regularized with Ramberg-Osgood model. In order to determine thermo-mechanical properties of each related phase below the temperatures that were not able to be conducted experiments due to problems mentioned in the Chapter 3, a second regularization was done on K_{RO} and n_{RO} parameters of Ramberg-Osgood model. Elastic modulus of austenite phase of 100Cr6 steel is computed using the thermodynamically based thermo-physical property calculation method using commercial JMatPro® software. Results of mechanical tests were compared and validated with the available literature data and a good agreement is established between the two. Yield strengths of meta-stable austenite, bainite and martensite phases were also calculated as a function of temperature at 0.005% proof stress and the values also in good agreement with the literature.

CCT and TTT diagrams of 100Cr6 were obtained from quenching dilatometry tests which are only applicable for 30 minutes austenitization at 850°C. CCT and TTT diagrams were also calculated with JMatPro® and both experimental and computational results were compared with diagrams found in the literature. It is observed that diagrams obtained from quenching dilatometry tests are in good agreement with the literature, on the other hand, diagrams calculated using JMatPro® were not match neither experimental results nor literature.

Thermal conductivity, heat capacity, elastic modulus, Poisson's ratio, enthalpy and density values for austenite and martensite phases were also calculated using physically based computational methods and compared with the literature. They are all have good agreement with the literature. Density values for spheroidite, austenite and martensite phases were also calculated by using Buoyancy method.

At last part of the study, determined material properties were introduced as an input data to the simulation code, SYSWELD®. Simulations were initialized with a known case, which is related with through-hardening of a conical bearing ring, in order to validate the obtained dataset and compare it with the literature. Cooling curves, residual stresses, dimensions and phase proportions were the results compared for this purpose. The results have good agreement with the literature [13] so that, data set might be used for through-hardening simulations.

The minor differences between the experimental results of this study and the literature [12, 13, 65] might be due to the differences in:

- Austenitization conditions
- Starting materials (i.e. initial microstructure, composition, segregations etc.)
- Instruments (deformation dilatometers) used (DIL 805 A/D vs. Gleeble 3500)
- Experimental setup/temperature programs used
- Numerical techniques used for calculations and fittings

It is also observed that results of JMatPro® were also have minor differences between experimental results and values found in the literature [12, 13, 65]. The software is based on thermodynamic equilibrium and the investigated phases, specifically the metastable austenite, might contain larger number of point defects than the equilibrium fractions [74]. This might also be the reason for the observed minor differences.

As a future work, simulations can be performed on different through-hardening cases with different bearing ring geometries. Verification of simulations, and so dataset, can also be done by conducting quenching experiments on the furnaces.

As an improvement for the dataset, it can be suggested that heat transfer coefficient of quenchant should be determined which is also important parameter especially if oil or salt bath is used as a quenchant in the quenching case. Furthermore, computationally calculated properties can be determined experimentally in order to compare them with the here presented results (Specific Heat Capacity, Thermal Conductivity, Enthalpy, Young's Modulus and Poisson's Ratio).

Lastly, the author hopes that the dataset created in this study will be used for the simulation purposes by heat treatment and welding communities.

REFERENCES

[1] Wegst, C.W., M. Wegst, and V.S. Wegst, *Stahlschlüssel: Key to steel*. 2010: Verlag Stahlschlüssel Wegst.

[2] Bhadeshia, H.K.D.H., *Steels for bearings.* Progress in Materials Science, 2012. 57(2): p. 268-435.

[3] Volkmuth, J., et al., *Uneven residual stresses in bearing rings prior to hardening and their effect on shape changes after hardening.* Harterei-Technische Mitteilungen, 2005. 60(6): p. 317-322.

[4] Bhadeshia, H. and J.W. Christian, *Bainite in steels.* Metallurgical Transactions a-Physical Metallurgy and Materials Science, 1990. 21(4): p. 767-797.

[5] Zoch, H.W., *Distortion engineering – Interim results after one decade research within the Collaborative Research Center.* Materialwissenschaft und Werkstofftechnik, 2012. 43(1-2): p. 9-15.

[6] Epp, J. and T. Hirsch, *Characterisation of the carrier of distortion potential "residual stresses" in the collaborative research centre "distortion engineering".* Materialwissenschaft und Werkstofftechnik, 2012. 43(1-2): p. 112-119.

[7] Şimşir, C. and C.H. Gur, *Simulation of Quenching*, in *Thermal Process Modeling of Steels*, C.H. Gur and J. Pan, Editors. 2009, CRC Press: USA. p. 341-425.

[8] Şimşir, C. and C.H. Gür, *Simulation of Quenching*, in *Quenching Theory and Technology*, B. Liscic, et al., Editors. 2010, CRC Press.

[9] Simsir, C. and C.H. Gur, *A Review on Modeling and Simulation of Quenching*, in *Quenching and Cooling, Residual Stress and Distortion Control (STP 1523)*, L.C.F. Canale and M. Narazaki, Editors. 2010, ASTM International. p. 117-156.

[10] Şimşir, C., *Modeling and Simulation of Steel Heat Treatment: Prediction of Microstructure, Distortion, Residual Stresses and Cracking*, in *ASM Metals Handbook Volume 4B "Steel Heat Treating Technologies"*. To be published in October 2014, ASM International.

[11] Schwenk, M., et al. *Data acquisition for numerical modelling of induction surface hardening process specific considerations*. in *Heat Treating 2011: Proceedings of the 26th Conference*. 2011. Cincinnati: ASM International.

[12] Acht, C., et al., *Determination of the material properties for the simulation of through hardening of components made from SAE 52100. - Part 1.* Journal of Heat Treatment and Materials (HTM), 2008. 63(5): p. 234-244.

[13] Acht, C., et al., *Determination of the material properties for the simulation of through hardening of components made from SAE 52100. - Part 2.* Journal of Heat Treatment and Materials (HTM), 2008. 63(6): p. 362-371.

[14] Ahrens, U., G. Besserdich, and H. Maier, *Modelling phase transformations in steels-have complex experiments become obsolete?* Harterei-Technische Mitteilungen(Germany), 2002. 57(2): p. 99-105.

[15] Guo, Z., et al., *Material properties for process simulation.* Materials Science and Engineering: A, 2009. 499(1–2): p. 7-13.

[16] Saunders, N. and A.P. Miodownik, *CALPHAD (Calculation of Phase Diagrams) : A Comprehensive Guide*. Pergamon Materials Series, ed. R.W. Cahn. 1998. 478.

[17] Saunders, N., et al., *Using JMatPro to model materials properties and behavior.* JOM, 2003. 55(12): p. 60-65.

[18] Chang, Y.A., et al., *Phase Equilibria and Phase Diagram Modeling*, in *ASM Handbook Volume 22A : Fundamentals of Modeling for Metals Processing*, D. Furrer and S.L. Semiatin, Editors. 2009, ASM International: Ohio, USA. p. 441-454.

[19] Guo, Z., N. Saunders, and J.P. Schillé, *Modelling Phase Transformations and Material Properties Critical to the Prediction of Distortion during the Heat Treatment of Steels.* International Journal of Microstructure and Materials Properties, 2009. 4(2): p. 187-195.

[20] Da Silva, A.D., *Prediction and Control of Geometric Distortion and Residual Stresses in Hot Rolled and Heat Treated Large Rings*, in *Department of Metallurgical and Mining Engineering*. 2012, Federal University of Minas Gerais. p. 151.

[21] Horstemeyer, M.F., *Integrated Computational Materials Engineering (ICME) for Metals: Using Multiscale Modeling to Invigorate Engineering Design with Science*. 2012: Wiley. 472.

[22] Şimşir, C., *3D Finite Element Simulation of Steel Quenching in order to Determine the Microstructure and Residual Stresses*, in *Metallurgical and*

Materials Engineering. 2008, Middle East Technical University: Ankara, Turkey.

[23] Inoue, T. and K. Tanaka, *Elastic-plastic stress analysis of quenching when considering a transformation.* International Journal of Mechanical Sciences, 1975. 17(5): p. 361-367.

[24] Lindgren, L.-E., *Finite element modeling and simulation of welding. Part 2: Improved material modeling.* Journal of thermal stresses, 2001. 24(3): p. 195-231.

[25] Inoue, T. and Z.G. Wang, *Coupling between stress, temperature, and metallic structures during processes involving phase-transformations.* Materials Science and Technology, 1985. 1(10): p. 845-850.

[26] Sjostrom, S., *Interactions and constitutive models for calculating quench stresses in steel.* Materials Science and Technology, 1984. 1(10): p. 823-829.

[27] Denis, S., S. Sjostrom, and A. Simon, *Coupled temperature, stress, phase-transformation calculation model numerical illustration of the internal-stresses evolution during cooling of a eutectoid carbon-steel cylinder.* Metallurgical Transactions a-Physical Metallurgy and Materials Science, 1987. 18(7): p. 1203-1212.

[28] Denis, S., D. Farias, and A. Simon, *Mathematical-model coupling phase-transformations and temperature evolutions in steels.* Isij International, 1992. 32(3): p. 316-325.

[29] Leblond, J.B., J. Devaux, and J.C. Devaux, *Mathematical modelling of transformation plasticity in steels I: Case of ideal-plastic phases.* International Journal of Plasticity, 1989. 5(6): p. 551-572.

[30] Leblond, J.B., *Mathematical modelling of transformation plasticity in steels II: Coupling with strain hardening phenomena.* International Journal of Plasticity, 1989. 5(6): p. 573-591.

[31] Reti, T., et al., *Computer-optimized planning of 2-stage carburising.* Heat Treatment of Metals, 1992. 19(4): p. 103-106.

[32] Jahanian, S., *Thermoelastoplastic and residual stress analysis during induction hardening of steel.* Journal of Materials Engineering and Performance, 1995. 4(6): p. 737-744.

[33] Yang, Y.S. and S.J. Na, *Effect of transformation plasticity on residual stress fields in laser surface hardening treatment.* Journal of heat treating, 1991. 9(1): p. 49-56.

[34] Gur, C.H. and A.E. Tekkaya, *Finite element simulation of quench hardening.* Steel Research, 1996. 67(7): p. 298-306.

[35] Gur, C.H., A.E. Tekkaya, and W. Schuler, *Effect of boundary conditions and workpiece geometry on residual stresses and microstructure in quenching process.* Steel Research, 1996. 67(11): p. 501-506.

[36] Johnson, W.A. and R.F. Mehl, *Reaction kinetics in processes of nucleation and growth.* Trans. AIME, 1939. 135: p. 416-458.

[37] Avrami, M., *Kinetics of phase change. II. Transformation-time relations for random distribution of nuclei.* J. Chem. Phys., 1940. 8: p. 212-224.

[38] Scheil, E., *Anlaufzeit der austenitumwandlung.* Arch. Eisenhuttenwes, 1935. 8: p. 565-567.

[39] Cahn, J.W., *Transformation kinetics during continuous cooling.* Acta Metallurgica, 1956. 4(6): p. 572-575.

[40] Christian, J.W., *The Theory of Transformations in Metals and Alloys*. 1975, Oxford: Pergamon Press.

[41] Reti, T. and I. Felde, *A non-linear extension of the additivity rule.* Computational Materials Science, 1999. 15(4): p. 466-482.

[42] Koistinen, D.P. and R.E. Marburger, *A general equation prescribing the extent of the austenite-martensite transformation in pure non-carbon alloys and plain carbon steels.* Acta Materialia, 1959. 7: p. 55-69.

[43] Magee, C.L., *Transformation kinetics, micro-plasticity and ageing of martensite in Fe-31Ni*, in 1966, Carnegie Inst. of Tech.: Pittsburgh , USA. p. 309.

[44] Lusk, M.T. and Y.-K. Lee, *A Global Material Model for Simulating the Transformation Kinetics of Low Alloy Steels*, in *Proceedings of the 7th International Seminar of the International IFHT*. 1999, IFHT: Budapest, Hungary. p. 273-282.

[45] Geijselaers, H.J.M., *Numerical Simulation of Stresses due to Solid State Transformations*. University of Twente: Twente.

[46] Denis, S., et al., *Stress-Phase transformation interactions - Basic principles ,modeling and calculation of internal stresses.* Materials Science and Technology, 1984. 1(10): p. 805-814.

[47] Denis, S., et al., *Influence of stresses on the kinetics of pearlitic transformation during continuous cooling.* Acta Metallurgica, 1987. 35(7): p. 1621-1632.

[48] Aeby Gautier, E., *Transformations perlitique et martensitique sous contrainte de traction dans les aciers*. 1985.

[49] Patel, J.R. and M. Cohen, *Criterion for the action of applied stress in the martensitic transformation.* Acta Metallurgica, 1953. 1(5): p. 531-538.

[50] Videau, J.-C., G. Cailletaud, and A. Pineau, *Experimental study of the transformation-induced plasticity in a Cr-Ni-Mo-Al-Ti steel.* Le Journal de Physique IV, 1996. 6(C1): p. C1-465-C1-474.

[51] Simon, A., S. Denis, and E. Gautier, *Effet des sollicitations thermomécaniques sur les transformations de phases dans l'état solide. Aspects métallurgique et mécanique.* Le Journal de Physique IV, 1994. 4(C3): p. C3-199-C3-213.

[52] Liu, C.C., K.F. Yao, and Z. Liu, *Quantitative research on effects of stresses and strains on bainitic transformation kinetics and transformation plasticity.* Materials Science and Technology, 2000. 16(6): p. 643-647.

[53] Bhattacharyya, S., G. Kehl, and J. Brett, *Isothermal transformation of austenite to ferrite and pearlite under externally applied tensile stress*. 1955, DTIC Document.

[54] Veaux, M., et al., *Bainitic transformation under stress in medium alloyed steels.* Journal De Physique Iv, 2001. 11(PR4): p. 181-188.

[55] Greenwood, G.W. and R.H. Johnson, *The deformation of metals under small stresses during phase transformations.* Proc. Roy. Soc., 1965. 283: p. 403-422.

[56] Fischer, F.D., Q.P. Sun, and K. Tanaka, *Transformation-induced plasticity (TRIP).* Applied Mechanics Reviews, 1996. 49(6): p. 317-364.

[57] Abrassart, F., *Influence des transformations martensitiques sur les propriétés mécaniques des alliages du système Fe-Ni-Cr-C*. 1972.

[58] Dalgic, M., et al., *Transformation plasticity at different phase transformation of a through hardening bearing steel.* International Journal of Materials and Properties, 2008. 3: p. 49-64.

[59] Cverna, F., *Thermal Expansion*, in *ASM ready reference: thermal properties of metals*. 2002, ASM International.

[60] Jablonka, A., K. Harste, and K. Schwerdtfeger, *Thermomechanical properties of iron and iron-carbon alloys: density and thermal contraction.* Steel Research, 1991. 62(1): p. 24-33.

[61] ASTM, *C518-10: Test Method for Steady-State Thermal Transmission Properties by Means of the Heat Flow Meter Apparatus*. 2010, ASTM International: West Conshohocken, PA.

[62] ASTM, *E1225-13: Standard Test Method for Thermal Conductivity of Solids by Means of the Guarded-Comparative-Longitudinal Heat Flow Technique*. 2013, ASTM International: West Conshohocken, PA.

[63] Hollomon, J.H., *Transactions of the American Institute of Mining, Metallurgical and Petroleum Engineers*. Vol. 162. 1945.

[64] Besserdich, G., et al., *Development of residual stresses and distortion during hardening of SAE 4140 cylinders taking into account transformation plasticity.* Residual Stresses, 1993: p. 975-984.

[65] Wever, F., A. Rose, and J. Orlich, *Atlas zur Waermebehandlung der Staehle*. Vol. 1-4. 1954-1976, Dues.

[66] Guo, Z., et al., *Introduction of Materials Modelling into Processing Simulation - Towards True Virtual Design and Simulation.* International Journal of Metallurgical Engineering, 2013. 2(2): p. 198-202.

[67] Saunders, N., *Computer modeling of phase-diagrams.* Materials Science and Technology, 1992. 8(2): p. 112-113.

[68] Saunders, N., et al., *The calculation of TTT and CCT diagrams for general steels.* JMatPro Software Literature, 2004.

[69] Kirkaldy, J.S. and D. Venugopalan, *Phase Transformations in Ferrous Alloys*, A.R. Marder and J.I. Goldstein, Editors. 1984, The Metallurgical Society of AIME: New York. p. 125-148.

[70] Kirkaldy, J., *Diffusion-controlled phase transformations in steels. Theory and applications.* Scandinavian journal of metallurgy, 1991. 20(1): p. 50-61.

[71] Kirkaldy, J.S., K. Hashiguchi, and G.R. Purdy, *Prediction of TTT and CCT curves for low-alloy steels.* Cim Bulletin, 1982. 75(842): p. 123-123.

[72] Miodownik, A. and N. Saunders, *Modelling of materials properties in duplex stainless steels.* Materials Science and Technology, 2002. 18(8): p. 861-868.

[73] Frerichs, F., et al., *Distortion of conical formed bearing rings made of SAE 52100.* Materialwissenschaft und Werkstofftechnik, 2009. 40(5-6): p. 402-407.

[74] Simsir, C., et al., *The Bauschinger effect in the supercooled austenite of SAE 52100 steel.* Acta Materialia, 2010. 58(13): p. 4478-4491.